Next Materials 12 (2026) 102426

Contents lists available at ScienceDirect

Next Materials

journal homepage: www.sciencedirect.com/journal/next-materials

Review Article

Cold metal transfer wire arc direct energy deposition of Mg alloys: A review

K.S.N.Satish Idury [a], Mehul Mendiratta [a], Kai Chen [b], Stanislav Evlashin [c], Jung-Ting Tsai [d], A.H.V. Pavan [e], R.L. Narayan [a,*]

[a] Department of Materials Science Engineering, Indian Institute of Technology Delhi, New Delhi 110 016, India
[b] Center for Advancing Materials Performance from the Nanoscale (CAMPNano), State Key Laboratory for Mechanical Behavior of Materials, Xi'an Jiaotong University, Xi'an, Shaanxi 710049, China
[c] Center for Materials Technologies, Skolkovo Institute of Science and Technology, Moscow 121 205, Russian Federation
[d] Department of Mechanical Engineering, National Taiwan University of Science and Technology, Taipei 106 335, Taiwan
[e] Metallurgy Department, BHEL Corporate R & D Division, Vikasnagar, Hyderabad 500 042, India

ARTICLE INFO

Keywords:
Wire arc direct energy deposition
Cold metal transfer
Microstructure
Mechanical properties

ABSTRACT

In the quest for designing large scale AM of Mg alloy components in automotive and aerospace sectors, wire arc direct energy deposition (WDED) is currently emerging as a popular process due to its enhanced scalability, high production rate, inexpensive setup for fabrication and the flexibility to integrate with a spectrum of auxiliary processing techniques. However, WDED results in higher heat input into the component being built thereby causing substantial accumulation of thermal energy during layer-by-layer deposition. This heat accumulation leads to thermal gradients, which in turn leads to build up of residual stresses, poor surface finish, distortion and the formation of large columnar grains in the finished component. Among the existing pursuits for mitigating heat accumulation, cold metal transfer (CMT) based WDED is most promising. Here we first describe state of the art in CMT WDED of Mg alloys emphasizing practical aspects and physics of this process, followed by a brief description of general trends in Mg alloy solidification with regard to cooling rate. Next, recent investigations on microstructural characteristics of Mg alloys in the as deposited condition are presented. Subsequently, the role of supplementary *in situ/ex situ* processing techniques and post process heat treatments in refining microstructure for enhanced mechanical performance are discussed. Finally, potential unaddressed research directions in this topic are summarized.

1. Introduction

Mg based alloys are attractive structural materials owing to multiple reasons. First, Mg extraction from globally abundant mineral resources and its production, is a matured technological process and as a result, worldwide annual manufacture of Mg amounts to ~ one million metric tons [1]. Mg alloys find applications in a gamut of domains like metallurgical reduction, aerospace [2–3], automotive [4–5], environment [6], biomedical [7–9] and energy storage [6,10]. Second, as the lightest structural metal, magnesium possesses a density approximately 65% that of Al and 38% that of Ti, along with excellent specific strength [11]. Mg and its alloys have a great potential to address the global warming issues in aviation and automotive sectors as they enable minimization of specific fuel consumption. For aviation and automotive industries conventional processing techniques for fabricating Mg alloy-based products in cast, wrought and sheet configurations has already reached the highest level of commercialization [1]. However, these conventional processing techniques are yet to overcome technological challenges in terms of imparting superior combination of strength-ductility along with ease of processability for structural applications [12–15]. For instance, the volume fraction of precipitated Mg-Al intermetallic phases in cast Mg-Al based alloys is insignificant to impart dislocation strengthening. Although advances in alloy design has enhanced the castability and tensile strength of Mg alloys, cast components are still inferior to their wrought counterparts in terms of mechanical performance [13–15]. Likewise, wrought Mg alloys are difficult to process at room temperature as they possess limited slip systems, profuse basal texture induced mechanical anisotropy, larger critically resolved shear stress of non-basal slip systems and propensity for twinning [13]. As Mg alloys have limited ductility and high strength at room temperature, their formability can be increased only with enhancement in processing temperature. Therefore, due to the practical processing challenges of Mg based

* Corresponding author.
E-mail addresses: rlnarayan@iitd.ac.in, rlnarayan@mse.iitd.ac.in, ragubuddy@gmail.com (R.L. Narayan).

https://doi.org/10.1016/j.nxmate.2026.102426
Received 26 September 2025; Received in revised form 23 May 2026; Accepted 2 June 2026
Available online 8 June 2026
2949-8228/© 2026 The Author(s). Published by Elsevier Ltd. This is an open access article under the CC BY license (http://creativecommons.org/licenses/by/4.0/).

wrought alloys at room temperature, a majority (~90%) of the commercial Mg alloy components are, as on date, fabricated via die casting, although the obtained final product has suboptimal mechanical properties [16].

The emergence of Additive Manufacturing (AM) offers an alternate technological paradigm towards synergizing the strength-ductility performance of Mg alloys vis-à-vis their conventionally manufactured counterparts [17]. In metal AM, a minor volume of the material is subjected to rapid melting by a thermal energy source in the region of interest in a repetitive and iterative manner based on the inputs from a digital model. As a result, on solidification, the fabricated components inherit meso-structural features that are characteristic of the scan strategy employed. Moreover, since the built component undergoes non-equilibrium solidification and experiences thermal gradients across layers owing to thermal cycling, it microstructure consists of fine grains along with some non-equilibrium phases. Moreover, the comparatively faster cooling rate enhances the solubility of secondary alloying elements in the matrix [18–31]. Consequently, AM results in the formation of hierarchical microstructures at multiple length scales, which can be tailored to yield optimal strength-ductility synergy for structural applications [23]. Conventional manufacturing routes, such as casting, produce structures with defects such as slag inclusion, coarse grains and shrinkage, which ultimately affect the mechanical properties [32–35]. Die-casting and hot extrusion for magnesium alloys [36–37] create structures with inadequate mechanical strength and permeability. Presently, AM of Mg alloys is a topic of significant research interest and comprehensive reviews in this direction have already been documented [38–47]. Specifically, AM of Mg alloys for biomedical applications [48–52] is being actively pursued through powder bed fusion (PBF) as this technology enables fabrication of implant geometries with great precision and surface finish vis-à-vis other existing AM techniques [48, 53–55]. However, PBF of Mg alloys present considerable challenge as compared to structural alloys like steel, Al, Ti and Ni based alloys owing to the presence of low vapor pressure alloying elements (Mg, Al, Zn, Mn) [56,57] in it, which evaporate during fabrication and lead to the formation of metallurgical defects and pores [58–62]. These defects are detrimental to the structural integrity of the component. Hence commercialization efforts of PBF Mg alloys for automotive and aerospace applications is hindered as the latter demands production of large complex shaped components that are mechanically reliable.

In the quest for a robust AM technique for manufacturing large-scale Mg components, alternate AM technologies like laser based direct energy deposition (LDED) [41], friction stir processing [63–69] and wire arc direct energy deposition (WDED) [44, 70–71] are being explored. Among these methodologies, WDED or wire arc additive manufacturing (WAAM) is currently emerging as a popular process for fabricating Mg based alloys due to its superior scalability, high production rate, inexpensive setup for fabrication (WDED is an extension of conventional arc welding process) and the flexibility to integrate with a spectrum of auxiliary processing techniques [72–75]. Since this method utilizes thin filler wires instead of metal powders, it also obviates vaporization issues of low vapor pressure elements in Mg alloys. In this regard, two recent reviews on WDED Mg alloys [76,77] summarize the scope and breadth of the state of the art in research investigations.

Despite the emerging popularity of WDED, certain drawbacks in this process need to be overcome towards its large-scale commercialization. WDED results in higher heat input into the component being built thereby causing substantial accumulation of thermal energy during layer-by-layer deposition. This progressive heat accumulation leads to creation of residual stresses, poor surface finish, dimensional distortion and generation of large columnar grains in the microstructure [76–80]. Therefore, WDED thermal management strategies for minimizing higher heat input towards mitigating these process-induced defects and tailoring the solidification microstructure is presently an active research topic. Among such existing innovative pursuits for mitigating heat accumulation, cold metal transfer (CMT) based WDED [81] is attracting attention in the research community, as evident from numerous recent publications available in open literature. Currently, there are no reviews that depict the state of the art in CMT based WDED Mg alloys in a focussed manner and this forms the primary motivation for this paper. This review paper is further organized as follows. Section 2 outlines practical and physical aspects of CMT WDED. In Sections 3 and 4, general trends in solidification behavior of Mg alloys and recent advances in microstructural evolution of CMT WDED magnesium alloys, respectively, is discussed. Section 5 summarizes the microstructural aspects of Mg alloys when CMT WDED is integrated with supplementary processing techniques. In Section 6, the role of post process treatments in fine tuning mechanical performance is elaborated. Finally in Section 7, the deformation response of CMT WDED Mg alloys is discussed under the purview of structure-property correlations.

2. CMT WDED practical and physical aspects

2.1. Necessity and significance of CMT WDED

Fig. 1 schematically illustrates the importance of input thermal energy in an AM process since it governs the temperature distribution in the built component, size of melt pool, melt pool solidification kinetics, microstructural evolution, defect formation, residual stress generation and subsequently the mechanical properties of the fabricated component. A reliable structure-property correlation in AM components can be established if the link between input process parameters that create a heat source for alloy melting, and characteristic metallurgical variables is established [82]. In WDED, thermal energy generated from an electric arc is utilized for a layer-wise fabrication on a substrate. Accordingly, WDED is broadly categorized as either non-consumable electrode based or a consumable electrode-based process. In the former, an electric arc generated in a shielded atmosphere between a tungsten electrode and a separate filler wire (gas tungsten arc (GTA) and plasma arc (PA) variants) functions as a heat source. Alternately, in the case of gas metal arc (GMA) based WDED, the arc is produced between the coaxial expendable filler wire and the substrate. The electric arc serves as a medium for the diffusion of electrons and ions, whose paths depend upon the polarity of the electrode and the substrate [20]. While the electrons move from cathode to anode, ions move in the opposite direction. During their movement in the arc column, the kinetic collisions of the electrons and ions is converted into heat energy.

Electrode polarity, voltage and current supplied to sustain the arc, filler wire diameter, chemistry of shielding inert gas are the important variables that govern the electric arc characteristics in WDED. GMA based WDED is superior in terms of absorbing thermal energy generated in the arc, compared to GTA and PA variants since there is a mass transfer from the molten filler wire to the substrate melt pool [20]. The heat absorption by the filler wire is a function of the magnitude of temperature generated in the arc, chemistry and surface roughness of the filler wire and the mode of molten metal transfer from the filler wire to substrate [20]. Depending upon the relative degree of time duration of metal droplet growth (t_g) at the tip of filler wire and contact time between the filler wire and melt pool (t_c) four modes of metal transfer are recognized as described below:

Mode 1: $t_c >> t_g$, where the filler wire is in virtual constant contact with melt pool

Mode 2: $t_c \sim t_g$, where the droplet growth time is identical to droplet contact time

Mode 3: $t_c << t_g$, where the droplet size becomes bigger with time

Mode 4: t_c tends to *0*, where there is no contact with melt pool and the energy for melting is obtained from arc plasma

At the tip of the filler wire, an inherent competition exists between surface tension, drag force of arc plasma and the gravity. While surface tension aids in formation of molten droplets and holds them onto the wire tip, gravity and drag forces are responsible for the detachment of droplets from the filler wire [20]. The droplets formed at the tip of the

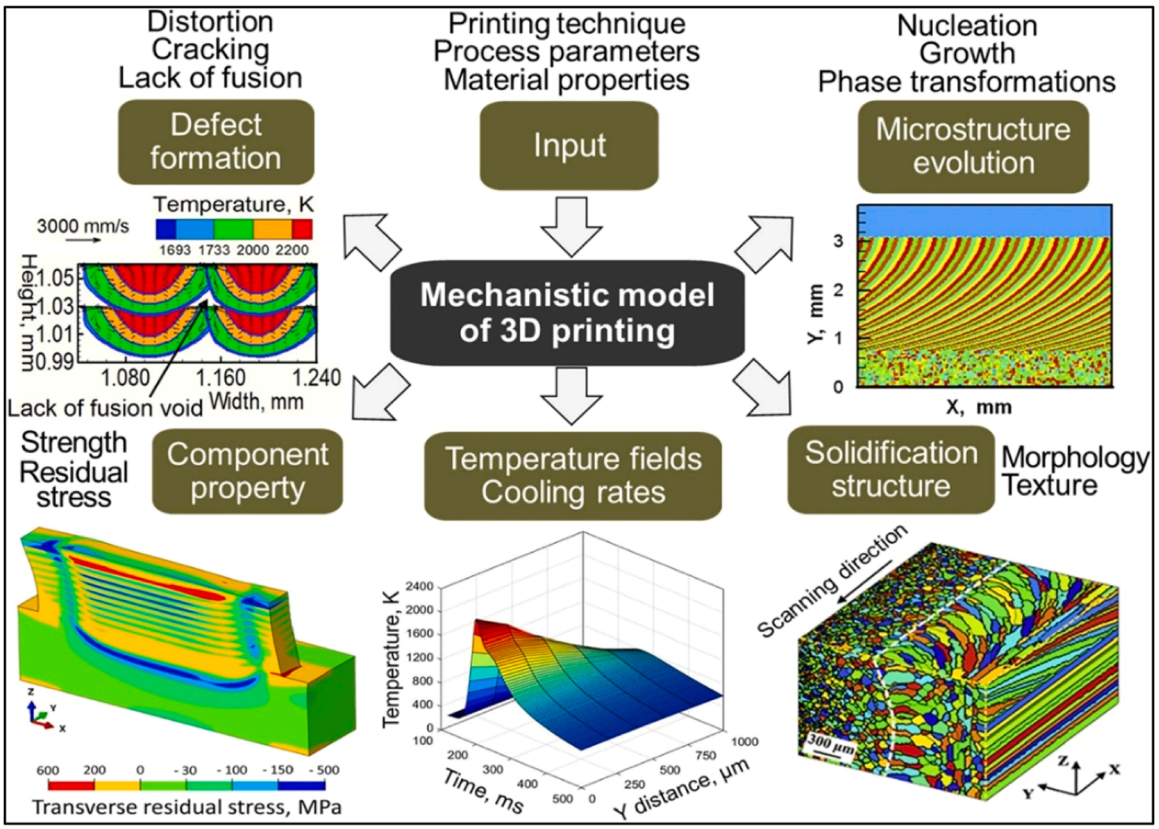


Fig. 1. Critical role of heat and mass transfer in analysis of AM process [82]. (*Reproduced with permission from Elsevier*).

filler wire due to heat input continue to grow until drag force and gravity are sufficient to rip the droplet and transfer it into the underlying melt pool. The kinetics of molten metal transfer from the filler wire tip to the substrate melt pool is driven by the magnitude of electric current supplied to sustain the arc. At significantly higher input currents, the filler wire melts faster and smaller sized droplets are sprayed into the underlying melt pool. Likewise, at moderate currents, the molten drops of filler wire take the spherical shape until they are detached under the influence of gravity. Therefore, higher and moderate input currents generally lead to pronounced spatter and surface roughness despite increased build rate [20]. Alternately, when a small input current is applied to create arc, the transfer of molten metal from the filler wire happens through the contact of the elongated droplet with underlying surface by creating a short circuit. Due to smaller input currents involved here, the size of the melt pool will be smaller, deposition will be free of spatter and better surface finish can be achieved. This process of depositing the molten metal from the filler wire tip via short circuiting the substrate at smaller currents forms the basis of cold metal transfer (CMT) WDED process.

2.2. *Practical aspects of CMT WDED process*

In WDED, the transient temperature distribution in the melt pool is complex compared to other metal AM processes. Here, in addition to the surface tension differential in the fusion zone, mass transfer of molten droplets from the filler wire and electromagnetic force of the arc dominate the convective heat transfer [20]. To mitigate momentum transfer from filler wire and electromagnetic force effects on melt pool convection, three successive processes need to be integrated, which are as follows.

a) a precisely controlled wire feed mechanism that switches off input current during the time interval of filler wire's contact with substrate
b) retraction of the wire, post contact to ensure droplet metal transfer due to the wire's oscillation force
c) reinitiation of electric arc with small input current to recreate metal droplet

The above-mentioned steps, if sustained in a cyclical and coordinated fashion, ensures that the transfer of metal droplet from filler wire happens only due to the mechanical oscillation force while mitigating the role of the electromagnetic force. Hence, for a given quantum of droplet transfer, the input current is significantly lessened so as to reduce spatter and also minimize heat accumulation in the fusion zone. CMT an evolutionary version of GMAW developed by Fronius Technology Austria, incorporates the above mentioned electrical cyclic process (see Fig. 2). CMT WDED is capable of fabricating wide range of components with extremely low heat input and dilution rates. It is a relatively a spatter free process in comparison to conventional GMAW, has high arc stability and can be operated in various modes. CMT process has a servomotor to initiate forward and retreating motion of the wire electrode to smooth molten pool detachment and enable better melt pool flow dynamics [81]. CMT has inbuilt wide range of optimal process parameters so that metal depositions can be carried out either in metal inter gas mode using argon or in metal active gas mode using ($Ar+CO_2$, $Ar+ N_2$, $Ar + CO_2$) mixtures.

Fig. 2**a** illustrates the waveforms of voltage and current during CMT deposition process on AZ31 Mg alloy in direct current (DC) mode. Here, a typical CMT cycle comprises a prolonged time interval during which the input current is increased to the peak value to melt the filler wire tip for creating a metal droplet, which is referred to as the 'arcing phase'. Furthermore, as the filler wire is fed forward towards the underlying melt pool, the input peak current is simultaneously lessened to a fraction of peak current, which is known as the 'base phase' [83] By reducing the current, the transfer of liquid droplet into the melt pool under the influence of gravity is prevented. When the filler wire is about to initiate

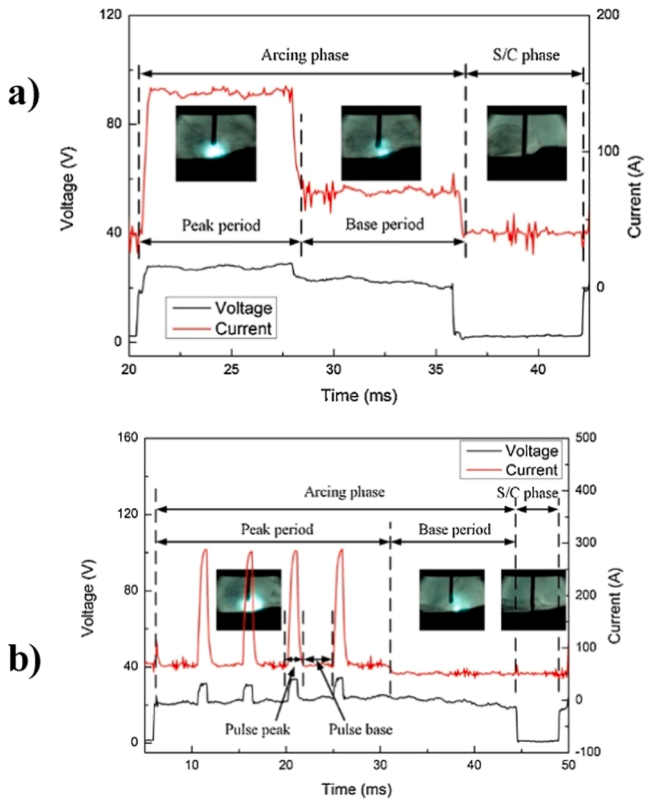


Fig. 2. Waveforms of current and voltage during CMT process of AZ31 Mg alloy (**a**)direct current CMT (**b**) pulsed CMT process [83]. (*Reproduced with permission from Elsevier*).

contact with melt pool during its downward motion, the input current is further reduced while creating a short circuit (S/C) path. Here the arc voltage is set to zero volts. During the S/C phase, the filler wire is withdrawn from the melt pool to complete the molten drop transfer. Fig. 2**b** illustrates the pulsed CMT mode comprising of multi peak input current pulses during arcing phase while base phase and S/C phase are identical to DC CMT. With the incorporation of multiple cycle of peak current in the arcing phase, the heat input into fusion zone can be enhanced that will aid in melt pool convection and also increased deposition rate [83]. Due to differences in the heat input imparted among different CMT modes, the wire feed speed varies. Higher wire feed speeds are practically feasible in cases of where lower heat input is envisaged and vice versa.

CMT WDED is a versatile process because the advancements in GMAW can be extended directly into the experimental setup depending upon processing requirements. The welding power sources supplemented through the innovations in modern electronics respond swiftly to requirements of varied heat input for fabrication through manipulation of voltage and current waveforms [84]. Current-voltage waveforms of Pulsed CMT process depicted in Fig. 2**b** can be further tailored by combining a sequence of complex pulses with different S/Cing time durations so that metal deposition rates and heat input are matched as per alloy chemistry. If the pulse frequency is increased, it will lead to higher heat input whereas an increase in S/C duration enhances metal deposition rate. The use of mixed current/voltage waveforms synergize the advantages of different waveforms in a single duty cycle. Fig. 3 illustrates different variants of current and voltage waveforms generated in CMT. Figs. 3**a** and 3**b** depict the wave forms with electrode having positive polarity whereas Figs. 3**c** and 3**d** indicate variable polarity of the electrode. Fig. 3**a** illustrates CMT mode with multiple broad peaks indicating longer time interval of arcing phase whereas in Fig. 3**b**, CMT pulse mode is shown, where high frequency pulses appear in the arcing phase. In Fig. 3**c**, which displays the current waveform in the CMT advanced mode, increased S/C frequency with electrode negative polarity is the prominent feature. In CMT pulse advanced mode (see Fig. 3**d**), multiple peaks appear in both arcing phase and short-circuiting phase with former in electrode positive and latter in electrode negative polarity [85]. Hence, by combining various metal transfer modes with sophisticated power electronics-controlled power sources, heat input to the component being fabricated can be controlled effectively by manipulating various forces acting on the metal droplet [85].

Fig. 4**a** shows the schematic illustration of a CMT set-up comprising a robotic arm controlled CMT torch, which incorporates the wire feed mechanism, shielding gas source and a power source. Fig. 4**b** illustrates the enlarged view of layer wise deposition of CMT WDED build component in vertical direction along with reciprocating motion of consumable wire for generating the arc in the presence of shielding gas. Fig. 4**c** depicts the process parameters in a general WDED process which include characteristics of power source for imparting energy to melt the wire, shielding gas chemistry and its flow rate, nature of substrate and characteristics of feed wire [86]. In Fig. 4**c** the substrate composition influences the wettability and dilution effect of the weld bead on the surface. The substrate volume and stiffness provides resistance to distortion. Mechanical tensioning of the substrate through fixtures could further reduce distortion; however, it may increase the residual stress formation [87].Apart from the primary parameters for tuning the quality of built component, various supplementary processes incorporated into the general WDED set-up, provide additional leverage for enhancing build quality. These processes are performed either *in situ* or post fabrication such as, imparting *in situ* mechanical oscillations to filler wire and component being built, machining and mechanical deformation in post fabricated condition, thermal treatments performed either *in situ* or post WDED [79]. Nevertheless, it is reckoned that *in situ* supplementary processes are effective in addressing heat accumulation issues compared to their *ex situ* counterparts [79].

2.3. *Practical aspects of supplementary processes for CMT WDED*

Fig. 5 illustrates the versatility of WDED in integrating other ancillary process like ultrasonic processing, manipulation of electric/magnetic fields, laser processing, *in situ* deformation techniques, and collaboration of multi robots for hybrid fabrication.

Ultrasonic treatments to the workpiece promote effective stirring of the fusion zone, which not only leads to the disintegration of dendrites in the mushy zone but also facilitates the separation of incompletely melted grains and their uniform mixing within the melt pool [88]. In magnesium alloy WAAM, ultrasonic assistance has been reported to enhance cavitation-induced melt flow, reduce the temperature gradient, promote constitutional supercooling, suppress solute segregation, and refine the microstructure from coarse grains to fine equiaxed grains through dendrite fragmentation and secondary nucleation mechanisms [89–90]. Moreover, ultrasonic vibration also improves the uniform distribution of in-situ formed oxide particles and reduces defect formation, thereby contributing to simultaneous enhancement of strength and ductility in AZ31 magnesium alloy deposits [90]. As mentioned previously, judicious incorporation of high-frequency pulses coupled with short-circuit transfer can also be utilized for tailoring melt-pool oscillations. Likewise, the electromagnetic field in the filler wire can be manipulated by incorporating multiple magnetic oscillators that produce magnetic fields along the axis parallel to the welding electrode [91]. These electromagnetic oscillators generate Lorentz force, which induces arc rotation and vigorous melt-pool stirring, thereby improving wettability, reducing porosity, suppressing interfacial reaction layer growth, and altering the orientation of long columnar grains through enhanced fluid flow and redistribution of thermal gradients. In CMT welding of Al/Mg alloys, magnetic oscillation has also been reported to expand the arc heating area, refine weld microstructure, and reduce brittle intermetallic compound formation due to electromagnetic

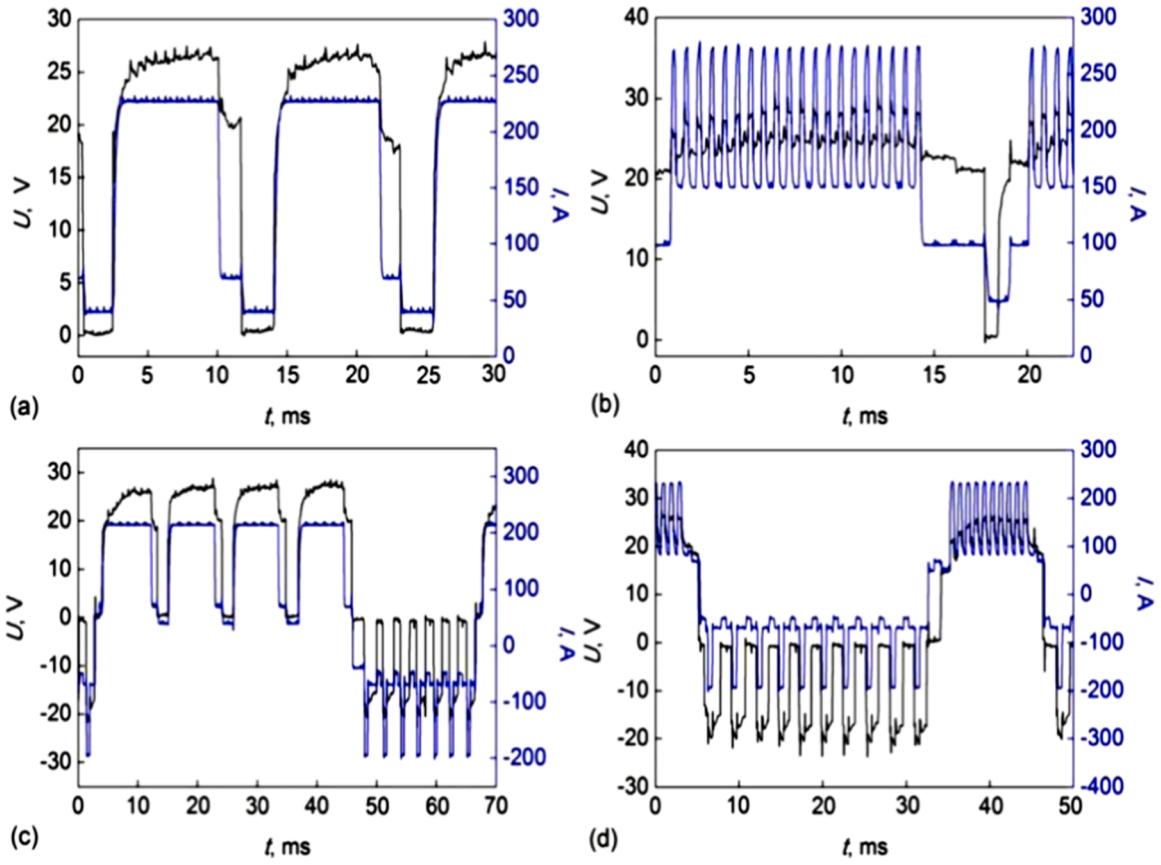


Fig. 3. Different mixed waveform configurations (**a**) CMT mode (**b**) Pulsed CMT mode (**c**) CMT advanced mode (**d**) CMT-Pulse advanced mode [85]. (*Reproduced with permission from Springer Nature*).

stirring effects within the molten pool [92]. The magnetic oscillation CMT welding increased the microhardness value at the interface and the shear strength value by 30% compared to without magnetic oscillation. Despite the fact that CMT results in less heat accumulation in the build component, WDED also has additional provision for incorporation of *in situ* cooling to augment microstructural refinement [79,86]. In addition to the above-mentioned techniques, *in situ* deformation through processes like rolling, hammer peening, friction stir processing, ultrasonic/laser shock peening aid in porosity mitigation, induction of surface compressive residual stress and texture modification [72,73]. One of the important features that makes WDED truly unique among existing AM techniques is utilization of filler wires as material source for fabrication, which is not only cost effective but also renders superior deposition rate. The filler wires of required diameter are fabricated through wire drawing and extrusion processes whose technology has matured to the commercial level. Another interesting aspect of WDED filler wires is that they can be fabricated in the form of multi material configurations, stranded configuration, composite wires and cored wires (which embed metal powders in a hollow tube) [88]. As a result of such flexibility, WDED is ideally suited for large scale industrial fabrication.

2.4. Physics of CMT WDED process

2.4.1. Melt pool energy conservation and forces responsible for its dynamics

CMT WDED is a multiscale multi-physics process as the phenomenon of metal deposition involves, the mechanism of arc generation, melting of the filler wire and transfer of molten droplets to the fusion zone after short circuiting, thermal field evolution due to heat and mass transfer into the fusion zone, evolution of microstructure and residual stresses. Fig. 6 depicts the interconnection of various phenomenon to reliably estimate the temperature field evolution in the build component and highlights the additional complexities introduced by virtue of coupling laser, magnetic and ultrasonic fields to WDED process [93]. CMT WDED involves vast spectrum of process parameters (Fig. 4**c**) whose mutual interaction during the practical deposition conditions influences the melt pool dynamics in a transient manner [93]. Given such transient nature of this entire process, numerical simulations are ideal tools to comprehend the intrinsic coupling between diverse physical fields. The goal of these simulations is to portray the temporal evolution of the melt pool geometry and depict the transient temperature distribution. Estimating the transient temperature distribution is the key to understand microstructure evolution.

Heat transfer from the arc is inhomogeneous in the direction of deposition due to its asymmetric shape. Besides arc shape, the inclination of the torch to the build surface also affects the distribution of thermal energy. Also, melt pool evolution during CMT WDED is governed by the conservation of mass, momentum and energy. The conservation of mass in this process is influenced by the rate at which the molten droplets are deposited into the melt pool. In turn, the rate of molten metal deposition is a function of filler wire's radius, energy density at the tip and its feeding rate. The morphology of the droplet and its rate of deposition are important attributes for melt pool convection since irregular droplets contribute to pronounced spatter [93]. Likewise, the conservation of momentum in the melt pool is affected by surface tension, gravity force acting the descending droplet, Lorenz force, drag and shear forces generated by the virtue of arc plasma [20]. In cases where external fields like ultrasonic, magnetic and laser energy incorporated into WDED, conservation of momentum is affected. Finally, the conservation of input thermal energy is accounted for by conduction into the build component, and convection and radiation into the ambient atmosphere. A brief account of the forces responsible for these physical mechanisms is as follows.

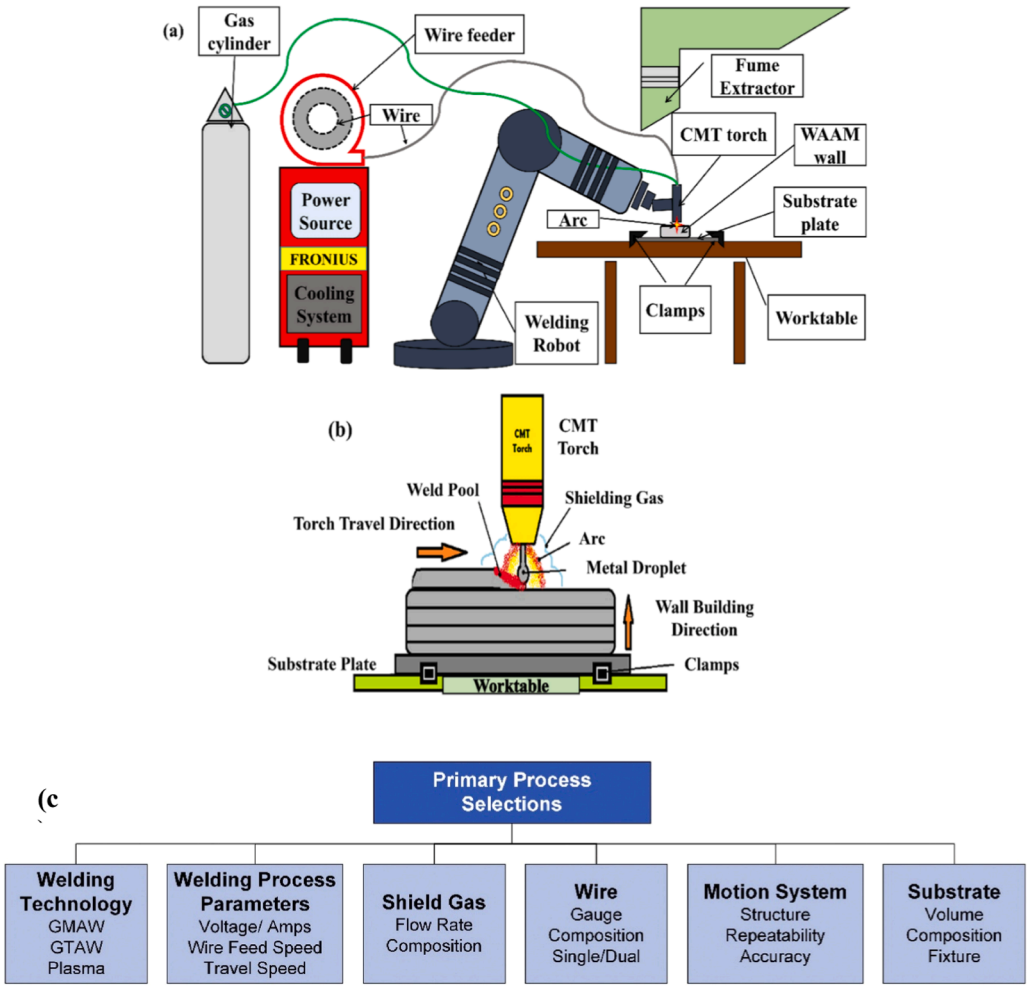


Fig. 4. Schematic illustration of CMT WDED and its process parameters (**a**) CMT WDED experimental set up (**b**) enlarged view of CMT torch and work piece [86]. (a) and (b) (*Reproduced with permission from Springer Nature*) (**c**) general process parameters in a WDED process [79] (*Reproduced with permission from Elsevier*).

Surface tension gradient exists at the melt pool surface due to inhomogeneity of the heat distribution by the arc, which drives melt pool convection, also referred to as Marangoni convection. Similarly, the inhomogeneous temperature distribution also disrupts the equilibrium hydrostatic pressure at the melt pool surface leading to its uneven rise, which manifests as the buoyancy force on the melt pool. Lorenz force is generated due to mutual coupling of electric and magnetic fields in three mutually perpendicular directions which exhibit a Gaussian distribution. The variation in the quantum of the input currents and their spatial distribution also induces pressure on the melt pool, which is referred to as arc pressure. Additionally, the frictional effects in the mushy zone and the Darcy forces due to the mechanical oscillations of filler wire lead to melt pool fluctuations [94]. Since the electric arc is in the high temperature plasma state, its downward motion during wire feed exerts a shear force on the melt pool, whose magnitude is determined by the arc's viscosity and its velocity gradient.

2.4.2. *Impact of arc characteristics on melt pool fluctuations*

Once the arc is initiated, it exerts mechanical pressure on the nonuniform melt pool surface in a heterogeneous manner. Since the arc shape is asymmetric and its energy distribution is Gaussian in space, the maximum mechanical pressure is induced underneath the arc's central axis, which causes a downward flow of liquid metal in the center of the fusion region and creates a depression [93]. Owing to maximum arc pressure and temperature at the central axis, the metal in the melt-pool flows outward towards the melt-pool boundaries. Since the maximum current intensity is focused at the center of the arc, there is a temperature gradient in the melt-pool, where ethe temperature is highest at its center and lowest at its boundaries. This spatial temperature gradient promotes an annular flow of liquid metal with a higher velocity component at center of the melt pool and minimum at its boundaries [93]. As mentioned in Section 2.2, the morphology of the arc can be varied with the incorporation of high frequency current pulses, to alter liquid metal flow in the fusion zone.

2.4.3. *Role of CMT in melt pool dynamics*

CMT alters the droplet morphology by virtue of its feed wire oscillations at the time of molten metal deposition. Owing to input current termination in the vicinity of fusion zone coupled with the relatively higher filler wire velocity in this process, the ability of molten droplets to grow into stable large sized spheres is restricted. As S/Cing happens prior to molten metal transfer, the formation of irregular shape droplets or larger spherical droplets that impart turbulence to the fusion zone is prevented [93,94]. Moreover, owing to current termination prior to metal transfer, CMT does not induce steep thermal gradients unlike the conventional mode of metal transfer. Due to decrease in melt pool turbulence and its input thermal energy, the formation of fluid vortices that create churning effect in melt pool is restricted thereby resulting in a shallower fusion zone and enhanced solidification rates [93,94]. However, in the context of pulsed input current, the exact role of pulsing in melt pool dynamics during CMT mode of metal deposition is yet to be thoroughly understood. Here, the effect of either increase in the duty

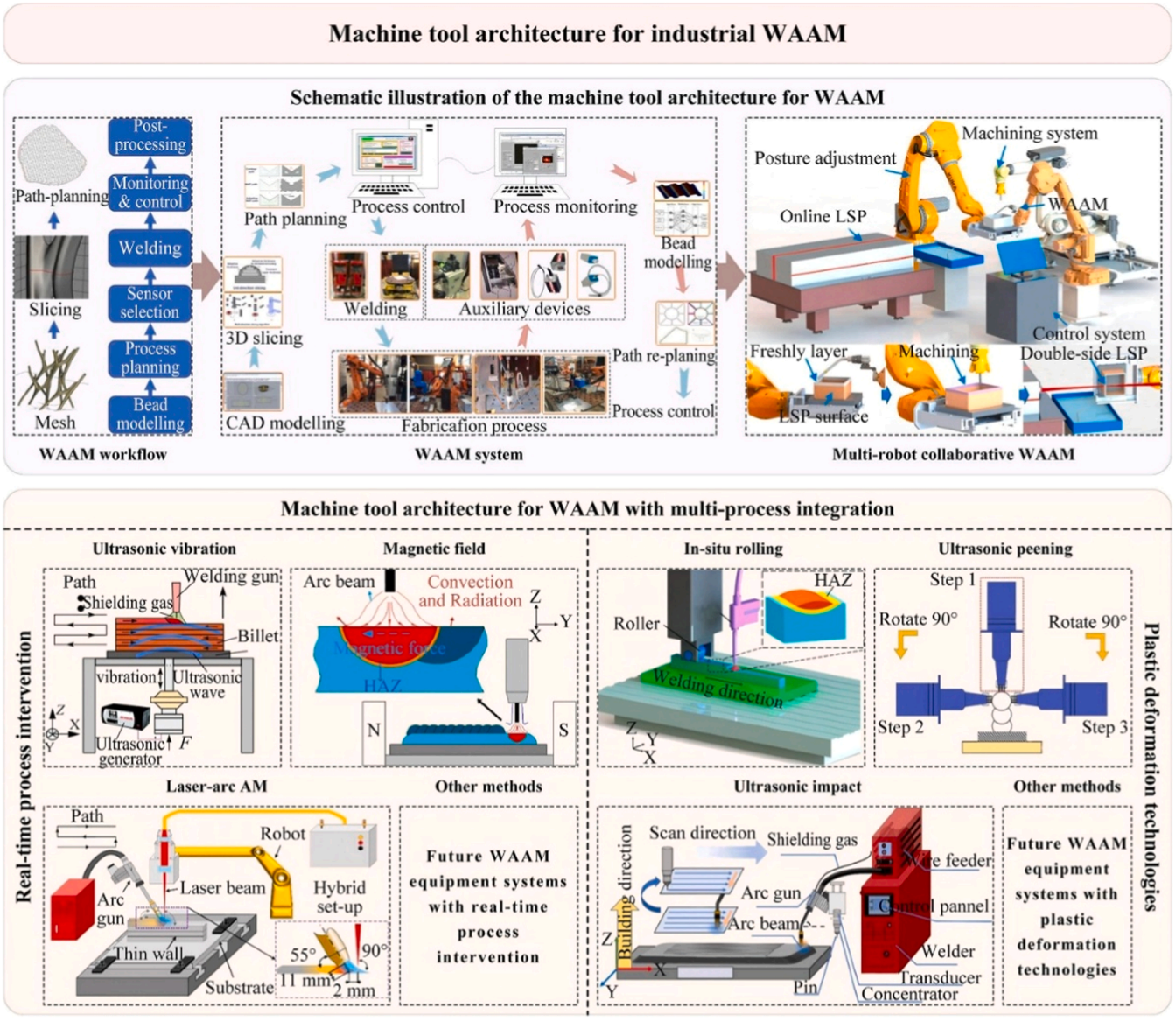


Fig. 5. Supplementary process in WDED aimed at enhancing fabrication quality [88]. (*Reproduced with permission from Elsevier*).

cycle and subsequent increment in heat input due to low frequency pulses or increase in momentum transfer due to high frequency pulses is succeeded by the extinguishment of arc before deposition.

Despite the effectiveness of CMT in minimizing the heat input and melt pool oscillations, Mg alloys pose significant challenge in fabrication as they are sensitive to both quantum of thermal energy imparted and alloy chemistry. Mg alloys are amenable for deposition only in a narrow window of process parameters beyond which they exhibit pronounced spatter [95]. The formation of spatter has been verified for Mg alloys during both arcing phase and short-circuiting phase, with the former being the dominant factor that contributes to this instability. Since a typical CMT cycle comprises of base current, peak current, peak current duration and short circuit current parameters, any increment in any of these beyond a threshold will lead to spatter. Specifically, simultaneous increase in both peak current and its duration will lead to pronounced increment in heat input beyond the melting point of Mg and will result in its evaporation. The produced Mg vapor exerts a potent recoil pressure on the descending molten droplet and repels it away from the central axis of the arc to cause spatter. Although an increase in the base and short circuit current will result in random spatter formation, it is not as severe as that caused by increase in peak current. [95].

Fig. 7 below illustrates the numerical simulation of droplet transfer during a typical CMT cycle for Mg-Gd-Y-Zr alloy. In Fig. 7**ai**, where lower peak current and peak duration conditions are simulated, the droplet remains spherical with a constant diameter throughout the cycle and undergoes stable deposition with its temperature well below melting point of Mg [95]. Fig. 7aii, which contains a simulation of higher peak current and longer exposure duration, depicts not only increase in droplet size and temperature close to melting point, but also forms an additional droplet which too begins to expand before depositing into the melt pool. Fig. 7aiii shows the velocity vectors for both conditions. While low heat input results in unform velocity along the arc axis, the drop is repulsed from the arc axis in the other condition [95].

In addition to electrical power parameters, filler wire feed rate will also affect the droplet dynamics and arc stability. Hu *et al.* [83] reported stable arc characteristics at lower wire feed rate during pulse CMT mode deposition of AZ31 Mg alloy. However, for a given frequency of pulses, if the feed rate is increased, it leads to droplet instability due to generation of recoil force (see Fig. 8). Conversely, the DC CMT mode which generates less heat input compared to pulsed CMT, facilitates greater wire feed rates, which ensures arc stability and stable droplet deposition [83].

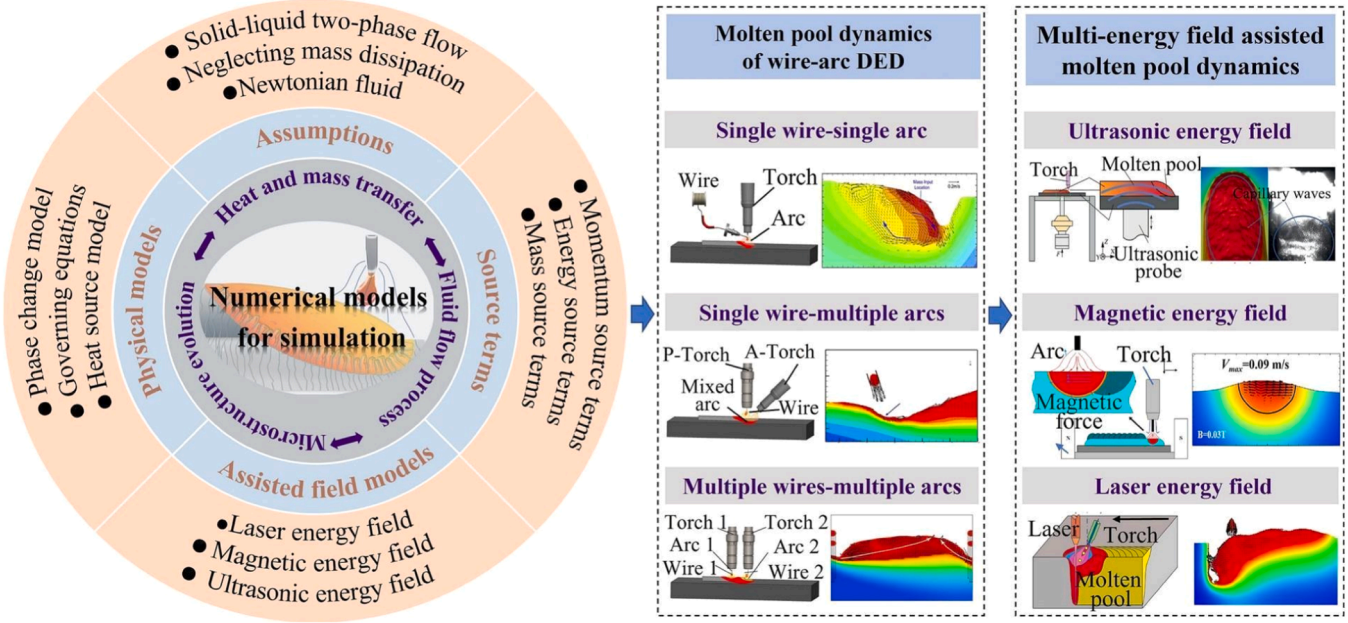


Fig. 6. Paradigm for numerical simulation of WDED through multiscale models [93]. (*Reproduced with permission from Elsevier*).

3. Solidification characteristics of Mg alloys: implications of cooling rate

3.1. Melt pool and dendrite evolution

There are serious solidification related challenges during CMT WDED of Mg alloys owing to their metallurgical characteristics. The mode of heat transfer in the built component is transient during fabrication thereby resulting in complex microstructure evolution. When the first layer is being deposited, the rate of heat extraction is governed by heat conduction into the substrate. However, with increase in the number of deposited layers, considering that a thin wall is fabricated, convection heat transfer to the surroundings can be enhanced in case of providing forced air/water circulation in vicinity. Here, the increase in surface area of thin wall in vertical direction promotes higher heat dissipation. But in case of absence of such forced air/water circulation in practical setup, heat accumulation in the build wall dominates heat dissipation since heat flux has to be dissipated only in downward direction. Alternately, with further increase in deposited layers, where successive beads are also adjacently deposited to form a thick wall, heat conduction can be promoted due to increase in additional cross sectional area. Therefore, in CMT WDED, three factors that are responsible for the formation of long columnar grains along the build direction, at the region adjacent to substrate are as follows. One, energy density of the arc source and the corresponding low solidification rate, two, substrate promoting the heat sink effect and three, unhindered grain growth in the absence of mechanisms that can promote competitive nucleation [79]. Since convection is the dominant mode of heat transfer in the melt pool, its sluggish heat dissipation rate [96] leads to heat accumulation during layer wise deposition. This uneven heat dissipation further complicates the microstructural evolution of Mg alloys, which by virtue of their HCP crystal structure exhibits alloy chemistry sensitive multiple dendritic growth modes even in conventional processing conditions along favored crystallographic orientations (see Fig. 9) [97].

In the context of CMT WDED, dendrites will start to evolve in a columnar fashion because the thermal gradient is perpendicular to the plane of welding torch motion. Although alloy chemistry affects the growth and characteristics of dendrites, Mg alloys exhibit typical generic features like growth of primary, secondary and tertiary arms depending on the inherent competition between them during solidification [98]. Scanning speed of the WDED heat source exerts significant influence on the dendrite growth velocity and segregation of solutes. With increase in heat source scanning speed, both dendrite growth velocity and solute segregation are reduced. This is attributable to increase in the speed of the solidification front (R) and reduction in temperature gradient (G), respectively [99]. A high G/R ratio promotes stable directional solidification and favors the formation of columnar dendrites aligned with the heat flow direction. In contrast, a reduced value increases constitutional supercooling ahead of the solidification interface, thereby enhancing heterogeneous nucleation and promoting equiaxed grain formation. Furthermore, the cooling rate ($G\times R$) significantly influences dendrite arm spacing and grain refinement, where higher cooling rates generally produce finer microstructures. Thus, enhancement in heat source scanning speed also leads to an increase in the primary dendritic arm spacing and their width. Conversely, with decrease in scanning speed, the opposite effects are observed. Wang *et al.* [100] reported similar trend in temperature gradient dependent dendrite growth velocity of CMT WDED Mg-Gd-Y-Zn-Zr. Mg dendrites evolved at a faster rate with enhanced size at regions farther away from melt pool key-hole owing to smaller thermal gradients compared to that at the center of the melt-pool.

Fig. 10**ai** depicts the finite element simulation of temporal increase in the melt pool size with each layer being deposited. Since the convection mode of heat transfer dominates the melt pool heat dissipation, the thermal energy keeps accumulating with each layer being deposited thereby increasing the size of fusion zone. As spatial heterogeneity in temperature distribution causes uneven thermal gradients within regions of melt pool, the dendrite growth velocity will also be heterogenous. Phase field simulations of temporal dendrite evolution reveal that at regions far away from the key-hole, hexagonal, snowflake shaped dendrites with enlarged size and prominent secondary dendrite arms appear (right column of Fig. 10**aii)** owing to lower thermal gradient and high dendrite velocity [100]. Here the formation of hexagonal shaped dendrites is ascribed to hexagonal symmetry of Mg. The opposite is observed for the melt pool region directly under the heat source central axis (left column of Fig. 10**aii**). Another possible factor that contributes to profuse dendrite growth farther from the heat source axis is the enhancement in local interfacial energy anisotropy which accelerates the instability of primary dendrite arm and promotes its branching [101]. Evidently, the mutual interaction of multiple secondary dendrite

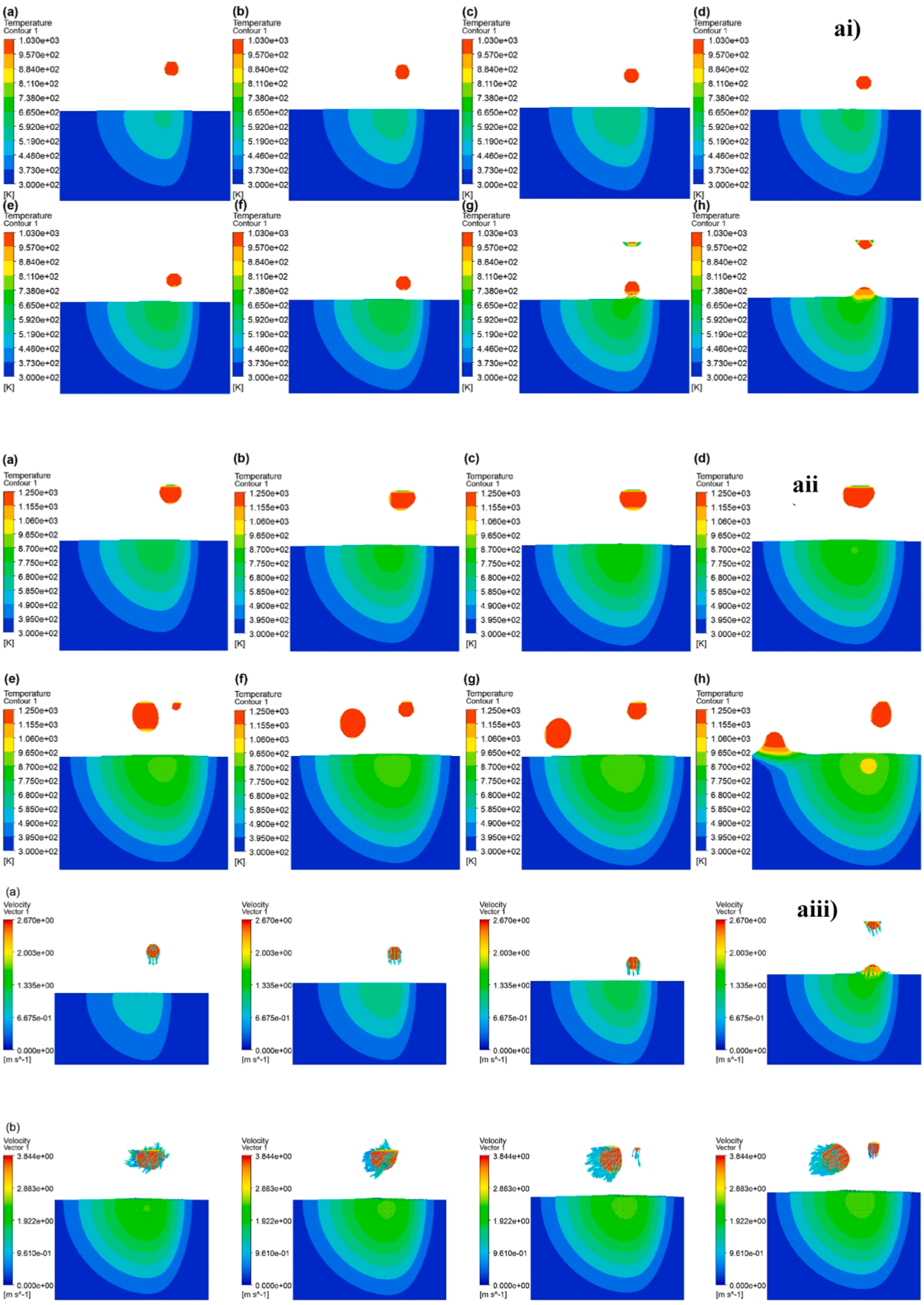


Fig. 7. Numerical simulation of CMT WDED droplet transfer for Mg-Gd-Y-Zr at different process parameter regimes (**i**) and (**ii**) at lower input current/arcing phase duration and higher input current/arcing phase duration respectively (**iii**) corresponding velocity of droplets for those lower and higher parameters [95] (*Reproduced with permission from Elsevier*).

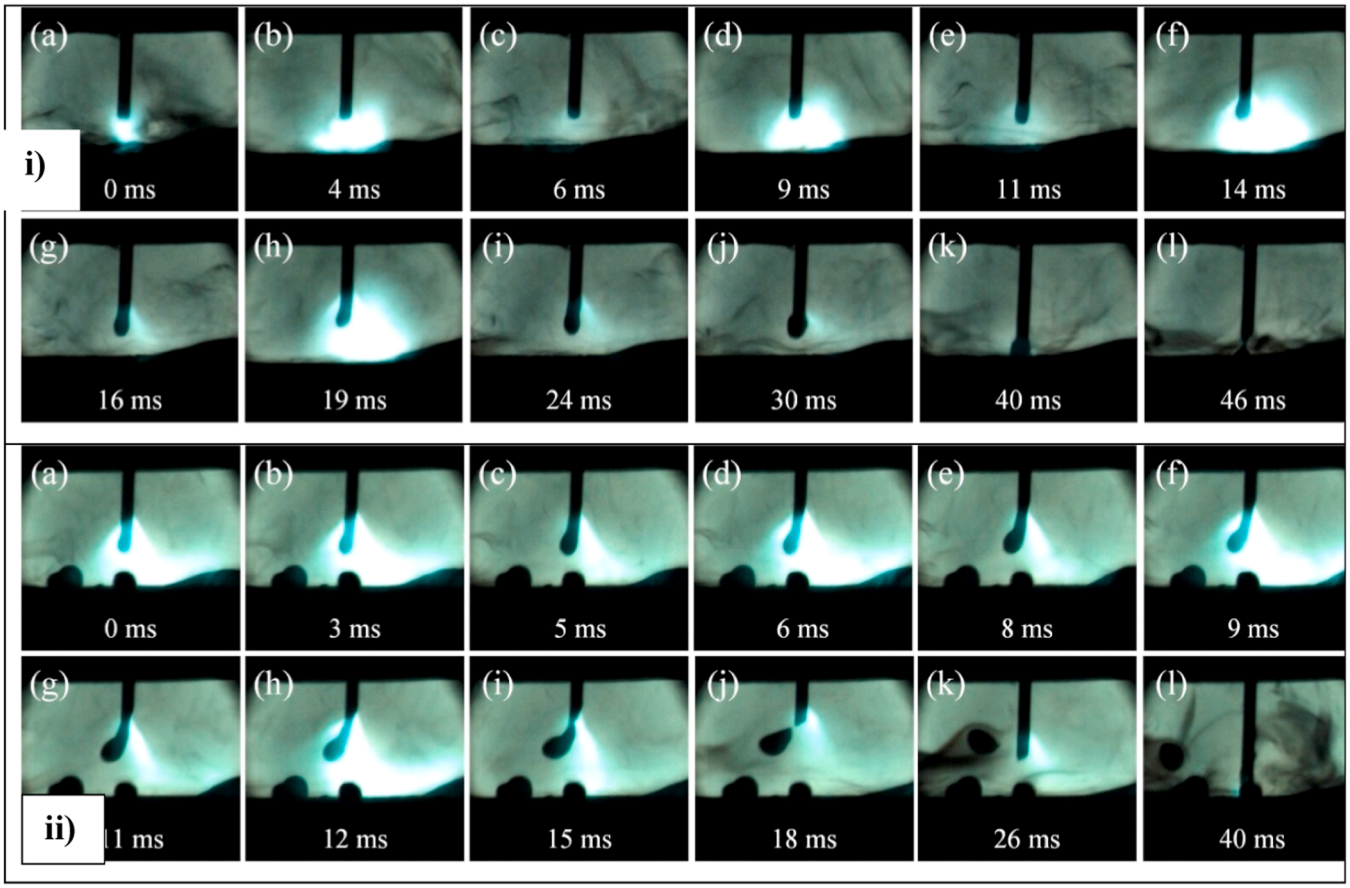


Fig. 8. High speed camera visualization of molten droplet transfer in pulsed CMT of AZ31 alloy at different wire feed rates for a CMT cycle (**i**) 4 mm/min and (**ii**) 5 mm/min [83]. (*Reproduced with permission from Elsevier*).

branches far away from the center of the melt-pool will also create so called "impact effect" to generate asymmetry in hexagonal morphology vis-a-vis their counterparts at the heat source axis.

The transformation rate from the *de facto* columnar dendrites into hexagonal structures is driven by inherent competition between alloy chemistry dependent melt's surface tension anisotropy and crystallographic anisotropy [101]. As there is spatial variation of thermal gradients and cooling rates in CMT WDED, misorientation among the initially formed columnar dendrites manifests in a spatially complex manner with regions of low cooling rate exhibiting high misorientation and vice versa. Additional subtleties in dendrite growth characteristics manifest from the crystal structure of the solute as it modifies the melt pool's interfacial energy and diffusion. CMT process being relatively milder compared to other modes of WDED molten droplet transfer in terms of generating melt pool turbulence, preserves the hexagonal morphology of the dendrite during its evolution, throughout the spatial extant of the melt-pool. In conventional processing of Mg alloys, if the melt pool convection is amplified either via high heat flux or artificial stirring effect, a pronounced asymmetry in dendrite arm morphology manifests [101]. However, the threshold melt pool surface velocity that can destabilize the hexagonal symmetry of dendrites has not yet been determined from experiments or simulations.

3.2. General trends in cooling rate dependent microstructure evolution of Mg alloys

As mentioned earlier, increment in cooling rates causes refinement of dendrites, boosts the dendrite tip velocity, alters their morphology and mitigates the evolution of higher order dendrites. Therefore, in view of the amplified cooling rates in CMT WDED vis-à-vis conventional manufacturing process like casting, the three noteworthy microstructural features in the components fabricated via the former are grain refinement, extended solid solubility and a homogeneous microstructure. Grain refinement is caused by factors like increase in both the undercooling of melt and increased rate of nucleation along with decreased nuclei growth rate. However, this grain refinement happens only when the cooling rates are higher than a critical limit. At lower cooling rates, nucleation is suppressed, and grain growth happens. Enhanced solid solubility is also attributed to high cooling rates, which prevents outward diffusion of microconstituents from the Mg matrix. However, at higher cooling rates, the partitioning of the elements increases due to the rise in the solid-liquid interface velocity [102]. Given the spatially heterogenous cooling rates encountered in a practical CMT WDED process, the secondary precipitate size distribution of Mg alloys could also be heterogeneous. With an increase in cooling rate up to a threshold, the solute concentration in the liquid melt deviates from that prescribed by the equilibrium phase diagram for a particular temperature. As a result, the liquid phase is enriched with solute, which on cooling would lead to second phase formation. However, if the cooling rates exceeds a threshold level, it results in solute trapping and prevents the formation of precipitates. For example, in Mg-Zr-RE alloys the threshold cooling rate for solute trapping is ~2.5–3.5 K/s [103]. However, this threshold cooling rate depends on the alloy chemistry of the alloy [104].

3.3. Metallurgical challenges of arc based WDED Mg alloys

In a broader sense, Mg alloys are classified as either Mg-Al based and Mg-Zr based systems [104]. To improve their mechanical performance and processability, rare earth (RE) elements are often alloyed to both

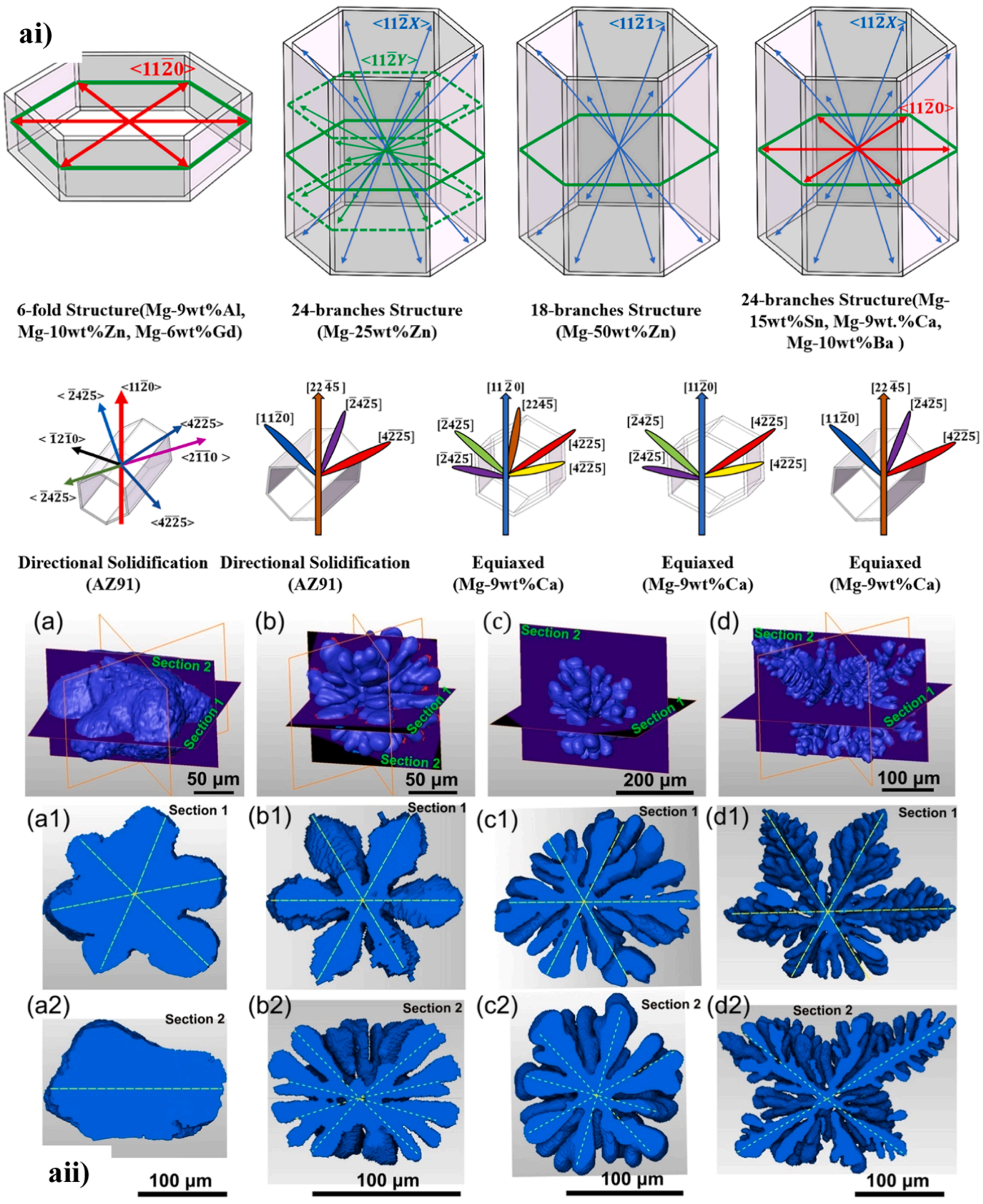


Fig. 9. Dendrite evolution of magnesium alloys along different orientations in casting. (**ai**) Alloy chemistry dependence of multifold branch structures (**aii**) enhancement in dendrite branching with increase in Zn concentration for Mg-Zn alloy [97]. (*Reproduced with permission from Springer Nature*).

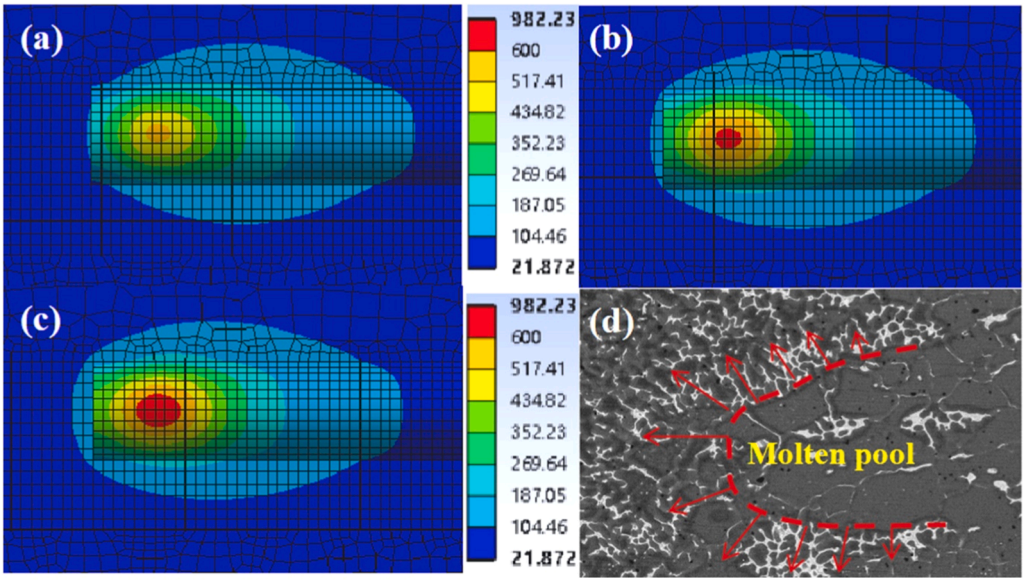


Fig. 10. Temperature distribution and temporal dendrite evolution in the melt pool of CMT WDED Mg-Gd-Y-Zn-Zr [100]. (*Reproduced with permission from Elsevier under CC-BY-NC-ND−4.0*).

these Mg based systems thereby promoting diversity in alloy design for desired applications. Since CMT WDED is an extension of fusion welding process, the metallurgical challenges encountered when this technique is applied for processing Mg alloys can be classified into two different categories as follows. First, if the process parameters are not optimized it will lead to generation of spectrum of defects like residual stresses, porosity, poor fusion, cracking issues and spatter [18,19]. Second, the microstructure generated will be heterogeneous because of spatially asymmetric melting of the substrate under the thermal energy source. The fusion zone (FZ) where complete melting of the material occurs, undergoes solidification to form long columnar grains. While the partially melted zone (PMZ) next to FZ has a microstructure with pronounced texture, heat affected zone (HAZ), which is in the immediate vicinity of PMZ undergoes alloy chemistry dependent solid state phase transformations and exhibits nearly equiaxed microstructure [18]. Among the metallurgical issues mentioned above, porosity, solidification and liquation cracking, columnar grain formation in fusion zone deserve special attention.

3.3.1. *Porosity in fusion zone of Mg alloys*

The leading cause of porosity is the dissolution of Hydrogen (H) in melt, which gets picked up from moisture present either on the filler wire and substrate or from the shielding gas. Due to the asymmetry in H solubility among solid and liquid phases in Mg alloys, with it being higher in latter, liquid metal is enriched with H due to its rejection at the advancing solid/liquid interface, with progressive solidification. Once the H concentration at the solid/liquid interface exceeds the liquid solubility threshold, it causes pore nucleation [105]. Since Mg melts have the lowest density, they decelerate the drifting velocity of the pores to the melt pool surface. This aids in coalescence of pores nucleated at spatially varying locations through the driving force provided by melt pool convection. If the melt pool convection in CMT WDED is amplified by the factors like Lorenz force and Marangoni force, porosity volume fraction is enhanced due to two reasons, which are as follows. First, local solute rejection and its transport away from the solid/liquid interface leads to decrease in melting point and lower undercooling so that solidification volume fraction decreases in the vicinity. Second, pore enlargement occurs due to absorption of H atoms transported from elsewhere via fluid flow [105]. Alternately if the convective forces are not dominant, pores are trapped at interdendritic regions. Another additional factor for porosity is the formation of key holes due to vaporization of low boiling point elements like Mg, Al and Zn.

3.3.2. *Solidification cracking of Mg alloys*

Solidification cracking is profoundly affected by the Mg alloy chemistry. Alloys that have a wider solidification range have a large mushy zone and are hence likely to crack [105]. As the molten metal cools, the shrinkage in volume triggers tensile stresses and if these stresses exceed the material's tensile strength, cracks form. Hence, if the liquid metal is constrained to flow into the cracks formed in between intricate columnar dendritic channels during such thermally induced volume contraction, cracking can be mitigated. Mg alloys that exhibit deep eutectics in which liquid phase is stabilized to the lowest temperature possible and offer better partitioning ability of solute elements at the solid-liquid interface have narrow mushy zone and hence better cracking resistance. However, in the context of CMT WDED, where non-equilibrium solidification conditions prevail and spatially varying thermal gradients cause formation of columnar grains in the fusion zone, solidification cracking can be mitigated by incorporating grain refiners in filler wire. Grain refinement leads to the formation of equiaxed grains, whose boundaries are more effective in absorbing thermal contraction stresses compared to boundaries of columnar grains. Moreover, there are more boundaries in the refined microstructure, which provide enhanced channels of feeding liquid metal to heal solidification cracks [105].

3.3.3. *Liquation cracking of WDED Mg alloys*

Mg alloys pose serious liquation cracking issues because of their high coefficient of thermal conductivity, greater solidification shrinkage and remarkably large thermal shrinkage due to their high coefficient of thermal expansion [105]. The phenomenon of liquation cracking is intergranular in nature and is prominent among Mg alloys exhibiting lower eutectic temperature. When the PMZ is undergoing cooling, the accumulation and coalescence of liquid film at the grain boundaries (GB) of multiple grains cripples the material's ability to resist tensile stress generated due to shrinkage, leading to liquation cracking. The formation of a continuous network of liquid film at GB is attributed to the following two factors. Preferential segregation of impurities and solutes to GB depress melting point locally vis-à-vis grain interior. Secondly at high temperatures, GB wetting with liquid phase is facilitated by local eutectic reactions between second phase precipitates and matrix

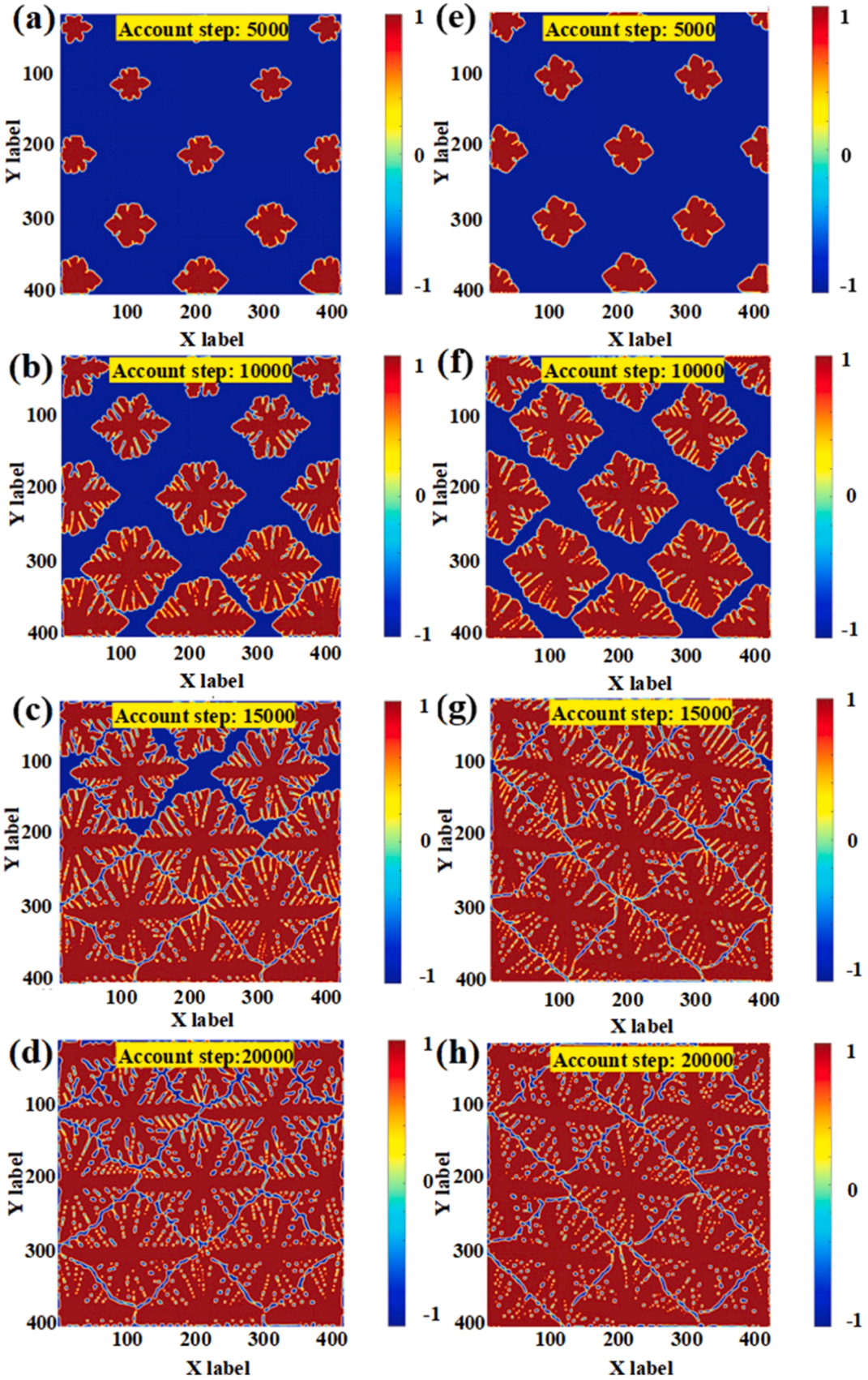


Fig. 10. (*continued*).

[105] . In Mg alloys, commonly observed Mg-Al and Mg-Zn intermetallic second phase precipitates have a higher melting point compared to pure Mg. During thermal cycling, these intermetallic phases facilitate constitutional liquation with the surrounding Mg matrix by forming a

diffusion couple [105]. Given the steep thermal gradients and heat accumulation in WDED process, diffusion coefficients are enhanced thereby contributing to constitutional liquation. These conditions are ideal to further accelerate precipitate dissolution in the eutectic reaction with Mg matrix [105]. Generally, diffusion controlled precipitate dissolution rate is proportional to the square of the average precipitate radius [105]. Since thermal cycling in WDED coarsens the precipitates, large sized precipitates have a higher propensity to form local eutectic liquid film. From the microstructure point of view, the goal of CMT WDED of Mg alloys is to obtain fine grains throughout the build component. Due to the high fraction of GB area and their pronounced average GB curvature, fine grains obviate GB wetting with liquid phase whereas coarser grains accelerate the propagation of liquid across the GB. Also, the CMT process parameters should be optimized in such a way that the amount of heat accumulation in the component due to repeated thermal cycling is kept minimal to avoid secondary phase coarsening.

3.3.4. *Fusion zone microstructure evolution in Mg alloys during CMT WDED*

The microstructural evolution in FZ of Mg alloys is initially characterized by formation of Mg rich primary dendrites whose morphology and sizes are determined by the prevailing cooling rate. Due to solute partitioning to the interdendritic regions, secondary solidification is initiated. Since a majority of the solute elements engage in eutectic reaction with Mg, intermetallic phases form during the terminal stage of solidification [105]. In WDED process, thermal gradients dominate the solidification rate to trigger epitaxial growth of columnar grains. However, it is possible to facilitate the transition of these columnar grains to equiaxed morphology via the following two approaches. First, the formation of large constitutional supercooling zone ahead of solid/liquid interface should be facilitated and two, heterogeneous nucleation in the zone of constitutional undercooling must be fostered. In the first approach, alloy design and CMT process play a vital role. The solutes, which not only increase the slope of the solvus curve and partitioning coefficient but also enhance their solubility in Mg, augment the constitutional supercooling zone. CMT technique ensures the reduction in thermal gradients and concomitant enhancement in solidification rate. Although the second approach to grain refinement through inoculation is more popular in Mg castings, the recent advancements in WDED guarantees feasibility of incorporating composite filler wire for inoculation [88]. Additional techniques for grain refinement include application of *in situ* external fields that vigorously stir the melt pool and create dynamic conditions for solidification [72,73]. Among such strategies, pulsed arc electrical sources, magnetic and mechanical oscillations of power source, laser pulses and ultrasonic waves are popular for effective integration with the CMT WDED experimental set up.

4. Recent advances in microstructural evolution investigations of CMT WDED Mg alloys

4.1. *Mg-Al based alloys*

4.1.1. *Microstructural attributes*

Fig. 11**a to c** illustrate the heterogenous grain size distribution (GSD) across the deposited layers of CMT ATZM31 Mg alloy thin wall. Fig. 11**a** depicts GSD in which the interlayers between first/second and second/third deposited layers exhibit certain fraction of fine grains. As the deposition progresses, the interlayers exhibit formation of columnar grains (Fig. 11**b and c**) due to continuous heat accumulation, which also causes pore formation in the uppermost layers [106]. Fig. 11**d** indicates the temperature distribution of the substrate gradually decreases after first few deposition layers, to finally converge to a specific temperature as shown by dotted line. The three distinct zones of heating, constant temperature and cooling are the consequence of transient thermal energy distribution of this process. Finite element simulation of the temperature distribution reveal that during deposition of first layer, thermal gradient is insignificant compared to that of last layer (see Fig. 12) which explains the generation of equiaxed grains near the substrate whereas columnar grains are formed at the middle and top regions of the built wall. Fig. 11**e to g** indicates that the average grain size increases as the deposition progresses, which is also indirectly determined from hardness measurements that reveal a decrease in hardness along the build direction [106]. Similar trends in grain size variations along the build direction was reported [107,108] for AZ31 alloy. Moreover, the microstructure has a strong (0001) texture.

The formation of equiaxed grains near the bottom region of the built component is due to larger constitutive cooling achieved locally, which exceeds the critical undercooling for nucleation. The steeper growth rate of solid/liquid interface at the bottom along with low thermal gradient (see Fig. 12**a**), enables high density of nuclei formation, thereby expanding the constitutional undercooling zone [106]. On the contrary, the constitutional undercooling at the top layers is hindered due to steep thermal gradients (see Fig. 12**b**) and low solid/liquid interfacial growth rate to impart grain growth. In CMT WDED, columnar grain orientation also exhibits diversity depending upon the number of layers being built. Due to continuous heat accumulation from multi-layer deposition, melt pool shape changes and alters thermal gradient direction with progressive increase in deposited layers. This orientation change of thermal gradient results in obliqueness of columnar grains with respect to build direction as against initial alignment to build direction [108].

The microstructure evolution pathway in ATZM 31 alloy [106] is different compared to AZ31 alloy [107] owing to differences in alloy chemistry. The addition of Sn alters the solidification pathway for ATZM 31 and thermodynamically favors the nucleation of η-Al_8Mn_5 at GB with α-Mg being the primary phase. Here, Sn inhibits partitioning of Al to Mg and as a result, the formation of β-$Mg_{17}Al_{12}$ eutectic is avoided. Conversely, in AZ31 alloy, the microstructure in the as-deposited state comprises of α-Mg matrix, eutectic structure of α-Mg + β-$Mg_{17}Al_{12}$ along the grain boundaries and fine η-Al_8Mn_5 inside the α-Mg matrix [108]. Due to slow cooling rate, the secondary dendrite evolution is profound at the top region of the wall as compared to middle and bottom regions. Hence, the volume fraction of interdendritic eutectic α-Mg + β-$Mg_{17}Al_{12}$ decreased concomitantly to increase in average size of primary dendrites from bottom to top regions in the building direction.

The role of transient temperature profile during in CMT WDED microstructural evolution, specifically precipitate morphologies for AZ31 alloy is depicted in Fig. 13. Initially, coarser Al_8Mn_5 exists in the microstructure along with liquid phase since this intermetallic phase's melting point is approximately closer to the boiling point of Mg. Al_8Mn_5 phase provides a driving force for nucleation of α-Mg due to their similar lattice parameters [109]. As the temperature decreases, coarser low melting point $Mg_{17}Al_{12}$ eutectic phase nucleates at the GB. However, during subsequent increment in temperature, $Mg_{17}Al_{12}$ dissolves into the matrix and conversely with decrease in temperature, forms a composite phase with existing Al_8Mn_5 particles. As the transient temperature during reheat cycles is higher than recrystallization temperature (300° C), it not only results in simultaneous recrystallization of α-Mg grains but also refinement of initial coarser eutectic phase at GB with increment in cycling. It is also worth mentioning that the electromagnetic forces generated in CMT WDED filler wire creates a stirring effect in the melt pool leading to fragmentation of dendrites and causes grain refinement.

4.1.2. *Strategies for obtaining equiaxed microstructure in Mg-Al alloys*

In CMT based processes, welding torch speed, input current, voltage and filler wire feed rate are the critical parameters that affect thermal energy input. By synergistically increasing all the above parameters, Ren et al. have shown that the melt pool width can be increased with concomitant linear decrease in HAZ [110] and resulted in columnar to equiaxed grain transition. Nevertheless, single bead deposition-based studies [110] do not ideally replicate the multilayered deposition

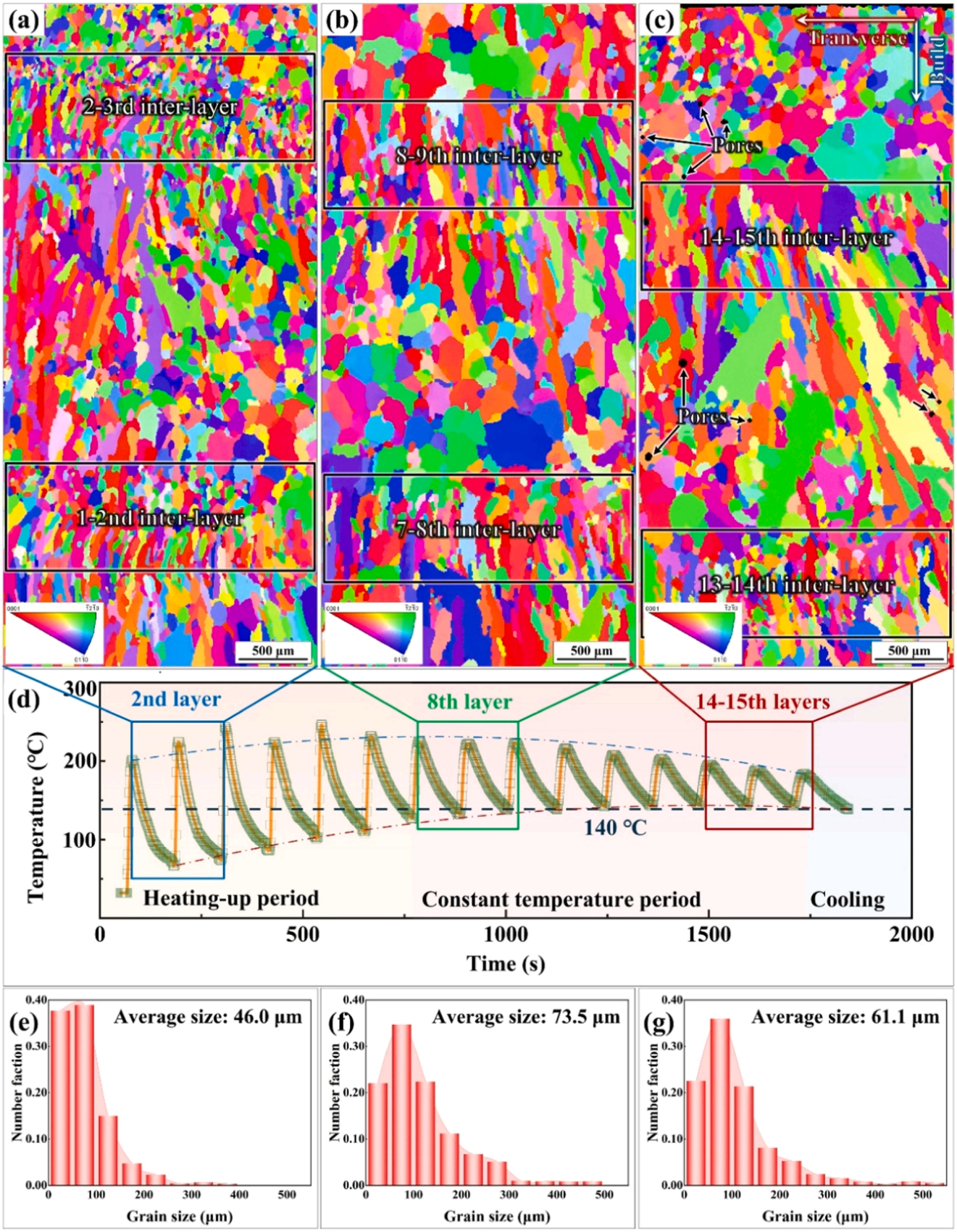


Fig. 11. **(a)-(c)** Heterogeneous grain size distribution of ATZM31 Mg alloy across various deposited layers depicted through inverse pole figure maps from EBSD characterization. **(d)** temperature distribution of substrate across the deposition time and **(e) - (g)** grain size statistics obtained from build wall at bottom, middle and top regions [106] . (*Reproduced from Elsevier under CC BY-NC-ND 4.0*).

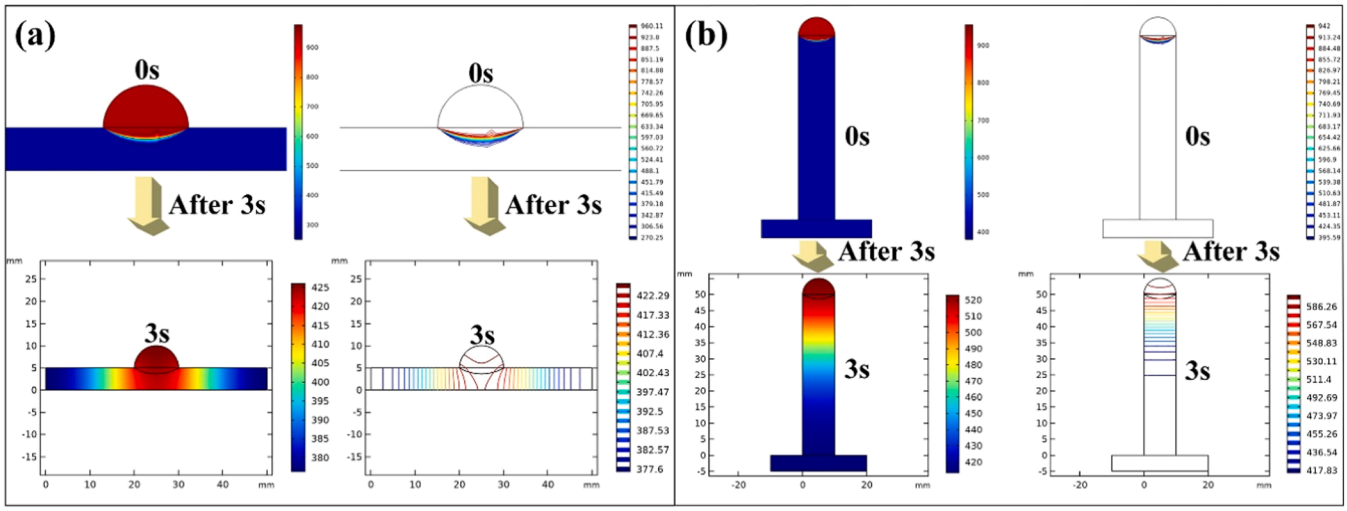


Fig. 12. Finite element simulation depicting the temperature distribution of CMT WDED ATZM31 Mg alloy at the before and after 3 s of layer deposition (**a**) for the first layer (**b**) for the last layer (fifteenth layer) [106]. (*Reproduced from Elsevier under CC BY-NC-ND 4.0*).

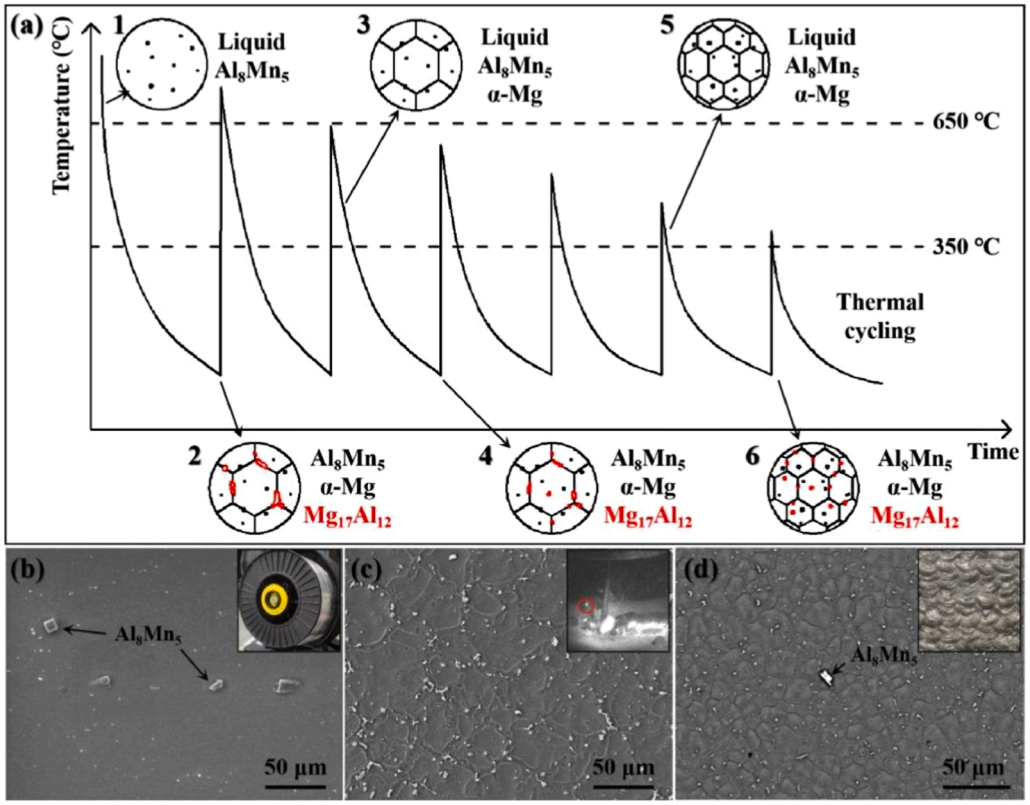


Fig. 13. (**a**)Temporal evolution of microstructure for AZ31 alloy due to transient thermal cycling in CMT WDED fabrication and (**b**),(**c**), (**d**) represents schematic microstructure during the thermal cycling as indicated by black arrows in a) [109]. (*Reproduced from Elsevier under CC BY-NC-ND 4.0*).

conditions in WDED. Similarly, weaving the wire arc during fabrication was noted to promote grain refinement of α-Mg and caused uniform dispersion of fine $Mg_{17}Al_{12}$ eutectic structure. Here the forced convection conditions that promote a stirring effect, causes reduction in melt pool thermal gradient and enhances constitutional supercooling [111, 112]. The stirring effect causes disintegration of columnar dendrites, where stronger stirring yields greater grain size refinement. While provisioning of forced convection through lateral Ar gas shielding has marginal effect on formation of equiaxed microstructure [113], depositing the layers with a smaller filler wire diameter was noted to have remarkable effect on grain refinement [114]. Similarly, CMT being effective in minimizing heat accumulation in build component, smaller dwell time between successive layers can also lead to equiaxed microstructure albeit with grain size variation along the build direction [115–118]. Equiaxed grains can also be obtained by dynamic control of current and voltage waveforms in CMT WDED process. However, establishing the regimes of spatter free metal deposition requires extensive design of the experimental approach for optimizing the arc current and voltage parameters [119–121].

4.2. Mg-RE based alloys

4.2.1. Microstructural attributes of Mg-Gd-Y-Zn-Zr alloys

Mg-Gd-Y-Zn-Zr alloy's microstructural evolution is sensitive to heat accumulation during layer wise deposition in CMT process. Amongst the process variables, filler wire feeding speed and welding speed have a contrasting effect on heat accumulation in the built component. Minimizing the heat accumulation and heat input in the built volume through a combination of low filler wire feeding speed and higher welding speed is an effective strategy to lessen both residual stresses, dislocation density and texture [122,123]. Despite optimized filler wire feeding rate and welding speed, heterogeneous dislocation distribution during processing affects the microstructural evolution in a complex manner. Typically, the dislocation density is highest in the initial built layer and lowest in the middle layers.

Fig. 14 illustrates melt pool size evolution for the first ten layers of the build in a CMT WDED fabricated Mg-Gd-Y-Zn-Zr alloy. In Fig. 14**b,e, h** the red and black dotted lines represent the melt pool and remelt zone size respectively. It is evident that the volume of melt pool is increasing with each deposited layer. The progressive heat accumulation coupled with asymmetric fusing of metal surrounding the melt pool will decrease the thermal gradient. The magnitude of heat accumulated will reach a stagnation point because with increase in layers being deposited, the thermal conductivity of already solidified layers will aid in dissipation of accrued thermal energy [123]. The microstructure in this alloy comprises of grains whose size is heterogeneously distributed with significant variation across each of the first ten deposited layers [123]. The origin of this grain size variation across layers can be traced back to spatio-temporal evolution of temperature and cooling rates. Specifically, the cooling rates exhibit two orders of magnitude difference between initial layer and eleventh deposited layer. Therefore, the as-solidified microstructure exhibits spatially varying cooling rate dependent precipitation of secondary phases in α-Mg matrix. Due to high cooling rates in the initial layers, their grain boundaries are dominated by a network of long period stacking order (LPSO) 18 R structures (that create a coherent interface with α-Mg) and minor fraction of Mg_5(Gd, Y, Zn) [123]. On the contrary, above the tenth layer where cooling rate is the least, the second phase is the $Mg_{24}(Gd,Y)_5$ phase. However, in the study by Bai et al., [124], it is reported that Mg_5(Gd,Y) did not precipitate owing to its low formation enthalpy that necessitates slow cooling process for its nucleation and growth. Likewise in another study, a eutectic structure of $(Mg, Zn)_3$(Gd,Y) precipitated at GB [125]. Therefore, in Mg-Gd-Y-Zn-Zr system, the eutectic phase formation at GB is dictated by local kinetics of the non-equilibrium solidification process.

Fig. 15 depicts the microstructural evolution for CMT WDED Mg−8.1Gd−2.6Y−0.7Zn−0.5Zr alloy [126]. Here, eutectic $(Mg, Zn)_3$(Gd, Y) is the predominant phase that precipitated along the α-Mg GB similar to that in [127, 128]. LPSO γ' phase can be observed only with grain interiors in the middle region of the build component while minor fraction of RE rich cubic $(Gd,Y)H_2$ was uniformly distributed within the grains along the entire build length [126,129]. Along the build direction, the microstructure exhibits banded structure with

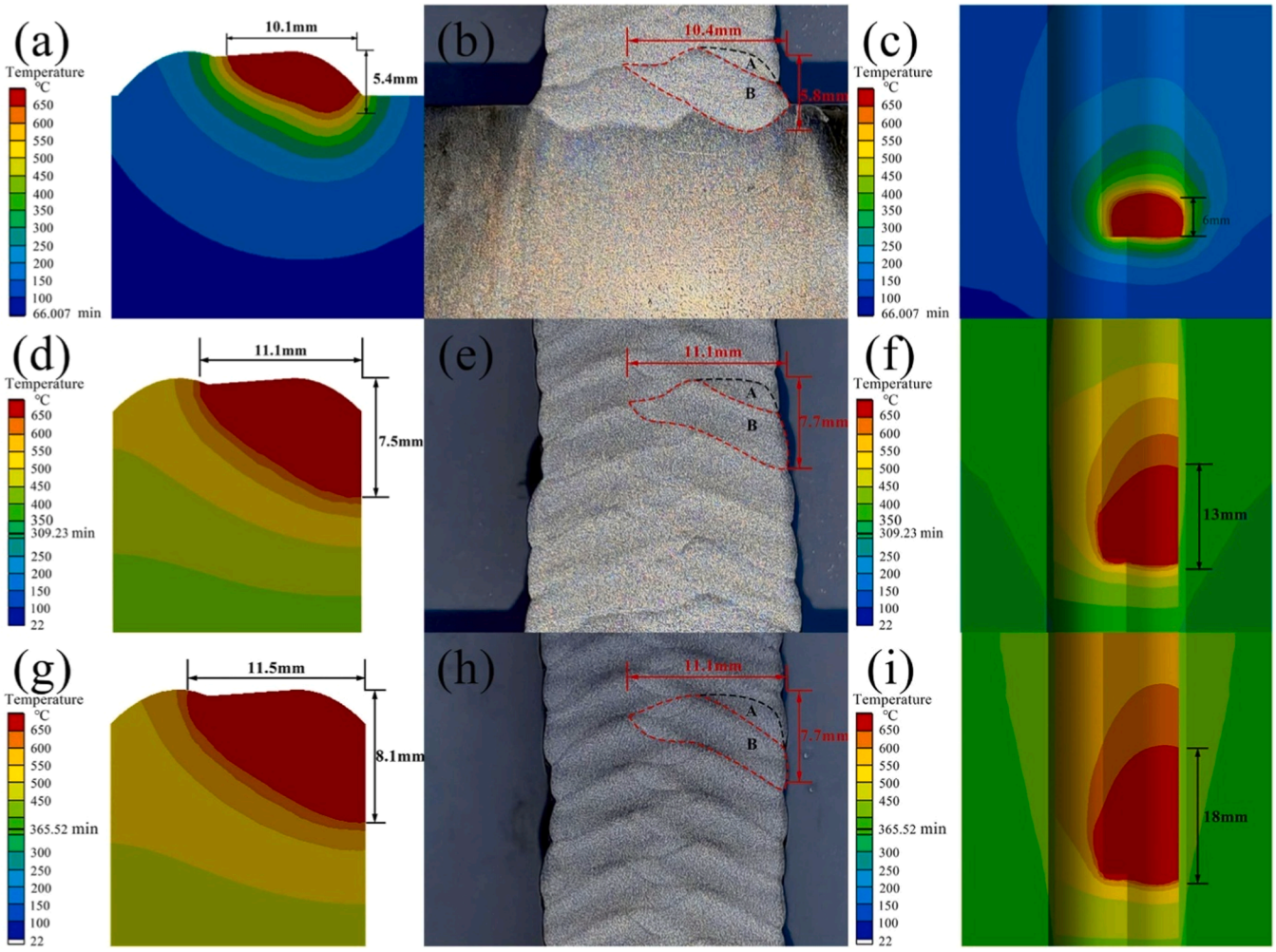


Fig. 14. Melt pool size evolution with increase in layers depicted in cross section and top views for CMT Mg−9.2Gd−3.2Y−2Zn−0.4Zr alloy (**a-c**)first layer (**d-f**) fifth layer and (**g-i**) tenth layer [123]. (*Reproduced with permission from Elsevier*).

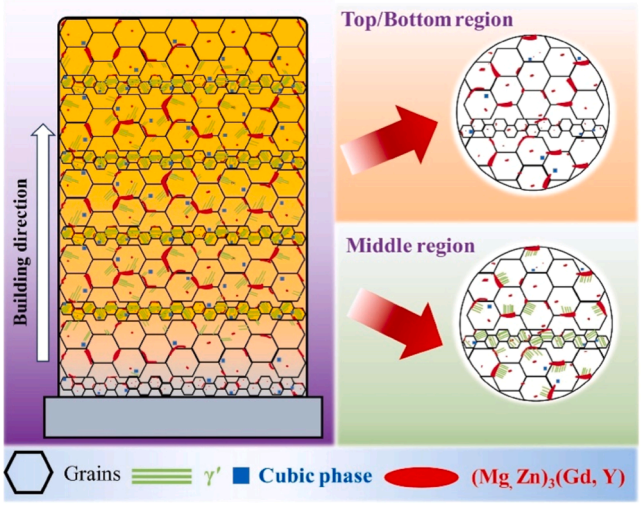


Fig. 15. Schematic illustrating general microstructural evolution in build direction for CMT WDED processed Mg−8.1Gd−2.6Y−0.7Zn−0.5Zr alloy [126]. (*Reproduced with permission from Elsevier under CC BY-NC-ND 4.0*).

alternate coarse and fine grains forming within melt pools and melt-pool boundaries respectively [130]. Apart from alloy chemistry and standard CMT process variables, CMT process modes have remarkable influence on phase formation and grain size distribution in this alloy system [125]. While CMT-pulse mode enhances heat input by introducing current pulses compared to standard CMT process, CMT-advanced mode results in a relatively reduced thermal input as the arc fluctuates between electrode-positive and electrode-negative polarities. Hence compared to pulse and standard modes, application of CMT-advanced mode causes smaller grain size, less oxidation and porosity during processing of Mg−8.8Gd−3.9Y−0.85Zn−0.45Zr alloy. However, CMT pulse mode enabled formation of a well-connected eutectic structure at GB but the caveat here is that this process is more prone to defect formation.

Despite a significant difference in alloy chemistries and CMT process parameters, this alloy system was reported to form equiaxed grains with alternating bands of coarse and fine grains in melt pool and melt-pool boundaries respectively. However, both the crystallographic nature of eutectic structure at GB and its spatial connectivity exhibit wide diversity. Also, the mechanism of LPSO structure formation is not clear although it is evident that process parameters that result in high heat accumulation favor LPSO formation [129]. While Zhao *et al.* [123] and Ju et al. [129] have shown that LPSO phases form at the melt-pool boundaries of the bottom region, Ma *et al.* [126] and Zhang *et al.* [127] argued that these phases preferentially form at melt-pool boundaries of middle region in the build direction. One possible reason that can be ascribed to the prominent presence of LPSO phases in bottom region of built layers is the high cooling rate at these locations that enhances supersaturation of RE elements in the α-Mg matrix. Hence this limits the driving force for precipitation of eutectic phase and favors LPSO phase formation. Further, eutectic phase precipitate sizes were found to be large at bottom regions compared to those at the top, since heat accumulation at the top layers aid in dissolution of the eutectic structure [124].

4.2.2. Microstructural attributes of Mg-Y-Nd-Zr alloys

Mg−3.82Y−2.46Nd−0.56Zr alloy's microstructure typically comprises of alternating layers of coarse-grained melt pools and fine-grained melt-pool boundaries. The equiaxed grains formed have the largest grain size at the bottom region while middle region and top region of build wall were shown to have intermediate and small average grain size respectively [131]. Though the precipitates formed at GB were identical across the build wall, the precipitate density displayed decreasing trend from top zone to bottom zone. The microstructure comprises of micron scale $Mg_{24}RE_5$ precipitates decorated at GB along with nanoscale needle-like Mg_3Nd phases and $Mg_{24}RE_5$ nanocubes in the grain interior. However, minor alloying of Gd ~1.2% to Mg-Y-Nd-Zr system resulted in precipitation of micron scale eutectic network of $Mg_{14}Nd_2$(Y, Gd) along the GB of α-M, while α-Mg grain interior comprises of $Mg_{24}Y_5$ nanoscale particles, $(Gd,Y)H_2$ nanocubes and dispersions of elemental Zr [132]. Another feature of Gd doped alloy is that it exhibits hierarchal evolution of GP zones in α-Mg and their precipitate density increases from top region to bottom region of the build volume [132]. Chen *et al.* [133] noted remarkable change in the precipitate crystallography and the spatial extant of melt-pool boundaries when Mg-Y-Nd-Zr alloyed with Gd, in minor quantities, is processed through various CMT modes like CMT-standard, CMT-pulse, CMT-advanced and CMT-pulse advanced. The spatial extent of remelted region inversely correlates with the energy input in CMT process. As a result, CMT-pulse mode that imparts higher heat input displayed smallest remelt zone whereas CMT-advanced that causes smallest heat input had a wider remelt zone. Likewise, CMT-standard and CMT-pulse advanced having intermediate heat inputs results in intermediate size of equiaxed grain remelt zones. Here, a micron scale eutectic microstructure, which comprises of $Mg_{41}Nd_5$ decorated GB and $Mg_{24}Y_5$ nanoparticles formed in grain interior, forms.

4.2.3. Microstructural attributes of Mg-Nd-Zn-Zr alloys

Mg−2.4Nd−0.3Zn−0.6Zr alloy microstructure comprises of alternating layers of equiaxed coarse grains in the melt zone and equiaxed fine grains in the remelt zone. Due to continuous heat accumulation with increasing number of deposited layers, the grain size increases from bottom to top regions of the build volume. In the as-deposited state, the alloy has $Mg_{12}Nd$ precipitates present at GB along with segregation of MgO and Nd_2O_3 in the vicinity of GB [134].

4.3. Mg-Li based alloys

In CMT WDED Mg−8Li−3Al−2Zn−1Y−0.5Mn−0.5Gd−1Si alloy, the remelt zone size decreased along the build direction with maximum observed at bottom region [135]. As deposited microstructure comprises of lath like α-Mg phase distributed within a network of β-Li phase, Mg-Li-Al and Mg-Li-Zn large micron sized primary precipitates and Al-Mn based dispersoids distributed uniformly in the matrix. The morphology of α-Mg laths exhibit profound variation not only across the build direction but also within melt-pool boundaries and melt pools. In melt-pool boundaries due to faster cooling rates, α-Mg has short rod like morphology, while having long needle like morphology in the top and bottom layers due to faster cooling rates experienced by the melt [135]. Conversely in the middle region intralayer, due to smaller thermal gradient and solidification growth rate, α-Mg displays a combination of long needle like and short coarser rod-like structures. Likewise, the spatial volume fraction distribution of α-Mg and of β-Li phases exhibit cooling rate dependence. At top and bottom regions that exhibit higher cooling rate, smaller fraction of α-Mg phase is obtained compared to that at the middle region of build wall. Similarly, the precipitate density was found to increase from top to bottom region with remelt zones (interlayers) having higher precipitate density (Fig. 16).

However, Mg–10Li–3Al–3Zn [136] microstructure is dominated by β-Li grains with α-Mg distributed along GB with island-like morphologies and fine needle-like secondary phase precipitates within grain interior. Here too, the precipitate density is maximum at the bottom region and the morphologies of the phases exhibit cooling rate dependence with regions of higher cooling rate having finer structure.

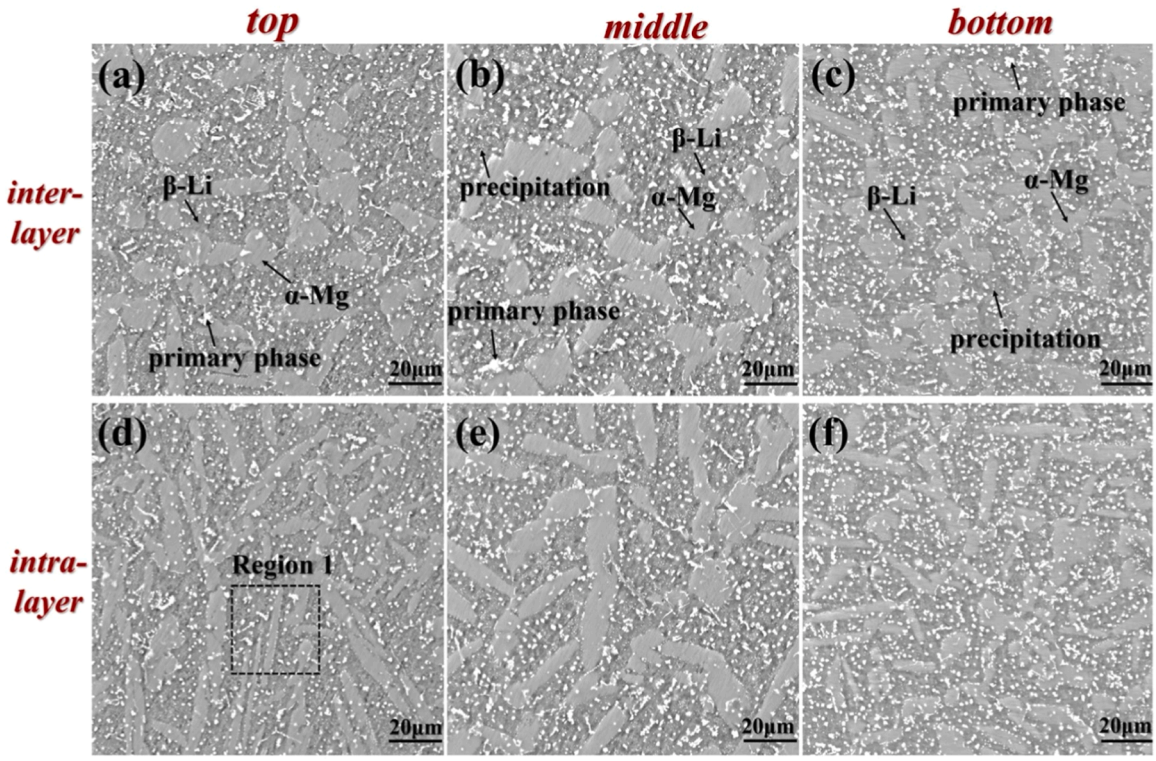


Fig. 16. Microstructural morphologies of Mg-Li based alloy at various regions across the build wall [135]. (*Reproduced with permission from Elsevier*).

5. Supplementary processing techniques for tailoring the microstructure of CMT WDED Mg alloys: Implications for mechanical performance

5.1. Mg-Al based alloys

5.1.1. In situ hammer peening

As evident from previous discussions, heat accumulation during CMT WDED can lead to nonuniform microstructure and causes anisotropic mechanical properties. Therefore, various *in situ* deformation techniques like hammering, friction stir processing, ultrasonic vibrations and laser shock peening are applied to not only refine grains but impart additional strength to the microstructure. Xu *et al.* [137] reported remarkable grain refinement and promotion of grain boundary and dislocation strengthening for *in situ* hammer peened CMT WDED AZ31B Mg alloy single deposited layer (Fig. 17).

Fig. 17 illustrates the experimental setup and the obtained microstructures of hammer peened AZ31B at two different degrees of deformation levels (20% and 35%). Here the hammering action is achieved through a terminal hammering head that is subjected to vibratory forces after a stipulated contact pressure with the deposited layer is established. Once the threshold deformation is achieved, stable hammering of the contact area is facilitated through precise electronic controls [137]. Hence the deformation in the entire deposited layer is realized through accumulation of instantaneous micro deformations in the CMT torch direction. Due to hammer peening, a gradient microstructure is introduced with higher density of dislocations in the top region of the layer exposed to the hammering head. Depending on the deformation force induced, the degree of grain refinement is facilitated by generation of numerous dislocation lines and dislocation walls whose dynamic migration leads to dynamic recrystallization. For a lesser degree of deformation, twining accommodates most of the strain and triggers dislocation and sub grain motion. Conversely, intense deformation at the top contact layer induces drastic migration of medium angle grain boundaries (MAGB) and promotes dynamic recrystallization. Due to such mild and severe deformation treatments leading to grain refinement and dislocation strengthening, the microhardness of the deposited alloy enhanced by 17.4% and 31.7% respectively [137]. Fang *et al.* [138] successfully extended the *in situ* hammer peening technique for multilayer walls and concluded that it not only reduced the mean grain size by ~50% but also enhanced the yield strength (YS) and ultimate tensile strength (UTS) by 37% (from 102.6 to 140.6 MPa) and 8.1% (from 239.8 to 259.2 MPa) respectively. Hence CMT WDED can be synergized with *in situ* hammer peening for improving the mechanical properties of the build.

5.1.2. In situ Friction stir processing

Fig. 18 illustrates the gradient microstructure obtained when interlayer friction stir processing (IFSP) is combined with CMT WDED. By combining deformation and thermal cycling protocols, each of these respective techniques will alter the microstructure of previously deposited layer in a heterogeneous manner. The as-deposited layer's microstructure comprising of coarse eutectic β-$Mg_{17}Al_{12}$ at α-Mg GB and η-Al_8Mn_5 in grain interior, will be subjected to grain refining, dissolution of eutectic structure and fine-tuning Al-Mn intermetallic precipitate size due to severe plastic deformation caused by IFSP [139]. Several mechanisms like strain induced dynamic recrystallization/dynamic recrystallization, which is induced by formation of micro shear bands, contribute to this grain refinement. Similarly, coarse eutectic phase dissolution at GB occurs due to intense heat generated by tool friction leading to local temperature exceeding the eutectic phase melting point. In the next phase, when subsequent layers are deposited via CMT WDED, a portion of the previously deposited stir zone undergoes remelting and the region underneath CMT torch exhibits considerable grain growth while the bottom portion of stir zone is unaffected by thermal cycling and has fine grains. During remelting of the stir zone, second phase particles are uniformly distributed into the α-Mg matrix. On performing IFSP again on this remelt region, grain refinement in the local vicinity is promoted there by creating alternate layers of coarse grained and fine-grained regions in stir zone. Due to such a gradient microstructure,

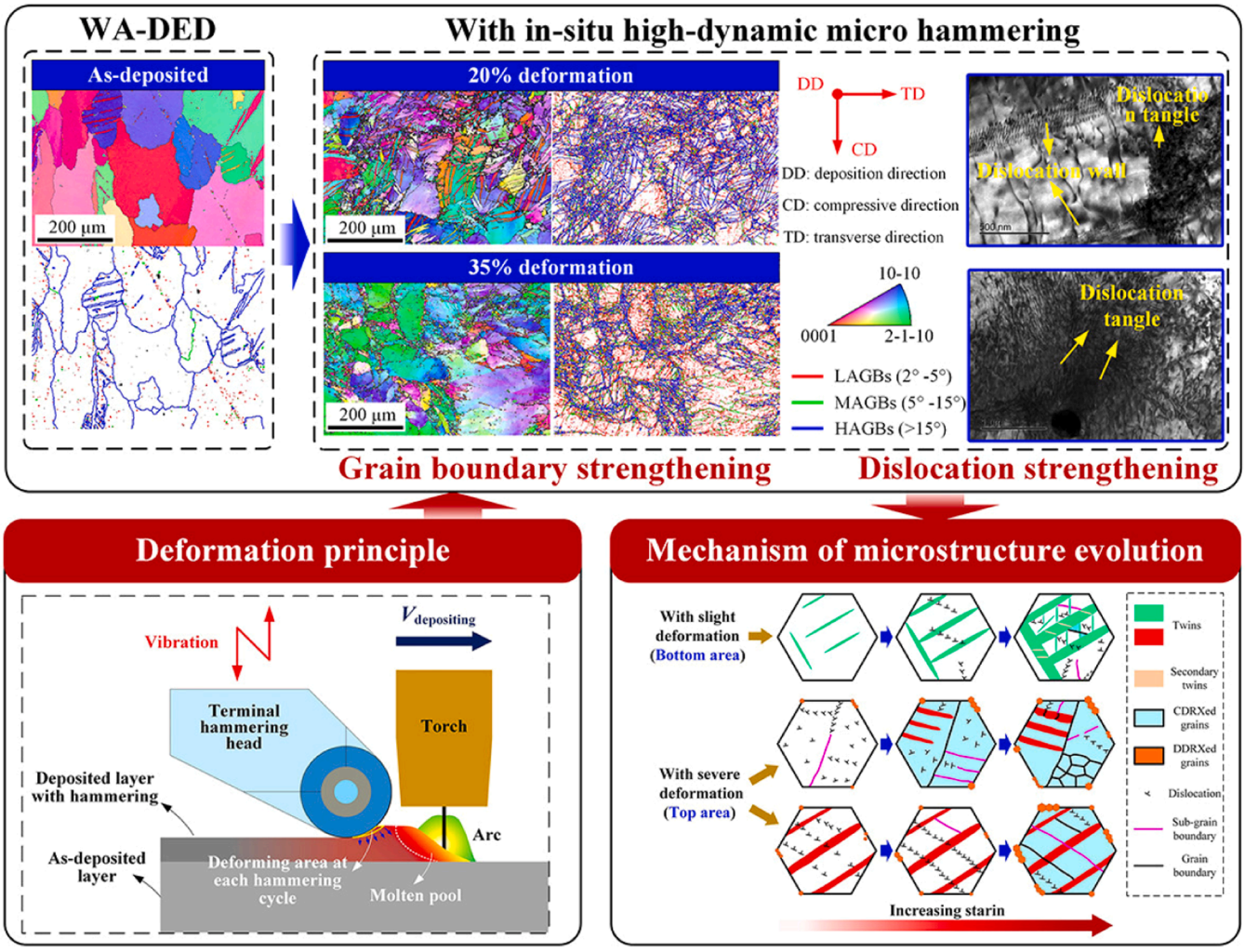


Fig. 17. Schematic illustrating the mechanism of grain boundary and dislocation strengthening for *in situ* hammer peened CMT WDED AZ31B Mg alloy [137]. (*Reproduced from Elsevier under CC-BY-NC-ND 4.0*).

YS in the deposition and build direction increase by 10% (284–315 MPa) and 22.7% (264–324 MPa), respectively [139]. Likewise, elongation enhances by 50% and 53% respectively, in transverse and build directions. Therefore, combining IFSP to CMT synergizes multiple mechanisms like grain refinement, eutectic structure dissolution and gradient microstructure and improves the mechanical properties of components.

5.1.3. Ultrasonic vibration assisted CMT WDED

Fig. 19 depicts the mechanism of grain refinement on application of ultrasonic vibration (UV) during CMT WDED. The melt pool generated by CMT heat sources without UV is characterized by its large volume, low velocity of fluid flow and high temperature gradients. Here grain growth happens epitaxially in the direction opposite to that of temperature gradient (perpendicular to melt-pool boundaries). With increase in build height, heat accumulation amplifies and leads to formation of large columnar grains. Conversely, UV induces cavitation bubbles in the melt pool whose subsequent series of compression and rarefactions by ultrasonic wave propagation [140] leads to the dynamic instability of bubbles and their final rupture. The energy released after the bursting of such cavitation bubbles burst is utilized to fragment the long columnar dendrites. Additionally, the dynamics of formation and collapse of cavitation bubbles enhances fluid flow in the melt pool, which promotes effective convective heat transfer and exchange of solutes. In a nutshell, UV promotes two critical factors for grain refinement, which is as follows. First, it enhances constitutional supercooling through high pressure generated from cavitation bubble collapse, which causes a decrease in critical free energy for nucleation. Second, it enhances the wettability of second phase particles, which fosters heterogeneous nucleation [140].

Yi *et al.* [140] integrated *in situ* UV with CMT WDED and observed columnar to equiaxed transition (CET) in the AZ31 Mg alloy. UV was shown to be more effective in promoting CET at the bottom and middle regions of build wall. Though columnar grains were also eliminated in the top region, the equiaxed grains are much coarser at the top compared to that at the bottom and middle regions. The reason for marginal effectiveness of UV in top region can be ascribed to the experimental setup involving mounting the UV platform below the substrate. Therefore, ultrasonic wave propagation ability diminishes with increase in the build height. However, two additional microstructural benefits accrued through UV are as follows. First it refines the secondary phase precipitate (η-Al_8Mn_5) and uniformly disperses it in the α-Mg matrix. Second, it refines the coarser eutectic $Mg_{17}Al_{12}$ phase and prevents liquation cracking of the GB. Due to such unique combination of grain size and precipitate size refinement along with mitigation of thermal cracking from UV treatment, there is an enhancement in the mechanical properties of AZ31 alloy compared to that which is not treated with UV. Specifically, microhardness, UTS and elongation increases by ~12.6%, ~30.8%, and ~114.2% respectively after UV treatment [140].

Similar enhancement in mechanical properties and reduction in

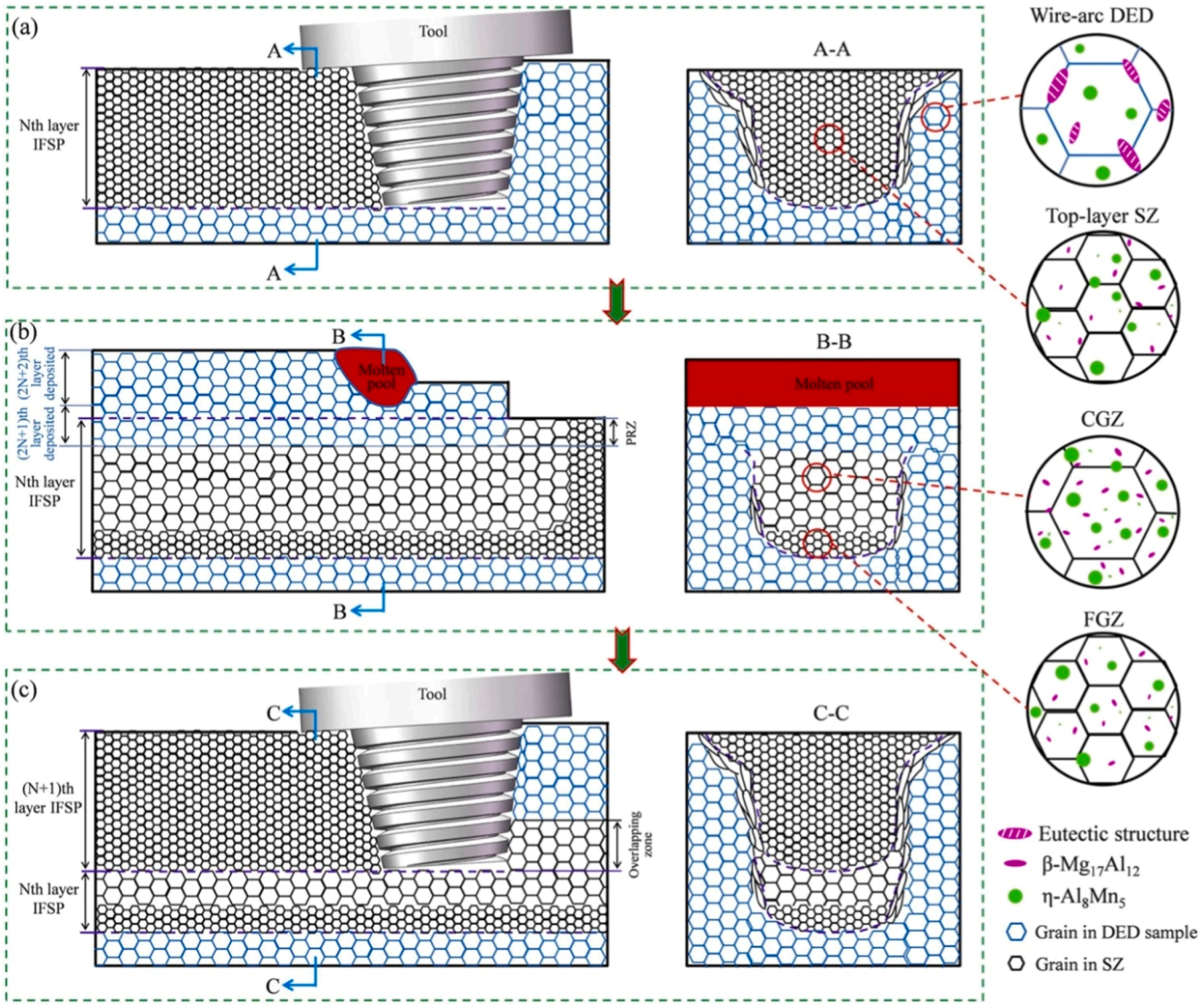


Fig. 18. Schematic illustrating grain refinement and layer wise microstructural evolution of AZ91 Mg alloy when interlayer friction stir processing is combined with CMT WDED [139]. (*Reproduced with permission from Elsevier*).

mechanical anisotropy along CMT travel and build directions are reported by other studies that employed UV as supplementary technique to CMT WDED [141–144]. The specific mechanism of increase in the tensile properties for UV treated AZ31 is as follows. Fig. 20 depicts the microscale mechanism for enhancement in tensile properties of UV treated AZ31 alloy through synergy of various microstructural attributes that transform hybrid fracture mode of the as-deposited specimen to ductile fracture. First, ultrasound field not only decreases the porosity, but also transforms high aspect ratio irregular lack of fusion (LoF) defects into spherical pores. Hence, lower number of pores and LoF defects prevent void nucleation and coalescence leading to fracture. Second, cavitation and acoustic streaming effects [144] refine the grain and precipitate sizes thereby eliminating stress concentration at the α-Mg matrix and precipitate interfaces. Likewise, cavitation aids in generation of several dislocations, twins and high angle grain boundaries (HAGB), which contribute to multiple strengthening mechanisms like Hall-Petch strengthening, low angle grain boundary (LAGB) strengthening and dislocation strengthening. The complex interactions between these mechanisms during tensile deformation provides highly tortuous paths for crack propagation.

Ultrasonic vibration propagating through the molten pool generates alternating compression and rarefaction pressure cycles, which lead to cavitation phenomena involving nucleation, growth, and implosive collapse of microscopic bubbles within the melt. In addition, ultrasonic treatment induces acoustic streaming, which refers to the steady-state fluid flow generated by the attenuation of ultrasonic waves in the molten metal. The collapse of cavitation bubbles locally generates extremely high pressure and temperature pulses along with shock waves and microjets. These fractures mechanically fragment growing dendrites, which are then carried away by acoustic streaming and subsequently act as heterogeneous nucleation sites during solidification. Consequently, the nucleation density increases significantly, thereby promoting the formation of fine equiaxed grains [145].

Additionally, acoustic streaming enhances melt-pool convection and improves heat and mass transfer within the fusion zone. This intensified fluid flow homogenises temperature and solute distribution, suppresses constitutional segregation, and reduces local thermal gradients. The reduction in thermal gradient, coupled with enhanced solute redistribution, facilitates constitutional supercooling ahead of the solidification front, thereby promoting heterogeneous nucleation and suppressing epitaxial columnar grain growth [146] Furthermore, the combined effects of cavitation-induced dendrite fragmentation and

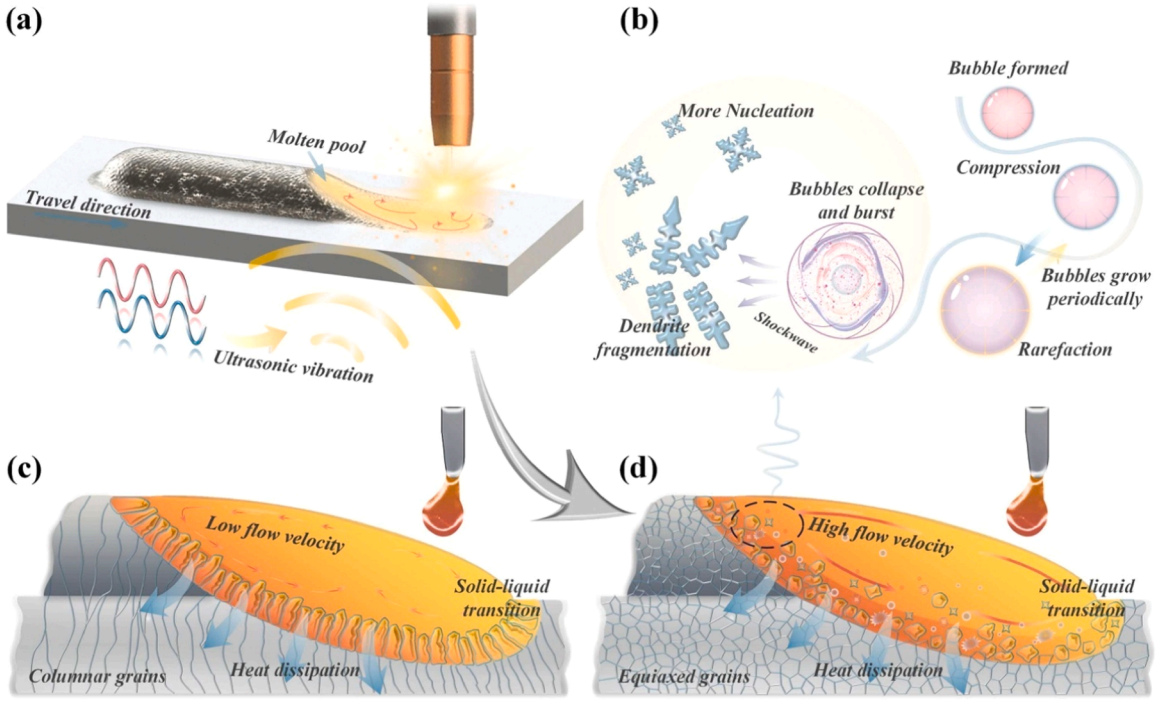


Fig. 19. Schematic illustrating the role of cavitation and acoustic effects induced by ultrasonic vibration in altering melt pool convection and subsequent grain refinement [140]. (*Reproduced with permission from Elsevier*).

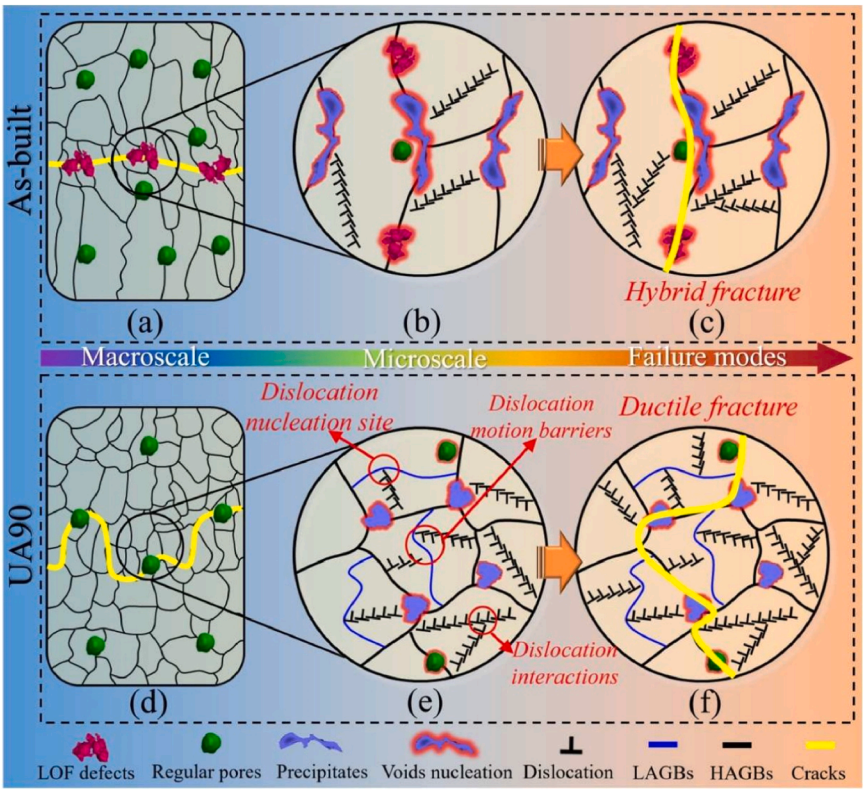


Fig. 20. Schematic illustrating microscopic mechanism of increase in strength ductility synergy for UV treated samples vis-à-vis as built sample [144]. (*Reproduced with permission from Elsevier*).

acoustic-streaming-assisted melt convection promote the columnar-to-equiaxed transition (CET), refine secondary phases, and improve microstructural homogeneity in Mg alloy deposits.

5.1.4. *Ex situ Surface engineering*

5.1.4.1. Laser shock peening. Laser shock peening (LSP) is a popular technique for inducing microstructural heterogeneities in a graded

fashion for enhancing mechanical properties and mitigation of surface tensile residual stresses. This ultrahigh strain rate enabled technique promotes surface nanocrystallization, generates nanoscale substructures and can also refine the size of harder precipitates in the alloy microstructure at micron scale depths from the surface. Li *et al.* [147] successfully imparted compressive residual stresses up to a depth of ~1 mm from the surface. This enhanced the YS and UTS of the CMT WDED fabricated AZ31 Mg alloy by ~30% and 13% respectively.

Fig. 21 depicts the sequential mechanism of nanocrystallization and secondary phase refinement leading to surface strengthening and marginal improvement in tensile properties. LSP induces a gradient microstructure characterized by the presence of nanograins up to a certain depth from the top surface layers exposed to LSP. With further increase in depth from the surface, deformation twins and their interaction with dislocations dominates the deformation microstructure. In the initial stage of LSP, the microstructure develops substantial interaction of planar dislocation arrays (PDA) due to significant generations of dislocations. In stage II, with progressive increase in strain, nano-mechanical twins operating in multiple parallel directions, fragment the coarser grain and also promote dislocation slip bands from the micron scaled precipitates. In stage III, with further increase in strain, a greater number of nano-mechanical twins are activated and trigger cracking of micron scale particles. Finally, further evolution of nano mechanical twins and subsequent exponential increase in dislocation interactions will generate sub grains, as twin boundaries are transformed into LAGB and HAGB. Therefore, various strengthening mechanisms synergistically contribute to improvement in YS. In the microstructural layers immediately beneath the surface, nanocrystallization and dispersion strengthening is achieved. With further increase in depth from surface, nano mechanical twins, micro mechanical twins are formed, and further below dislocation strengthening contributes to the increased strength [147].

5.1.4.2. Low Plasticity Burnishing (LPB). Although LSP is an effective strategy for inducing microstructural gradients and imparting compressive residual stresses on the surface, the peened surfaces have high roughness and are therefore unsuitable for high performance applications, where the component is exposed to corrosive media and fatigue loading. Therefore, low plasticity burnishing (LPB) technique that generates plastic deformation at the surface and subsurface by

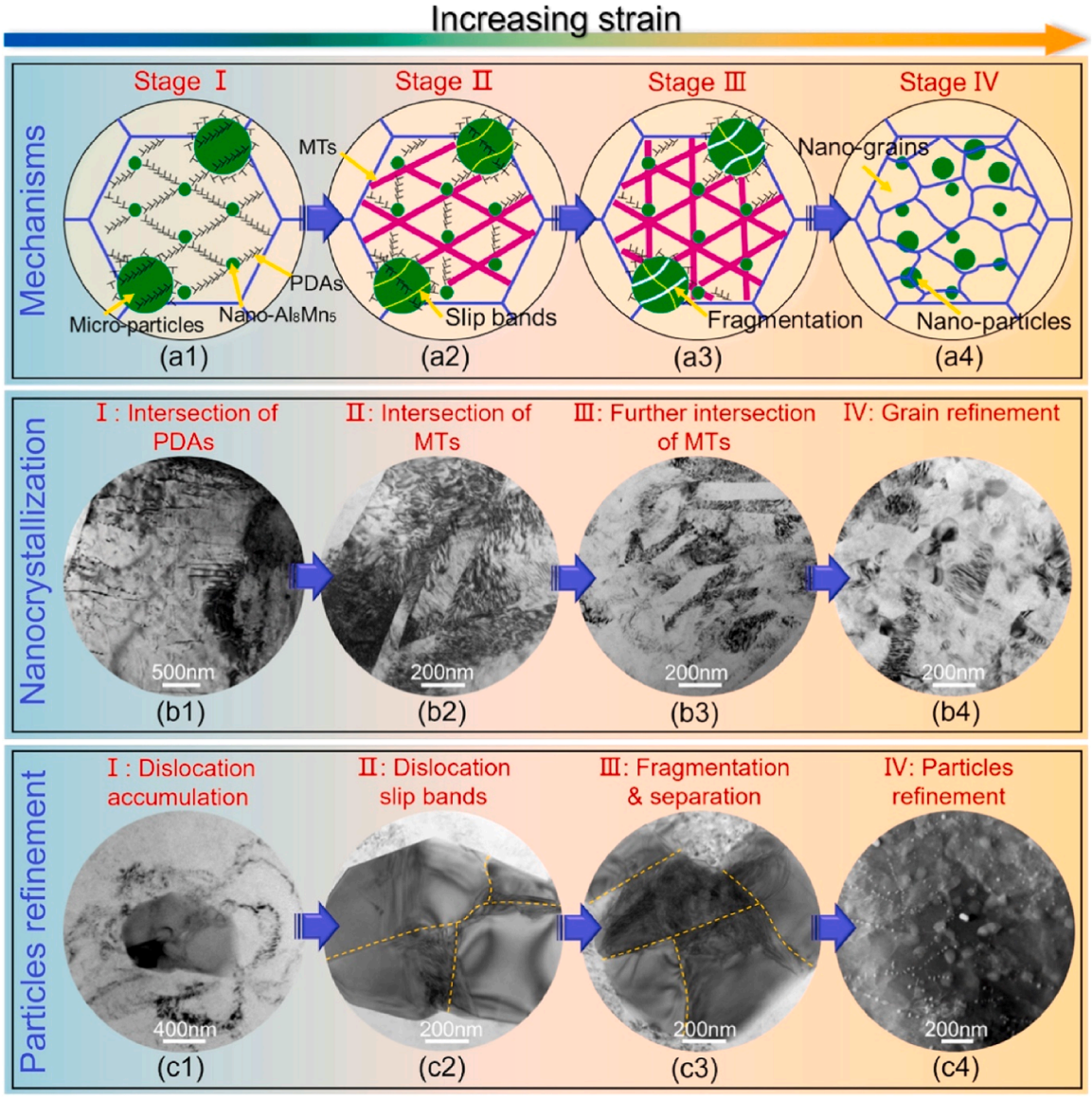


Fig. 21. Schematic depicting the four stage mechanism of nanocrystallization and precipitate reinforcement for ex situ LSPed CMT WDED AZ31 Mg alloy [147]. (*Reproduced with permission from Elsevier*).

application of a specific force (exceeding material's YS) through a ceramic roller is an attractive alternative [148]. Owing to the application of a ceramic roller on the surface, besides grain refinement and compressive residual stress, the surface is not significantly damaged. Fig. 22 depicts the schematic set up for ex situ LPB of a CMT WDED AZ31 Mg alloy and the surface finish obtained through two different burnishing strategies: a) cross LPB pattern b) parallel LPB patter.

Due to LPB treatment, there is an enhancement in the surface microhardness upto a depth of ~300 μm from the surface [148]. Among the two different burnishing strategies employed [148], cross pattern appears to improve the surface finish much more significantly and also superimposes higher compressive stresses at the surface and grain refinement to a greater depth from surface. The improvement in mechanical properties of the built component in cross pattern burnishing is ascribed to the formation of geometrically necessary dislocations (GND) at the surface, which lead to the formation of HAGBs and twin boundaries, although the same is not observed in parallel LPB. However, the caveat in this surface finish process is that an extensive process parameter optimization through a design of experiments approach is required. Specifically, the applied pressure on the ceramic ball, feed rate, medium of operation and number of passes and overlap distance [148] affect the quality of surface obtained.

5.1.5. Innovations in the tailoring of CMT allied process parameters

In Fig. 23 an illustration of the integration of in situ SiC particle addition along with CMT torch oscillation to introduce grain refinement in AZ31 alloy is displayed. From Fig. 23**a**, it is evident that columnar grain formation in CMT WDED is the consequence of large thermal gradient and negligible constitutional supercooling in front of the solid-liquid interface [149]. By performing CMT torch oscillation about a central axis (Fig. 23**b**), convective heat transfer of the melt pool is enhanced. Therefore, constitutional supercooling zone area is marginally increased and volume fraction of equiaxed grains can be improved. Fig. 23**c** depicts that incorporating nucleating agents like ceramic particles is far more effective compared to arc oscillation, for grain refinement and can even form composite microstructures [150–152]. SiC exhibits orientation relationship with α-Mg grains and serves as heterogeneous nucleating agents. Also SiC particles segregate to grain boundaries during solidification and arrests grain growth. The reason why the combination of CMT torch oscillation and SiC particle incorporation is the most effective of all the above cases is that it addresses both the aspects of increasing heterogeneous nuclei and decreasing thermal gradient. Fig. 24**g** also depicts that the nearest available particle for nucleation decreases for the above case compared to that in the CMT process. Therefore, through this technique, Yang et al. [149] demonstrate a remarkable decrease of ~81% in grain size, which leads to ~

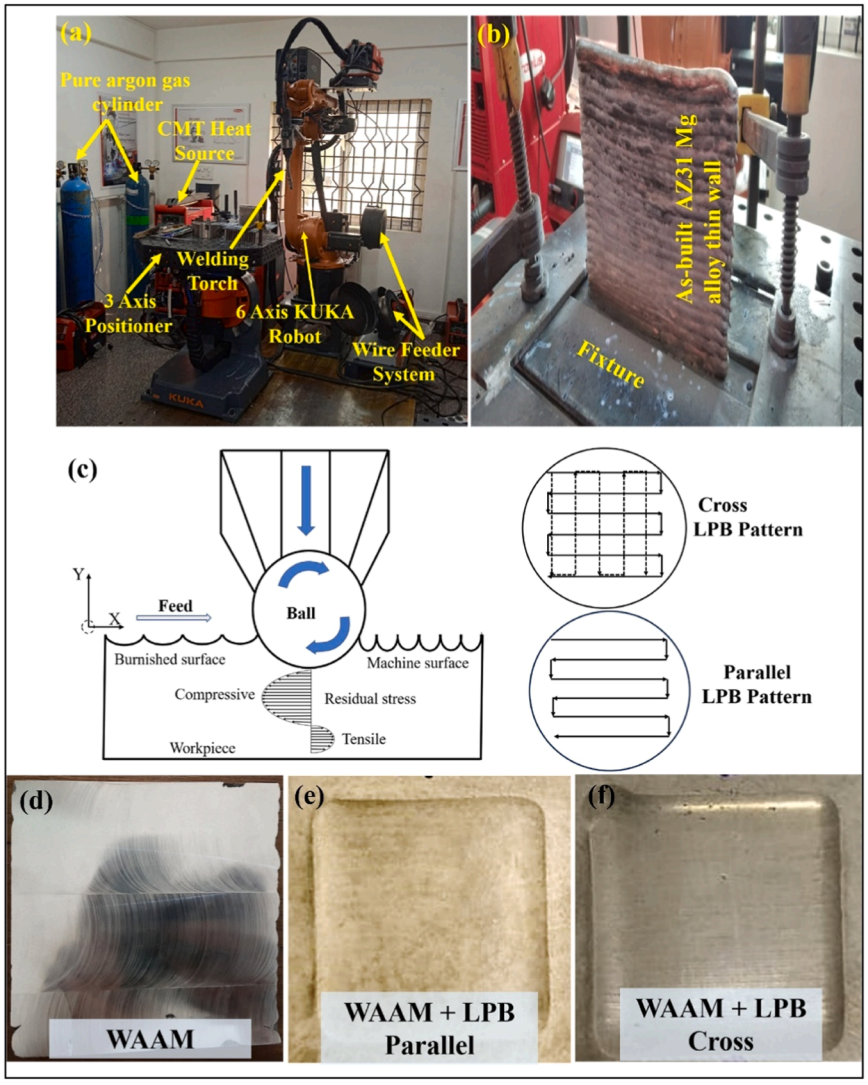


Fig. 22. Schematic depiction of ex situ LPB set up, burnishing strategies and the optical micrographs of AZ31 surfaces in various conditions [148]. (*Reproduced from Elsevier under CC BY 4.0*).

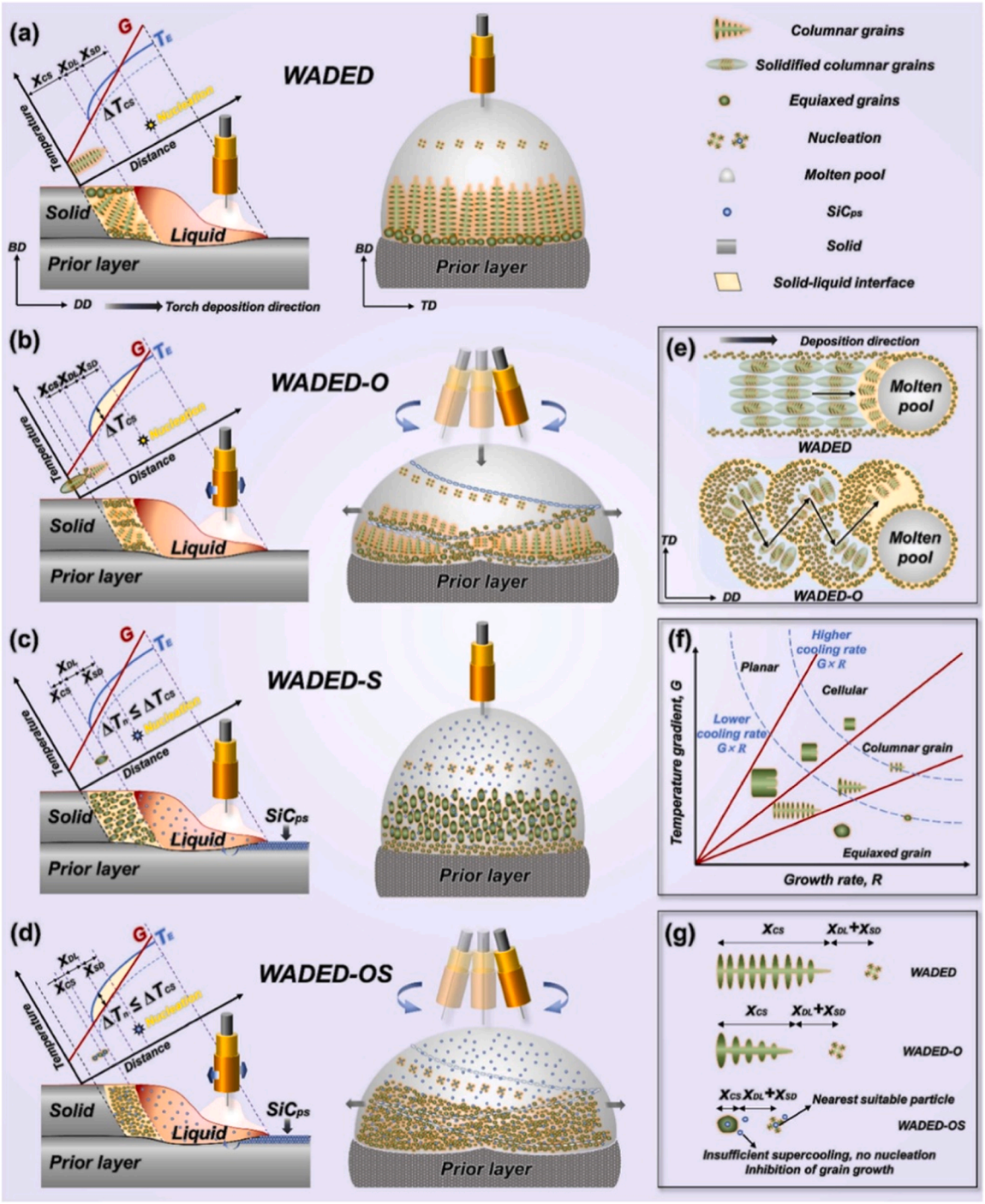


Fig. 23. Schematic depicting the effectiveness of combining CMT torch *in situ* incorporation of SiC particles for grain refinement for AZ31 alloy [149]. (*Reproduced with permission from Elsevier*).

23% and 38% increase in YS, 51.4% and 33% increase in UTS, and 100% and 163% in elongation in build and deposited directions, respectively for CMT WDED fabricated AZ31 Mg alloy. Similarly other investigations explored utilization of ultrasonic frequency pulsed arc [153], cryogenic cooling [154], water cooling [155] and water cooling coupled with ultrasonic vibration [156], optimized CMT torch path planning [157] as additional aids for refining the microstructure albeit with marginal improvement in mechanical properties.

5.2. Mg-RE based alloys: thermal management strategies through active cooling

Increasing the cooling rate in built wall through forced water circulation is a practically viable and a relatively cheaper technique for enhancing heat transfer and mitigating heat accumulation during CMT WDED process [158]. Fig. 24 illustrates a novel experimental setup where additional water channels are provided both underneath the substrate and forward/rear sides of the built wall for recirculating water to facilitate cooling. Evidently, adding such additional appendages for cooling does not affect the macroscopic formability as evident from

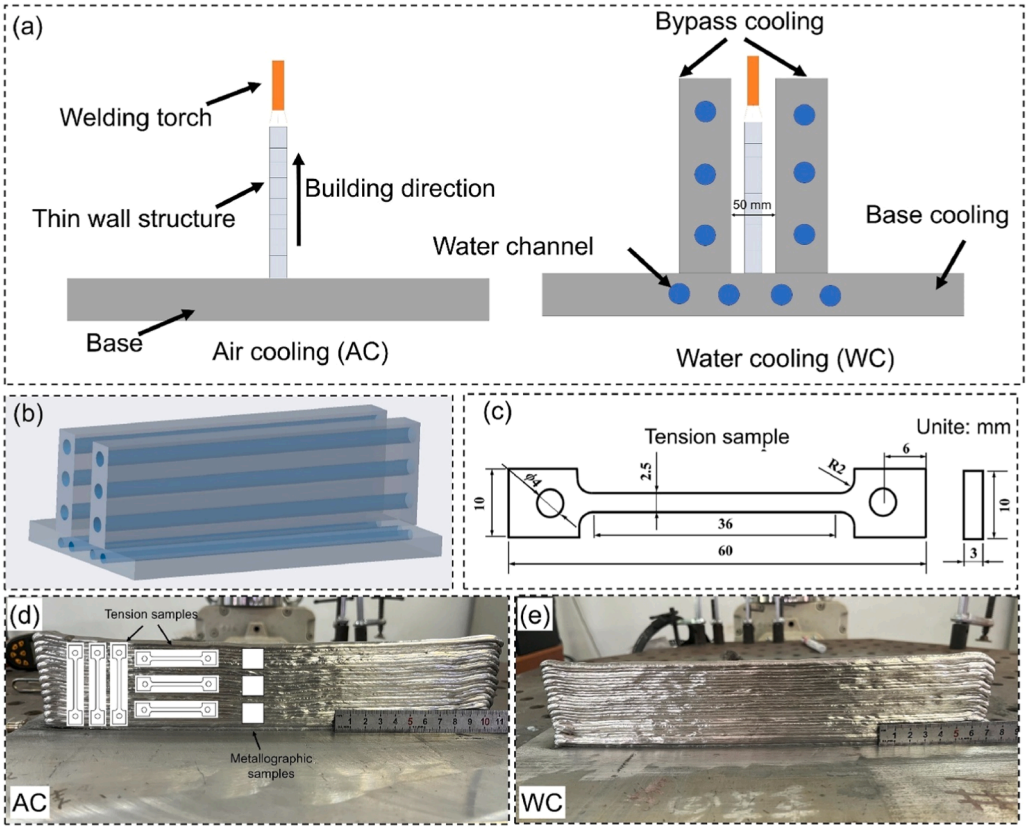


Fig. 24. Experimental set up of active cooling technique for minimizing heat accumulation during CMT WDED of Mg-Y-Nd-Gd-Zr alloy [158]. (*Reproduced with permission from Elsevier*).

macrographs of the built specimen (Fig. 24**e**). Due to increase in the cooling rate from the convective effects of recirculating water, a marginal decrease in grain size and substantial refinement of GB eutectic phase is reported [158]. Compared to the specimen that experienced only air-cooling, water-cooled specimens experience lower thermal gradients and also exhibits enhanced Zr solubility in the melt pool, which in turn enables its uniform precipitation in the α-Mg matrix after solidification. Owing to faster cooling rates, metastable β_1-Mg_3(Y,Nd, Gd) precipitate is prevented from coarsening, which results in a 11.7%, 5.8%, and 72.3% increment in UTS, YS and elongation, respectively compared to an air cooled CMT WDED manufactured Mg-Y-Nd-Gd-Zr alloy [158]. Based on the preceding discussions, Fig. 25 schematically summarises the coupled interactions among process parameters, melt pool behaviour, solidification mechanisms, microstructure evolution, final characteristics and defects governing Mg alloy CMT-WDED processing.

6. Post process heat treatments for optimized microstructure-mechanical properties

6.1. Mg-Al based alloys

CMT WDED fabricated AZ91 alloy exhibits unusually dissimilar precipitation kinetics during solution heat treatment (SHT) and aging compared to its as cast counterpart. In post SHT + aged condition, CMT WDED AZ91 comprised of continuous and discontinuous β-$Mg_{17}Al_{12}$ phase irrespective of various aging protocols performed [159]. SHT at 410°C for one hour followed by ageing at 250° C triggered discontinuous β-$Mg_{17}Al_{12}$ at GB within thirteen minutes of initiation of ageing protocol. The enhanced precipitation kinetics in CMT WDED alloy is due to equiaxed microstructure having large volume fraction of GB that provides multiple sites for discontinuous precipitate nucleation. Likewise unusual segregation of Al in in remelt zones during layer wise processing and nanoscopic scale Mn, Al rich precipitates also contributes to faster precipitation kinetics. Fig. 26 shows that ageing temperature is the predominant factor that drives precipitation kinetics. Low temperature ageing (250° C) leads to steeper increase in volume fraction of β-$Mg_{17}Al_{12}$ while maximum precipitate density was achieved within 4 h of ageing time. With increase in the precipitation of the β-phase, microhardness of the SHT + aged alloys increased at a rapid rate initially and later plateaued once maximum volume fraction of β-phase is precipitated. However, in this study, no further tensile tests are performed [159] to ascertain the role of SHT + ageing on bulk mechanical response.

6.2. Mg-RE based alloys

6.2.1. Mg-Gd-Y-Zn-Zr alloys

Designing heat treatment protocols in Mg-Gd-Y-Zn-Zr systems involves the following two underlying principles. First, as-built GB eutectic phase (Mg, Zn)$_3$(Gd, Y) must be completely disintegrated to release precipitate forming elements into matrix and also prevent crack formation during mechanical loading. Second, fine grain size attained during CMT WDED process should be preserved, which implies that the SHT + ageing process must not lead to grain coarsening. Hence, solutionizing (T4) and aging treatment (T6) explored in literature vary between 450 and 580°C and 200–225 °C respectively [127, 128, 130, 160, 161]. Specifically, the time duration for each of the respective protocol varies, and is generally much shorter compared to that of conventionally processed materials, owing to the non-equilibrium nature of the solidification in CMT WDED manufactured alloys. If substantially longer duration is chosen for SHT at ~520° C, it promotes the precipitation of a high volume fraction of the χ phase. However, while SHT at ~580° C leads to a homogenized microstructure, it causes grain

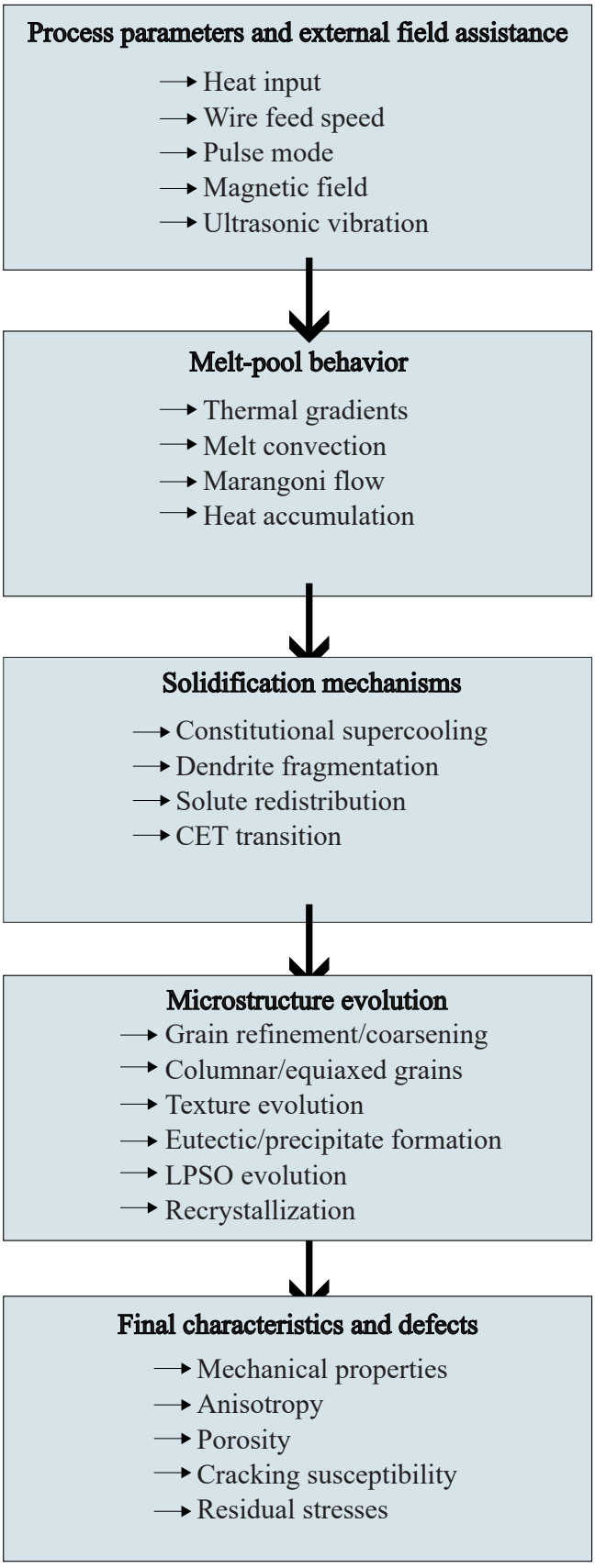


Fig. 25. Integrated schematic framework summarising the coupled interactions among process parameters, transient melt-pool behaviour, solidification mechanisms, microstructure evolution, and final microstructural characteristics/defects governing Mg alloy CMT-WDED processing.

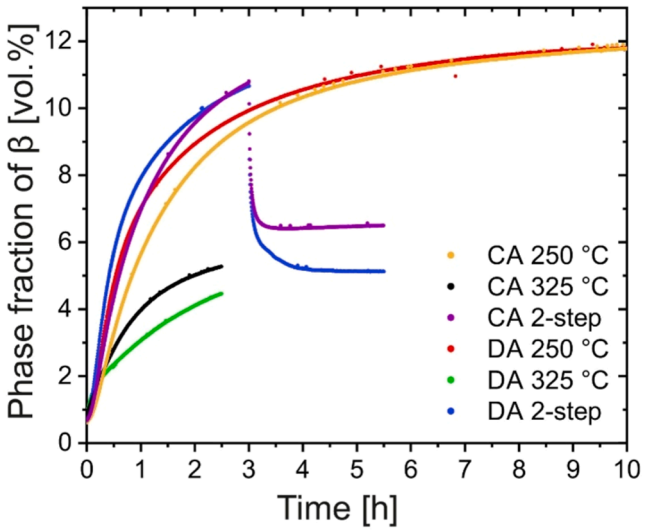


Fig. 26. Temporal evolution of β-$Mg_{17}Al_{12}$ phase with respect to conventional and direct aging protocols for AZ91 Mg alloy [159]. (*Reproduced from Elsevier under CC-BY-NC-ND 4.0*).

coarsening. Likewise, if a lower temperature of ~480°C is chosen for SHT, complete dissolution of the eutectic phase is prevented.

In general, T4 treatment, leads to elimination of both eutectic phase and RE rich segregations, and further results in the precipitation of 14H-LPSO phases. Nonetheless, T4 treatment could not eliminate higher melting point cuboid phases like (Gd, Y)H_2 and Zr rich segregations. T6 treatment does not coarsen the 14H-LPSO phases but results in precipitation of fine nanoscale -β' and β" precipitates [160]. Fig. 27 schematically illustrates the precipitation pathway for Mg−8.1Gd−2.6Y−0.7Zn−0.5Zr alloy under SHT + ageing and ageing conditions. Evidently, the alternating coarse- and fine-grained structure is preserved throughout the heat treatment process irrespective of the heat treatment route. While ageing treatment alone not only eliminates the 14H-LPSO phase formation but also preserve the sanctity of the eutectic (Mg, Zn)$_3$(Gd, Y) GB phase and forms nano- β' phases inside grains. Conversely, SHT + ageing first leads to uniform precipitation of 14H-LPSO phase at GB and subsequently forms nano- β' within grain interiors. Here the advantage is that GB eutectic phase is completely eliminated.

For Mg−9.88Gd−3.44Y−1.56Zn−0.4Zr [128] SHT at 500° C for 1 h, does not dissolve the GB eutectic phase completely. As a result, the subsequently aged microstructure comprises of remnant GB eutectic phase. Conversely, when SHT duration is increased for 12 h at 500° C, GB eutectic phase dissolves completely. Here in this study, prolonged ageing for 72 h compared to 48 h in [160] did not lead to grain coarsening due to the pinning effect of cubic (Gd, Y)H_2 phase. Likewise, Zhang et al. [127] reported identical microstructural attributes and tensile properties when Mg−9.4Gd−3.3Y−1.75Zn−0.38Zr alloy was aged at 225°C for 12 h subsequent to SHT at 500°C for 12 h.

Despite commonalities in the obtained microstructure in terms of phase formation post SHT + ageing, it is not clear whether the deformation response obtained is highly sensitive to alloy chemistry. While Mg−9Gd−4Y−1Zn−0.4Zr exhibits isotropic mechanical properties [130] with highest elongation 8%, YS 220 MPa and UTS 370 MPa, Mg−10Gd−2Y−1Zn−0.5Zr has the lowest elongation 2.7%, YS 278 MPa and UTS 403 MPa on being subjected to the same SHT + ageing treatment [161]. It is observed that Zn plays a vital role in elemental partitioning into the eutectic phase during deposition. This elemental partitioning in the as built state plays a key role in subsequent formation of multiple nano scale precipitates like γ", γ', 14H-LPSO, β', β_1, RE rich cuboid phases and Zr segregations in SHT + aged condition [161]. Multiple strengthening mechanisms responsible for such high

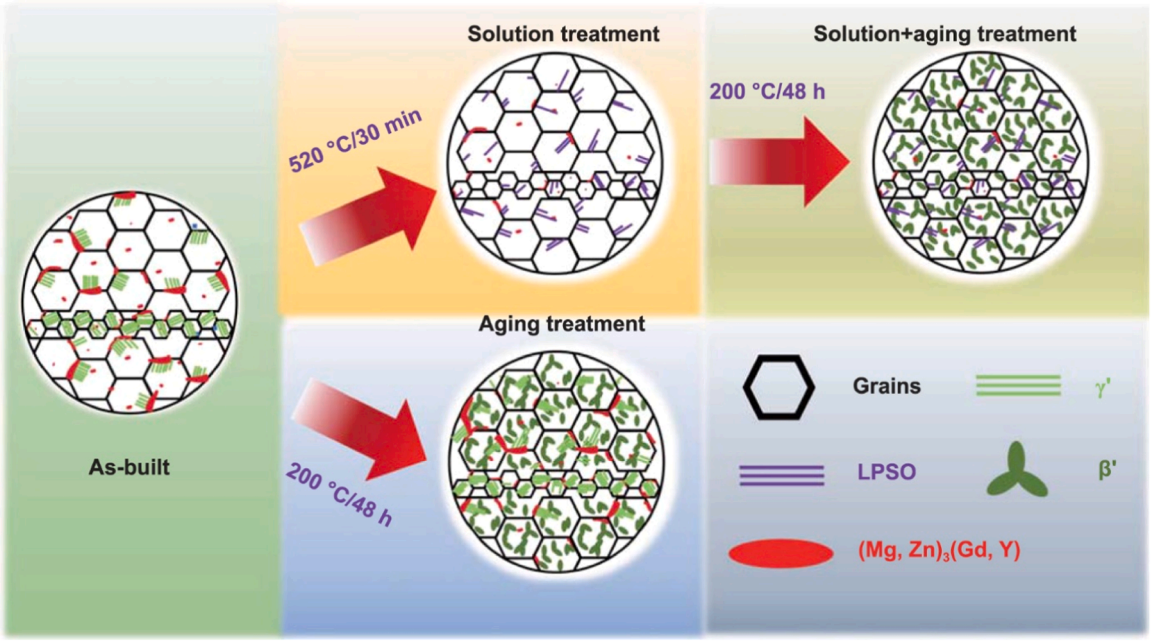


Fig. 27. Schematic illustrating the microstructural evolution of Mg−8.1Gd−2.6Y−0.7Zn−0.5Zr alloy with respect to nature of post built treatment [160]. (*Reproduced from IOP Publishing Ltd. under CCBY−4.0*).

strength in SHT + aged condition are intrinsic lattice friction stress, strengthening at GB, solid solution strengthening, LPSO phase induced strengthening and remarkably higher contribution of nano-β' precipitates [160]. However, existing studies hint that SHT + ageing creates strength-ductility dilemma in this alloy system owing to complex precipitation behavior.

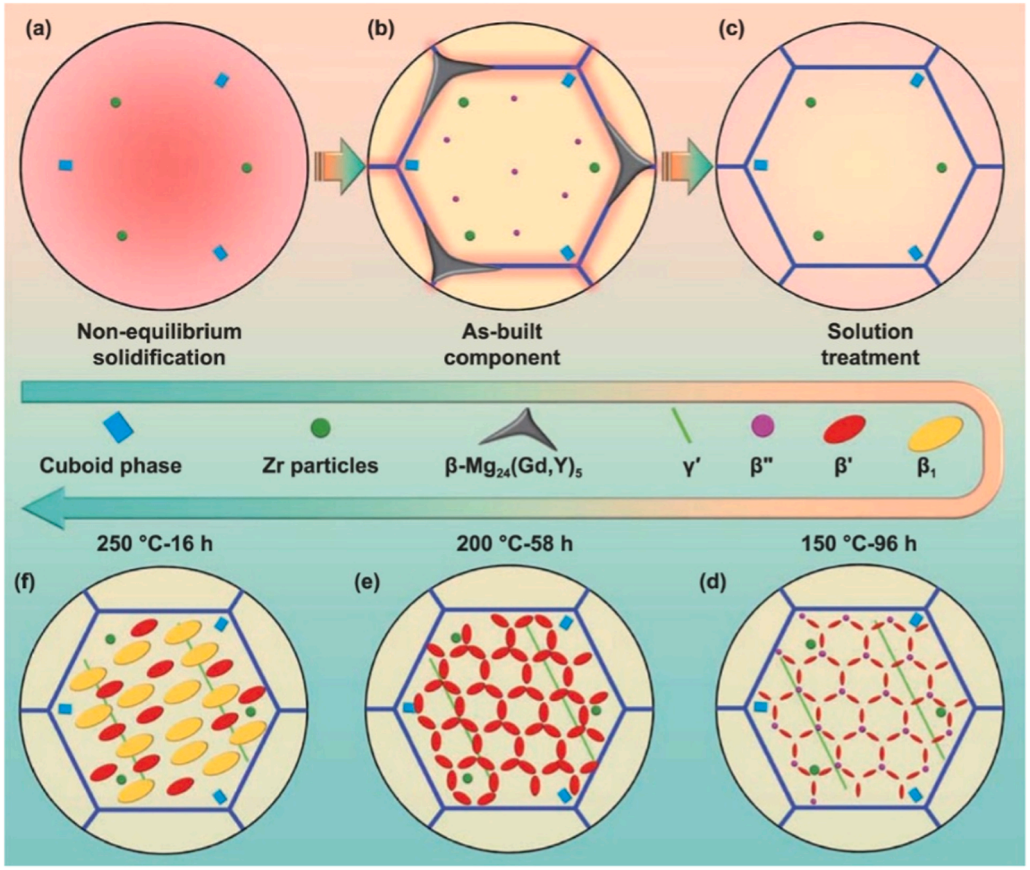


Fig. 28. Precipitation mechanism for Mg-Gd-Y-Zr from various aging treatments [162]. (*Reproduced from IOP Publishing Ltd. under CC BY−4.0*).

6.2.2. Mg-Gd-Y-Zr alloys

Fig. 28 depicts the mechanism of precipitate evolution in Mg-Gd-Y-Zr alloys. Here, contrary to Zn doped system mentioned earlier, the absence of Zn will lead to formation of β- $Mg_{24}(Gd,Y)_5$ as the GB eutectic phase [162–164]. As-built microstructure is also consists of cuboid $(Gd,Y)H_2$ phase, Zr particles and β" nano phases. SHT at 530° C for 1 h effectively dissolves the as built microstructure except the high temperature phases like Zr particles and RE based cuboid structures that get retained (also throughout the ageing treatment), due to the temperature not being high enough to facilitate their dissolution. Subsequent microstructure evolution and mechanical properties post ageing is dependent on the magnitude of temperature and time duration. Perhaps the high Gd content in the Mg-Gd-Y-Zr alloys considered by Li *et al.* [162] necessitates higher SHT (530 °C) compared to that by Ma *et al.* and Shen *et al.* [163,164] (400 and 480°C respectively) to ensure complete dissolution of GB eutectic phase albeit their YS, UTS and elongation are similar. Regardless, these alloys exhibit grain growth with increase in SHT temperature.

Irrespective of ageing time and temperature, long slender nano γ' precipitates can be found. At low temperature and long ageing time (150°C and 96 h) the microstructure is dominated by a well-connected hexagonal network of β' lath like nanoprecipitates that mutually share a β" spherical precipitate with in grain interior. With increase in ageing temperature and reduction in time duration, the hexagonal network is partially disrupted and also absence of β" spherical precipitates can be observed. If ageing is done at higher temperature i.e. 250° C for 16 h, the hexagonal network is completely broken, coarser β_1 phase and β' dominate the microstructure. Despite wide variation in SHT temperatures and ageing durations nearly identical mechanical properties were reported [162–164]. Specifically, ageing protocol driven, nano-β' precipitates are responsible for remarkable strength and lower ductility as they impede dislocation motion, while nano β_1 exhibited easier propensity to shear and proliferation of slip bands and thereby promoted ductility [162].

6.2.3. Mg -Y-Nd-Gd-Zr alloys

For WE43 alloy, SHT temperature is to be carefully optimized for attaining optimal combination of strength and ductility in post aged state. While lower SHT causes incomplete dissolution of GB eutectic phase, high temperature SHT causes abnormal grain coarsening. In post aged condition, suboptimal SHT lead to significant fraction of GB eutectic phase while highest temperature SHT nullifies the beneficial aspect of strengthening effect arising from high density nano-β" precipitates due to grain coarsening [165]. Hence both these cases are not ideal from a mechanical property enhancement perspective. Fig. 29 depicts that the microstructure in optimal SHT + aged condition is dominated by small volume fraction of GB eutectic $Mg_{41}Nd_5$ and nano cuboid $Mg_{24}Y_5$ phase along with uniform precipitation of nano-β" precipitates throughout the microstructure. Therefore, intermediate temperature SHT followed by ageing at 225°C for 18 h lead to best combination of UTS, YS and elongation respectively (323 ± 15.2 Mpa, 225 ± 11.3 Mpa, and 8.4 ± 1.1%). However, when innovative *in situ* water cooling was adopted during CMT WDED followed by SHT at 500°C for 1 h and double step (high and low temperature) ageing lead to remarkable increase in UTS and YS along with a marginal decrease in elongation, respectively (393 ± 5 MPa, 265 ± 5 MPa and 5 ± 0.5%). *In situ* water cooling leads to a sharp decrease in thermal gradients, enhanced cooling rate and forms fine nano-β' ($Mg_{12}YNd$) precipitates that contribute to the observed high strength. Similar SHT + ageing in the temperature regimes stated above on other Mg alloy systems also reveal dissolution of GB eutectic structure and precipitation of fine scale nano-precipitates, which lead to enhancement in tensile strength [166]. Also, other practical innovative approaches involve the extension of the inter-layer dwell time to decrease thermal input accumulation and improvement in cooling rate to tailor microstructural attributes [167]. Table 1 summarises the different solution and ageing heat treatments applied to the different CMT-manufactured Mg alloys, and their effect on microstructure and mechanical response.

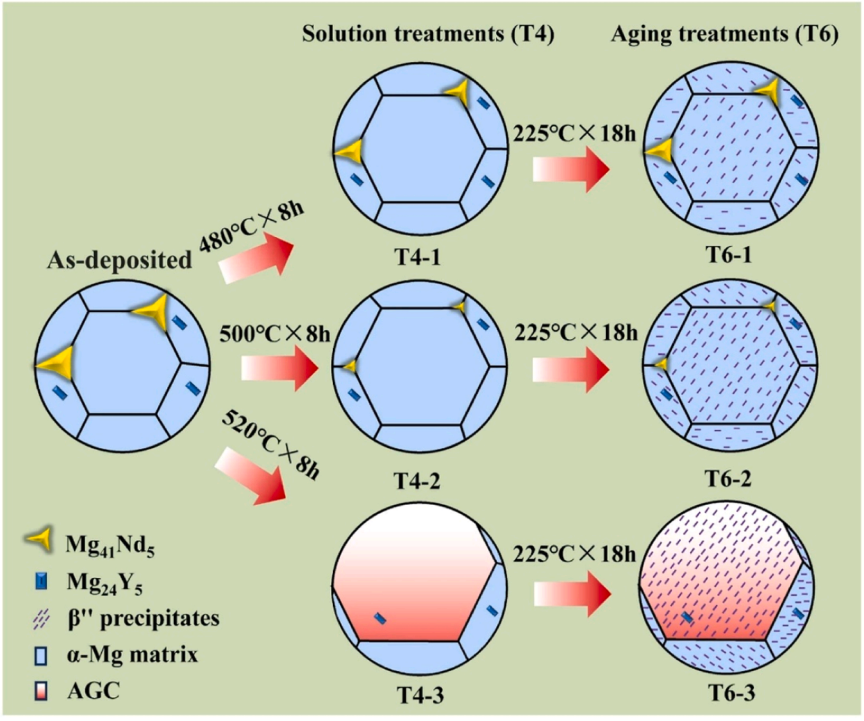


Fig. 29. Schematic illustration of microstructural evolution on SHT and AG for Mg−4.08Y−2.07Nd−1.06Gd−0.51Zr alloy [165]. (*Reproduced with permission from Elsevier*).

Table 1
Comparative summary of solution heat treatment and aging parameters, corresponding microstructural evolution, and mechanical property improvements in CMT additively manufactured magnesium alloy systems.

Mg alloy system	Solution treatment (temperature, time) (°C, hours)	Aging treatment (temperature, time) (°C, hours)	Main microstructural effect	Mechanical Property response
AZ91[159]	410°C, 1 h	250° C, 4 h	Maximum precipitate density of β-phase	Improved microhardness
Mg-Gd-Y-Zn-Zr [127, 128, 130, 160, 161]	450–580°C, varies	200–225°C, varies	Multiple nanoscale precipitates	Depends upon alloy chemistry
Mg-Gd-Y-Zr [162–164]	400–530°C, varies	150–250°C, varies (96–16 h)	nano-β' and nano β_1 precipitates	Strength and ductility depends upon precipitates
Mg -Y-Nd-Gd-Zr [165]	480–520°C, 8 h	225°C, 18 h	Uniform nano-β'' precipitates	Best combination at 500°C solution treatment
Mg -Y-Nd-Gd-Zr (in situ water cooling) [166]	500°C, 1 h	Double-step high and low temperature ageing	Forms fine nano-β' ($Mg_{12}YNd$) precipitates	Remarkable increase in strength

7. Deformation behaviour

7.1. Tensile testing

7.1.1. Mg-Al based alloys

CMT WDED fabricated Mg-Al alloys have inferior tensile properties in the as-built condition and currently there is only one report that addresses heat treatment aspects for attaining isotropic tensile properties for Mg−8.2Al−0.6Y−0.4Ce (AE81) alloy [168]. However, various *in situ* techniques like hammer peening, IFSP, UV and *ex situ* techniques like LSP and LPB integrated with CMT WDED are widely explored to enhance mechanical properties. As per existing literature, CMT WDED + IFSP processing leads to remarkably high strength-ductility synergy amongst all other process supplementations to CMT WDED processing. The representative stress-strain curves of AZ91 alloy processed via this method are shown in Fig. 30. It is noteworthy that YS and UTS obtained parallel to build direction are higher compared to that of CMT deposition direction [139]. In case of *in situ* IFSP, the mechanism of fracture during tensile deformation changes from intergranular fracture in as built state to transgranular fracture. The obtained good strength-ductility combination in this case is attributed to refinement of grains and secondary phase from the intense deformation and generation of GNDs at hard/soft grain interfaces in the graded microstructure [139].

7.1.2. Mg-RE based alloys

In Mg-RE based alloys, various studies explored only heat treatment route through various SHT + AG protocols, while there are no studies that integrated the above mentioned *in situ* or *ex situ* techniques for enhancing mechanical properties. Fig. 31 depicts the classical strength-ductility dilemma for heavy RE alloyed Mg−10Gd−2Y−0.5Zr (GW102K) and Mg−10Gd−2Y−1Zn−0.5Zr (GWZ1021K) after being subjected to T4 and T6 treatments. It is evident that while T4 has almost no impact on YS and UTS in both transverse (TD) and build directions (BD) for both these alloys, while T6 caused the opposite effect in which, both YS and UTS increased at the expense of ductility. Specifically, the increment in strength and concomitant decrease in ductility is more pronounced for Zn doped GWZ1021K alloy [161].

From Fig. 31**b and d** it is further evident that GWZ1021K maintained consistently higher YS and UTS and lower elongation compared to that of GW102K alloy in as-built, T4 and T6 conditions. Despite almost similar alloy chemistry, it is remarkable that doping Zn leads to drastic change in microstructure in as-built, T4 and T6 states. The prominent microstructural changes triggered through Zn doping in GWZ1021K vis-à-vis undoped GWZ102K alloy are as follows. One, in the as built state the GB eutectic phase changes from $Mg_{24}(Gd, Y)_5$ to $(Mg,Zn)_3(Gd,Y)$, which accompanies the formation of nano-γ'' and γ' phases and significantly minimizes the volume fraction of nano-β'' phases [161]. Two, in T4 condition, profuse formation of 14H-LPSO structures along with inheritance of nano-γ'' and γ' phases from the as-built state and three, in T6 condition, the formation of an extensive network of nano-β' phases that share spherical β_1 precipitates along with the inheritance of 14H-LPSO, nano-γ'' and γ' from the T4 state. During plastic deformation of the T6 sample, the CMT WDED fabricated GWZ1021K alloy, which

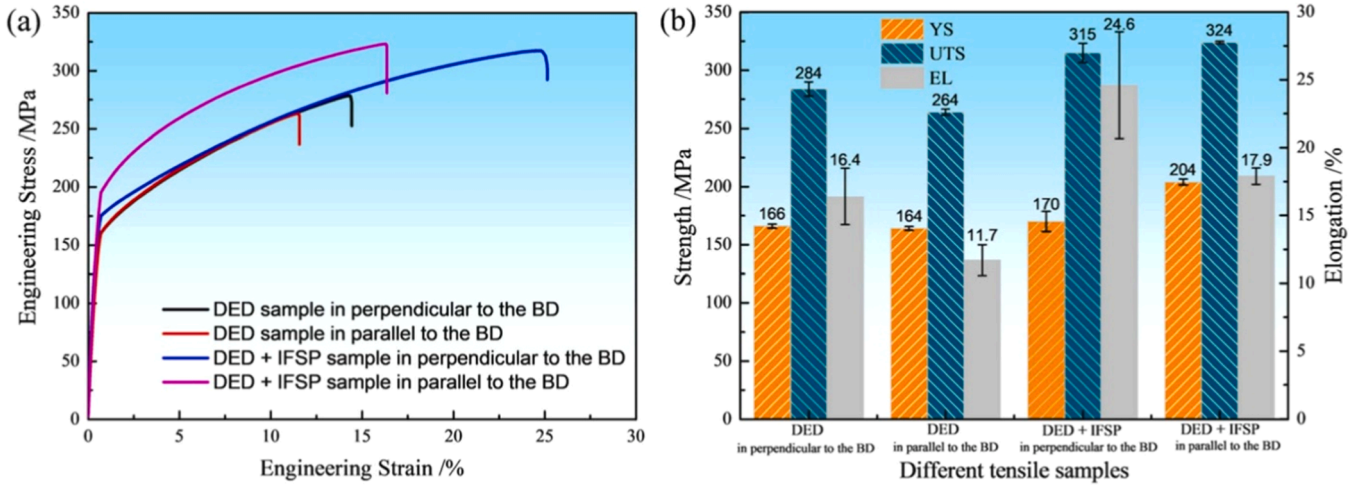


Fig. 30. Tensile properties of CMT WDED fabricated AZ91 Mg alloy subjected to IFSP in parallel and perpendicular to build directions[139]. (*Reproduced with permission from Elsevier*).

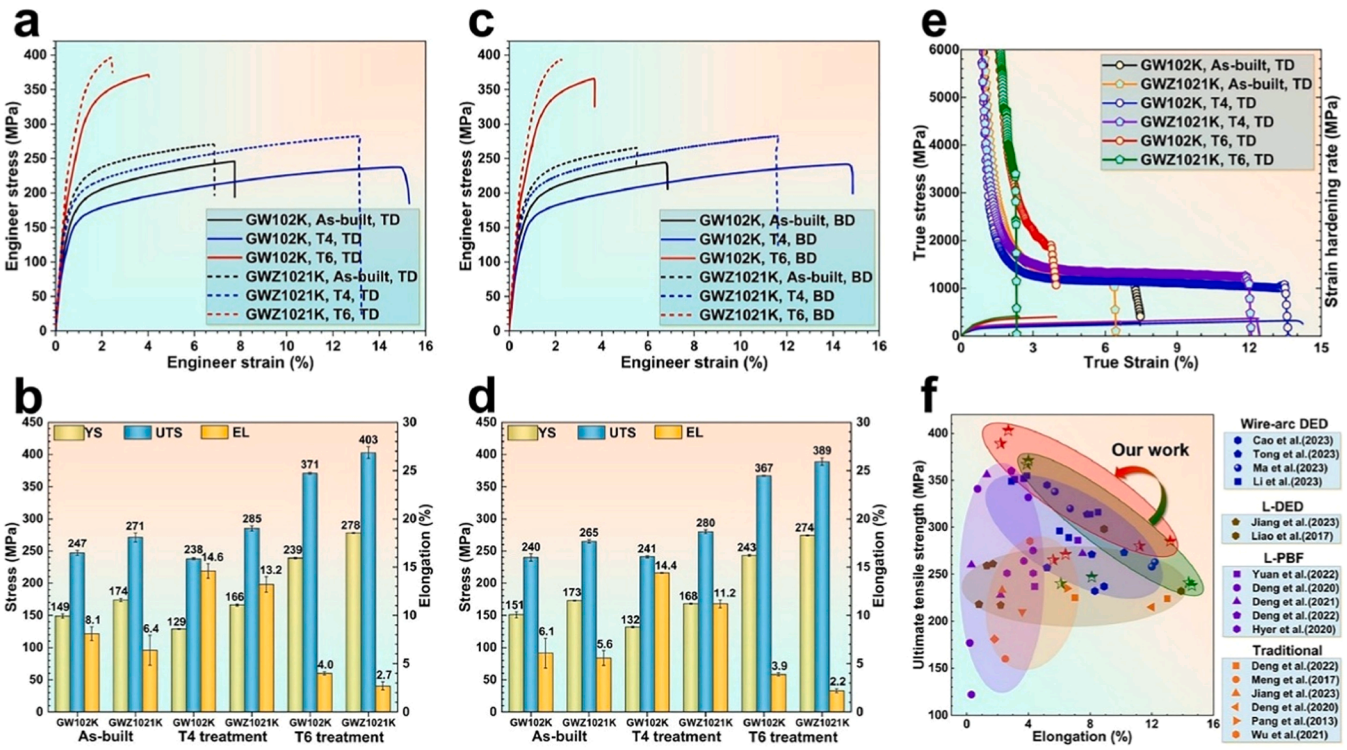


Fig. 31. Comparison of stress-strain curves for CMT WDED Mg−10Gd−2Y−0.5Zr (GW102K) and Mg−10Gd−2Y−1Zn−0.5Zr (GWZ1021K) alloys in as-built, T4 and T6 treated states along (**a**), (**c**) deposition direction (TD) and (**b**), (**d**) in build direction BD (**e**) strain hardening rate comparison along TD (**f**) comparison of tensile results with literature [161]. (*Reproduced from Elsevier under CC BY-NC-ND 4.0*).

has extensive network of nano-β'phase and 14H-LPSO nanostructures effectively blocks both basal and non-basal dislocation motion, which contributes to this enhanced strength [161].

Fig. 32 illustrates that the fracture mode in both GWZ102K and GWZ1021K exhibits microstructural state dependence although the latter undergoes brittle mode of failure. In the as-built state, the ductility is ascribed to formation of persistent slip bands whereas certain pockets of cracks that form are attributed to fracture of GB eutectic phases [161]. Here, the failure is driven by stress concentration around GB eutectic phases and nanoprecipitates in grain interiors. In T4 state, the predominant fracture mode is ductile fracture associated with increase in percentage of elongation due to the formation of high density slip bands. It is noteworthy that the volume fraction of dimples in GWZ102K is larger. In T6 state, the volume fraction of cleavage planes in GWZ1021K is larger and its pronounced brittleness is ascribed to high stress concentration caused by massive dislocation pileup at secondary phases. Here failure is driven by high volume fraction dislocation substructures. Additionally, the propensity for cracking is also higher for Zn doped alloy.

However, in the study by Li *et al.*, [161] it is not clear whether there is a gradient in nanoprecipitation throughout the build wall unlike that in the study by Deng *et al.* on GWZ102K [130] where uniform volume fraction of second phases (8%) is reported. Also, the GWZ102K alloy considered by Deng *et al.*, [130] despite being heavily with RE, does not have diverse nanoprecipitates like that in the one tested by Li *et al.*, [161]. Perhaps concentration differences of Gd and Y in the alloys considered by the two studies [130, 161] could have altered the phase formation sequence leading to precipitation of a lower fraction of precipitates in the alloy considered by Deng *et al.*, [130]. This results in higher percentage elongation (8%) albeit at the expense of lower YS and UTS (220 and 370 MPa respectively). Since isotropic tensile properties are observed in the GWZ102K alloy developed by Deng *et al.*, [130] as opposed to anisotropy in the one considered by Li *et al.*, [161], it appears that careful optimization of both alloy chemistry with regard to RE elements and heat treatment procedures [160] is necessary for attaining a synergy between strength and ductility. Specifically, nano-β' precipitates dictate the mechanical response, as these phases contribute to strengthening in the T6 condition [160]. Hence Mg-RE alloy chemistries that promote higher volume fraction of LPSO phases in T4 state are detrimental for mechanical properties because they consume a larger fraction of RE elements and hinder the precipitation of nano-β' phases [160]. Meanwhile, even for specific Mg alloy chemistries, temperature and time duration variations in AG protocols could lead to drastic changes in strength and ductility in the T6 state [127, 162, 164,165] highlighting the challenges in designing both alloys and employing SHT + ageing practices for mechanical performance.

7.2. Hot compression testing

CMT WDED being a unique AM process that has the ability to integrate diverse supplementary deformation techniques, hot compression studies are ideal to probe the suitability of techniques like rolling and forging on improving the microstructural attributes of Mg alloys either *in situ* or post-fabrication. Since as built microstructures are nonequilibrium in nature, the processing maps and allied unstable regimes explored for conventionally processed alloys, may not be directly applicable in this context. Therefore, few studies started to emerge in this direction specifically for Mg-RE based alloys [169–171]. These investigations reveal that both high deformation temperatures and low strain rates will lead to decrease in peak flow stress. It is noteworthy that under identical deformation conditions, peak flow stress of CMT WDED Mg-Gd-Y-Zn alloy is significantly smaller as compared to its cast + homogenized counterpart [169]. This is rationalized by the observation of a fine equiaxed grain structure in the as-build condition that amplifies dislocation density as opposed that in the conventionally processed alloy. High volume fraction of GB, twins, dislocation loops and stacking faults generated during hot compression provide numerous active sites for dynamic recrystallization, leading to softening and

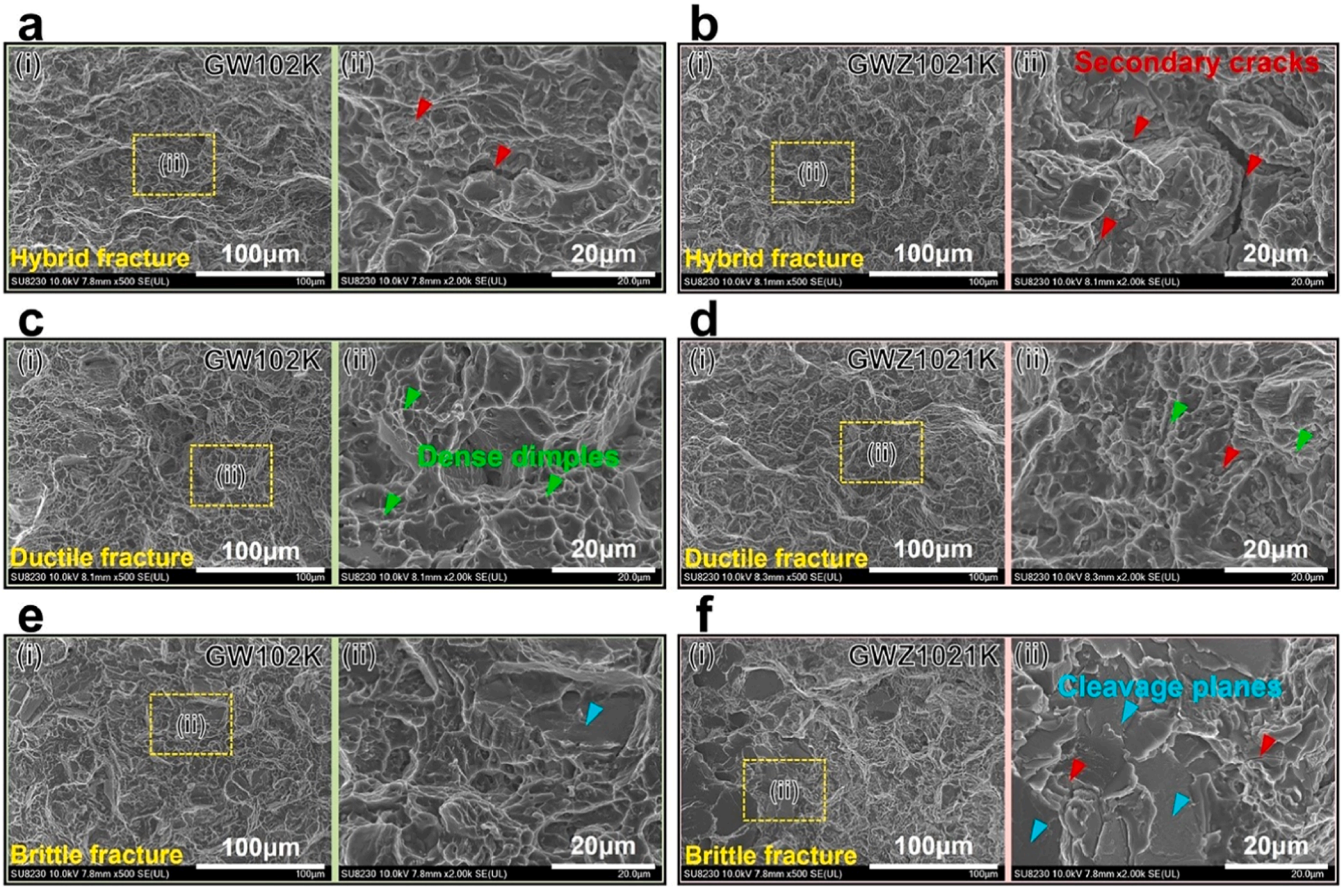


Fig. 32. Comparative fractographs of TD tensile samples in as-built, T4 and T6 conditions for: (**a**),(**c**),(**e**) GWZ102K and (**b**),(**d**),(**f**) GWZ1021K [161]. (*Reproduced from Elsevier under CC BY-NC-ND 4.0*).

decrease the flow stress of the material being deformed. These factors lead to grain refinement.

8. Concluding remarks

This review summarizes the current state-of-the-art in cold metal transfer (CMT) wire directed energy deposition (WDED) of Mg alloys, with emphasis on process physics, thermal behavior, microstructure evolution, and structure–property correlations. The reviewed literature demonstrates that the relatively low heat input associated with the CMT process offers significant advantages over conventional arc-based additive manufacturing techniques by minimizing spatter formation, oxidation, distortion, and excessive heat accumulation during deposition. Furthermore, the development of advanced CMT variants such as CMT-pulse and CMT-advanced modes, along with external-field-assisted strategies, has enabled improved control over droplet transfer stability, melt-pool oscillation, and dimensional stability during fabrication.

From the solidification perspective, the transient thermal behavior during multilayer deposition governs melt-pool convection, thermal gradients, cooling rates, constitutional supercooling, and dendrite evolution. The coupled interaction among these factors determines grain morphology, precipitate evolution, texture development, and defect formation in Mg alloy deposits. External field assistance through ultrasonic vibration, electromagnetic stirring, pulse current modulation, and mechanical oscillation has emerged as an effective route for promoting dendrite fragmentation, heterogeneous nucleation, grain refinement, and microstructural homogenization.

The review also establishes that Mg-Al-, Mg-RE-, Mg-Y-Nd-Zr-, Mg-Nd-Zn-Zr-, and Mg-Li-based alloy systems exhibit strong cooling-rate-dependent microstructural evolution during CMT WDED. The formation of eutectic structures, LPSO phases, precipitate distributions, recrystallized grains, and texture heterogeneity is strongly influenced by heat accumulation and repeated thermal cycling during layer-wise deposition. In general, refinement of equiaxed grains and homogeneous precipitate distributions improve hardness, strength, ductility, and crack resistance, whereas porosity, liquation cracking, solidification cracking, oxidation, residual stresses, and anisotropy remain major metallurgical challenges limiting broader industrial implementation. Post-processing treatments such as solution heat treatment and aging have demonstrated considerable potential for tailoring precipitate evolution and enhancing mechanical performance.

However, the following aspects deserve further attention for continued advancement in this field:

1. There are very limited investigations on post-process heat treatment strategies for CMT WDED fabricated Mg-Al-based alloys. Likewise, studies involving supplementary in situ/ex situ processing techniques for improving the structure–property correlations of Mg-RE-based alloys remain scarce.
2. Apart from friction stir processing (FSP), ultrasonic vibration (UV), laser shock peening (LSP), laser pulse assistance, hammer peening, and thermal management strategies, additional deformation-assisted approaches such as rolling and forging could provide promising pathways for enhancing grain refinement and reducing microstructural heterogeneity in CMT WDED fabricated Mg alloys. Furthermore, hybridization of multiple external-field-assisted techniques may provide synergistic improvements in microstructural stability and mechanical performance.
3. Most of the currently available studies on CMT WDED fabricated Mg alloys are restricted to uniaxial tensile characterization. Important

aspects such as fracture toughness, fatigue resistance, creep behavior, impact toughness, and damage tolerance remain largely unexplored. Moreover, expanding thermomechanical deformation studies such as hot compression to broader Mg alloy systems will help establish stable processing windows suitable for integration with CMT WDED.

4. Shape control and dimensional stability remain critical challenges in Mg alloy CMT additive manufacturing owing to the low melting point, oxidation tendency, and heat accumulation behavior of Mg alloys. Future studies should therefore focus on systematic optimization of process parameters, thermal management strategies, melt-pool control, and path planning approaches for achieving geometrically stable and defect-free deposition.
5. WDED is a highly flexible additive manufacturing process because it utilizes wire feedstock materials. Consequently, complex geometries and near-net-shape fabrication can be achieved efficiently. While AZ31 and AZ91 alloys have been investigated extensively, other alloy systems such as Mg-Zn-based rare-earth-free alloys, Mg-Al-Ca, Mg-Sn-Ca, and Mg-Li alloys also exhibit strong potential for thin-wire fabrication due to their favorable extrudability and processability, thereby considerably expanding the future scope of Mg alloy CMT WDED technology.

CRediT authorship contribution statement

Stanislav Evalshin: Writing – review & editing. **Jung-Ting Tsai:** Resources. **A.H.V. Pavan:** Validation. **Narayan Ramasubramanian Lakshmi:** Writing – review & editing, Supervision, Resources, Project administration, Conceptualization. **Mehul Mendiratta:** Validation, Writing – review & editing. **K.S.N.Satish Idury:** Writing – original draft, Formal analysis, Data curation. **Kai Chen:** Writing – review & editing.

Declaration of Competing Interest

The authors declare that they have no known competing financial interests or personal relationships that could have appeared to influence the work reported in this paper.

Acknowledgements

SI dedicates his contribution in this work to his late father Idury Parthasarathi who has been instrumental in shaping his career. This research was supported by NSTC 114-2923-E-011-005-MY3.

References

[1] J. Zhang, J. Miao, N. Balasubramani, D.H. Cho, T. Avey, C.Y. Chang, A.A. Luo, Magnesium research and applications: past, present and future, J. Magnes. Alloy. 11 (11) (2023) 3867–3895, https://doi.org/10.1016/j.jma.2023.11.007.
[2] J. Bai, Y. Yang, C. Wen, J. Chen, G. Zhou, B. Jiang, X. Peng, F. Pan, Applications of magnesium alloys for aerospace: a review, J. Magnes. Alloy. 11 (10) (2023) 3609–3619, https://doi.org/10.1016/j.jma.2023.09.015.
[3] J. Yang, Z. Zhu, S. Han, Y. Gu, Z. Zhu, H.D. Zhang, Evolution, limitations, advantages, and future challenges of magnesium alloys as materials for aerospace applications, J. Alloy. Compd. 1008 (2024), https://doi.org/10.1016/j.jallcom.2024.176707.
[4] W.J. Joost, P.E. Krajewski, Towards magnesium alloys for high-volume automotive applications, Scr. Mater. 128 (2017) 107–112, https://doi.org/10.1016/j.scriptamat.2016.07.035.
[5] B. Liu, J. Yang, X. Zhang, Q. Yang, J. Zhang, X. Li, Development and application of magnesium alloy parts for automotive OEMs: a review, J. Magnes. Alloy. 11 (1) (2023) 15–47, https://doi.org/10.1016/j.jma.2022.12.015.
[6] Y. Huang, Y. Zhang, J. Song, F. Pan, R. Willumeit-Römer, K.U. Kainer, N. Hort, Development and prospects of degradable magnesium alloys for structural and functional applications in the fields of environment and energy, J. Magnes. Alloy. 11 (11) (2023) 3926–3947, https://doi.org/10.1016/j.jma.2023.09.013.
[7] F.Z. Akbarzadeh, M. Sarraf, E.R. Ghomi, V.V. Kumar, M. Salehi, S. Ramakrishna, S. Bae, A state-of-the-art review on recent advances in the fabrication and characteristics of magnesium-based alloys in biomedical applications, J. Magnes. Alloy. 12 (7) (2024) 2569–2594, https://doi.org/10.1016/j.jma.2024.06.015.
[8] C.A. Niranjan, T. Raghavendra, M.P. Rao, C. Siddaraju, M. Gupta, V.K.S. Jain, R. Aishwarya, Magnesium alloys as extremely promising alternatives for temporary orthopedic implants – a review, J. Magnes. Alloy. 11 (8) (2023) 2688–2718, https://doi.org/10.1016/j.jma.2023.08.002.
[9] F. Kiani, C. Wen, Y. Li, Prospects and strategies for magnesium alloys as biodegradable implants from crystalline to bulk metallic glasses and composites—a review, Acta Biomater. 103 (2020) 1–23, https://doi.org/10.1016/j.actbio.2019.12.023.
[10] Y. Yang, X. Xiong, J. Chen, X. Peng, D. Chen, F. Pan, Research advances of magnesium and magnesium alloys worldwide in 2022, J. Magnes. Alloy. 11 (8) (2023) 2611–2654, https://doi.org/10.1016/j.jma.2023.07.011.
[11] J. Wang, Y. Zou, C. Dang, Z. Wan, J. Wang, F. Pan, Research progress and the prospect of damping magnesium alloys, Materials 17 (6) (2024) 1285.
[12] G.G. Wang, J.P. Weiler, Recent developments in high-pressure die-cast magnesium alloys for automotive and future applications, J. Magnes. Alloy. 11 (1) (2023) 78–87, https://doi.org/10.1016/j.jma.2022.10.001.
[13] J. Babu, A. Madarapu, D. Kodali, M.V. Ramana, Deep drawing of magnesium alloys: a review, J. Magnes. Alloy. 13 (4) (2025) 1428–1475, https://doi.org/10.1016/j.jma.2025.02.015.
[14] H. Wang, X.C. Luo, D.T. Zhang, C. Qiu, D.L. Chen, High-strength extruded magnesium alloys: a critical review, J. Mater. Sci. Technol. 199 (2024) 27–52, https://doi.org/10.1016/j.jmst.2024.01.089.
[15] U. Masood Chaudry, S. Tekumalla, M. Gupta, T.S. Jun, K. Hamad, Designing highly ductile magnesium alloys: current status and future challenges, Crit. Rev. Solid State Mater. Sci. 47 (2) (2022) 194–281, https://doi.org/10.1080/10408436.2021.1947185.
[16] S. You, Y. Huang, K.U. Kainer, N. Hort, Recent research and developments on wrought magnesium alloys, J. Magnes. Alloy. 5 (3) (2017) 239–253, https://doi.org/10.1016/j.jma.2017.09.001R.
[17] J. Chen, B. Chen, Progress in additive manufacturing of magnesium alloys: a review, Materials 17 (15) (2024), https://doi.org/10.3390/ma17153851.
[18] T. Mukherjee, J.W. Elmer, H.L. Wei, T.J. Lienert, W. Zhang, S. Kou, T. DebRoy, Control of grain structure, phases, and defects in additive manufacturing of high-performance metallic components, Prog. Mater. Sci. 138 (2023), https://doi.org/10.1016/j.pmatsci.2023.101153.
[19] T. DebRoy, H.L. Wei, J.S. Zuback, T. Mukherjee, J.W. Elmer, J.O. Milewski, A. M. Beese, A. Wilson-Heid, A. De, W. Zhang, Additive manufacturing of metallic components – process, structure and properties, Prog. Mater. Sci. 92 (2018) 112–224, https://doi.org/10.1016/j.pmatsci.2017.10.001.
[20] H.L. Wei, T. Mukherjee, W. Zhang, J.S. Zuback, G.L. Knapp, A. De, T. DebRoy, Mechanistic models for additive manufacturing of metallic components, Prog. Mater. Sci. 116 (2021), https://doi.org/10.1016/j.pmatsci.2020.100703.
[21] J.P. Oliveira, T.G. Santos, R.M. Miranda, Revisiting fundamental welding concepts to improve additive manufacturing: From theory to practice, Prog. Mater. Sci. 107 (2020), https://doi.org/10.1016/j.pmatsci.2019.100590.
[22] G. Liu, X. Zhang, X. Chen, Y. He, L. Cheng, M. Huo, J. Yin, F. Hao, S. Chen, P. Wang, S. Yi, L. Wan, Z. Mao, Z. Chen, X. Wang, Z. Cao, J. Lu, Additive manufacturing of structural materials, Materials Science Engineering R Reports 145 (2021), https://doi.org/10.1016/j.mser.2020.100596.
[23] T.H. Becker, P. Kumar, U. Ramamurty, Fracture and fatigue in additively manufactured metals, Acta Mater. 219 (2021), https://doi.org/10.1016/j.actamat.2021.117240.
[24] Q. Li, X.R. Li, B.X. Dong, X.L. Zhang, S.L. Shu, F. Qiu, L.C. Zhang, Z.H. Zhang, Metallurgy and solidification microstructure control of fusion-based additive manufacturing fabricated metallic alloys: a review, Acta Metall. Sin. (Engl. Lett.) 37 (1) (2024) 29–53, https://doi.org/10.1007/s40195-023-01656-y.
[25] D. Herzog, V. Seyda, E. Wycisk, C. Emmelmann, Additive manufacturing of metals, Acta Mater. 117 (2016) 371–392, https://doi.org/10.1016/j.actamat.2016.07.019.
[26] N. Li, S. Huang, G. Zhang, R. Qin, W. Liu, H. Xiong, G. Shi, J. Blackburn, Progress in additive manufacturing on new materials: A review, J. Mater. Sci. Technol. 35 (2) (2019) 242–269, https://doi.org/10.1016/j.jmst.2018.09.002.
[27] Z. Liu, D. Zhao, P. Wang, M. Yan, C. Yang, Z. Chen, J. Lu, Z. Lu, Additive manufacturing of metals: Microstructure evolution and multistage control, in: Journal of Materials Science and Technology, 100, 2022, pp. 224–236, https://doi.org/10.1016/j.jmst.2021.06.011.
[28] W.E. Frazier, Metal additive manufacturing: a review, J. Mater. Eng. Perform. 23 (6) (2014) 1917–1928, https://doi.org/10.1007/s11665-014-0958-z.
[29] S. Cooke, K. Ahmadi, S. Willerth, R. Herring, Metal additive manufacturing: technology, metallurgy and modelling, J. Manuf. Process. 57 (2020) 978–1003, https://doi.org/10.1016/j.jmapro.2020.07.025.
[30] W.J. Sames, F.A. List, S. Pannala, R.R. Dehoff, S.S. Babu, The metallurgy and processing science of metal additive manufacturing, Int. Mater. Rev. 61 (5) (2016) 315–360, https://doi.org/10.1080/09506608.2015.1116649.
[31] S. Chandra, J. Radhakrishnan, S. Huang, S. Wei, U. Ramamurty, Solidification in metal additive manufacturing: challenges, solutions, and opportunities, Prog. Mater. Sci. (2024) 101361, https://doi.org/10.1016/j.pmatsci.2024.101361.
[32] R. Gehrmann, M.M. Frommert, G. Gottstein, Texture effects on plastic deformation of magnesium, Mater. Sci. Eng. A 395 (2005) 338–349.
[33] K. Wei, Z. Wang, X. Zeng, Influence of element vaporization on formability, composition, microstructure, and mechanical performance of the selective laser melted Mg–Zn–Zr components, Mater. Lett. 156 (2015) 187–190.
[34] Y. Wang, J. Huang, The role of twinning and untwinning in yielding behavior in hot-extruded Mg–Al–Zn alloy, Acta Mater. 55 (2007) 897–905.
[35] Q. Yan, B. Song, Y. Shi, Comparative study of performance comparison of AlSi10Mg alloy prepared by selective laser melting and casting, J. Mater. Sci. Technol. 41 (2020) 199–208.

[36] H. Zhu, A. Windle, Effects of cell irregularity on the high strain compression of open-cell foams, Acta Mater. 50 (2002) 1041–1052.
[37] T.L. Nguyen, M.P. Staiger, G.J. Dias, T.B.F. Woodfield, A novel manufacturing route for fabrication of topologically-orderedporous magnesium scaffolds, Adv. Eng. Mater. 13 (2011) 872–881.
[38] Z. Zeng, M. Salehi, A. Kopp, S. Xu, M. Esmaily, N. Birbilis, Recent progress and perspectives in additive manufacturing of magnesium alloys, in: Journal of Magnesium and Alloys, 10, 2022, pp. 1511–1541, https://doi.org/10.1016/j.jma.2022.03.001.
[39] S. Sui, S. Guo, D. Ma, C. Guo, X. Wu, Z. Zhang, C. Xu, D. Shechtman, S. Remennik, D. Safranchik, R. Lapovok, Additive manufacturing of magnesium and its alloys: process-formability-microstructure-performance relationship and underlying mechanism, Int. J. Extrem. Manuf. 5 (4) (2023), https://doi.org/10.1088/2631-7990/acf254.
[40] T.S. Wang, Z.M. Hua, Y. Yang, H.L. Jia, C. Wang, M. Zha, Y. Gao, H.Y. Wang, Macro-/micro-structures and mechanical properties of magnesium alloys based on additive manufacturing: a review, J. Mater. Sci. 59 (22) (2024) 9908–9940, https://doi.org/10.1007/s10853-024-09455-1.
[41] G. Çam, A. Günen, Challenges and opportunities in the production of magnesium parts by directed energy deposition processes, J. Magnes. Alloy. 12 (5) (2024) 1663–1686, https://doi.org/10.1016/j.jma.2024.05.004.
[42] S.K. Manjhi, P. Sekar, S. Bontha, A.S.S. Balan, Additive manufacturing of magnesium alloys: characterization and post-processing, Int. J. Lightweight Mater. Manuf. 7 (1) (2024) 184–213, https://doi.org/10.1016/j.ijlmm.2023.06.004.
[43] R. Karunakaran, S. Ortgies, A. Tamayol, F. Bobaru, M.P. Sealy, Additive manufacturing of magnesium alloys, Bioact. Mater. 5 (1) (2020) 44–54, https://doi.org/10.1016/j.bioactmat.2019.12.004.
[44] Y. Li, S. Yin, G. Zhang, C. Wang, X. Liu, R. Guan, A review on wire arc additive manufacturing of magnesium alloys: wire preparation, defects and properties, Met. Mater. Int. (2024), https://doi.org/10.1007/s12540-024-01724-7.
[45] R. Motallebi, Z. Savaedi, H. Mirzadeh, Post-processing heat treatment of lightweight magnesium alloys fabricated by additive manufacturing: a review, J. Mater. Res. Technol. 20 (2022) 1873–1892, https://doi.org/10.1016/j.jmrt.2022.07.154.
[46] N. Ansari, F.G. Alabtah, M.I. Albakri, M. Khraisheh, Post processing of additive manufactured Mg alloys: current status, challenges, and opportunities, J. Magnes. Alloy. 12 (4) (2024) 1283–1310, https://doi.org/10.1016/j.jma.2024.04.017.
[47] C. Zhang, Z. Li, J. Zhang, H. Tang, H. Wang, Additive manufacturing of magnesium matrix composites: Comprehensive review of recent progress and research perspectives, J. Magnes. Alloy. 11 (2) (2023) 425–461, https://doi.org/10.1016/j.jma.2023.02.005.
[48] X. Wu, J. Liu, Y. Yang, J. Bai, C. Shuai, J. Buhagiar, X. Ning, Laser powder bed fusion of biodegradable magnesium alloys: process, microstructure and properties, Int. J. Extrem. Manuf. 7 (2) (2025), https://doi.org/10.1088/2631-7990/ad967e.
[49] A. Nair, S. Gupta, A. Jangitwar, B. Kandasubramanian, Innovations in 3D printing of magnesium alloys and composites for biodegradable biomedical devices, Bioprinting 46 (2025), https://doi.org/10.1016/j.bprint.2025.e00390.
[50] A. Azadi, T. Ebel, M. Wolff, E. O'Cearbhaill, M. Celikin, Additive manufacturing of magnesium alloys for biomedical applications: critical review on sinterability and alloy development, J. Mater. Res. Technol. 35 (2025) 6986–7007, https://doi.org/10.1016/j.jmrt.2025.03.018.
[51] B. Peng, H. Xu, F. Song, P. Wen, Y. Tian, Y. Zheng, Additive manufacturing of porous magnesium alloys for biodegradable orthopedic implants: process, design, and modification, J. Mater. Sci. Technol. 182 (2024) 79–110, https://doi.org/10.1016/j.jmst.2023.08.072.
[52] R. Allavikutty, P. Gupta, T.S. Santra, J. Rengaswamy, Additive manufacturing of Mg alloys for biomedical applications: current status and challenges, Curr. Opin. Biomed. Eng. 18 (2021), https://doi.org/10.1016/j.cobme.2021.100276.
[53] K. Li, C. Ji, S. Bai, B. Jiang, F. Pan, Selective laser melting of magnesium alloys: necessity, formability, performance, optimization and applications, J. Mater. Sci. Technol. 154 (2023) 65–93, https://doi.org/10.1016/j.jmst.2022.12.053.
[54] C.Y. Tan, C. Wen, H.Q. Ang, Influence of laser parameters on the microstructures and surface properties in laser surface modification of biomedical magnesium alloys, J. Magnes. Alloy. 12 (1) (2024) 72–97, https://doi.org/10.1016/j.jma.2023.12.008.
[55] C.Y. Tan, C. Wen, H.Q. Ang, Influence of laser parameters on the microstructures and surface properties in laser surface modification of biomedical magnesium alloys, J. Magnes. Alloy. 12 (1) (2024) 72–97, https://doi.org/10.1016/j.jma.2023.12.008.
[56] G. Shi, R. Zhang, Y. Cao, G. Yang, A review of the vaporization behavior of some metal elements in the LPBF process, Micromachines 15 (7) (2024), https://doi.org/10.3390/mi15070846.
[57] J. Liu, P. Wen, Metal vaporization and its influence during laser powder bed fusion process, Mater. Des. 215 (2022), https://doi.org/10.1016/j.matdes.2022.110505.
[58] J. Fu, H. Li, X. Song, M.W. Fu, Multi-scale defects in powder-based additively manufactured metals and alloys, J. Mater. Sci. Technol. 122 (2022) 165–199, https://doi.org/10.1016/j.jmst.2022.02.015.
[59] A. Mostafaei, C. Zhao, Y. He, S. Reza Ghiaasiaan, B. Shi, S. Shao, N. Shamsaei, Z. Wu, N. Kouraytem, T. Sun, J. Pauza, J. v Gordon, B. Webler, N.D. Parab, M. Asherloo, Q. Guo, L. Chen, A.D. Rollett, Defects and anomalies in powder bed fusion metal additive manufacturing, Curr. Opin. Solid State Mater. Sci. 26 (2) (2022), https://doi.org/10.1016/j.cossms.2021.100974.
[60] C. Du, Y. Zhao, J. Jiang, Q. Wang, H. Wang, N. Li, J. Sun, Pore defects in Laser Powder Bed Fusion: formation mechanism, control method, and perspectives, J. Alloy. Compd. 944 (2023), https://doi.org/10.1016/j.jallcom.2023.169215.
[61] S. Wang, J. Ning, L. Zhu, Z. Yang, W. Yan, Y. Dun, P. Xue, P. Xu, S. Bose, A. Bandyopadhyay, Role of porosity defects in metal 3D printing: Formation mechanisms, impacts on properties and mitigation strategies, Mater. Today 59 (2022) 133–160, https://doi.org/10.1016/j.mattod.2022.08.014.
[62] J. Berez, C. Saldaña, On the nature and causes of spatter redistribution in laser powder bed fusion, J. Manuf. Process. 127 (2024) 531–544, https://doi.org/10.1016/j.jmapro.2024.07.143.
[63] Z. Zheng, Q. Li, X. Chen, A. Gao, N. Zhang, Application status and prospects of friction stir processing in wrought magnesium alloys: a review, Trans. Indian Inst. Met. 77 (8) (2024) 1891–1906, https://doi.org/10.1007/s12666-024-03290-3.
[64] K. Palanikumar, E. Natarajan, S. Suresh, D.G. Mohan, C. Prakash, K. Kaur, Prospects of friction stir processed Mg alloys and composites-reviews and suggestions, J. Mater. Res. Technol. 31 (2024) 971–997, https://doi.org/10.1016/j.jmrt.2024.06.087.
[65] R.V. Marode, T.A. Lemma, N. Sallih, S.R. Pedapati, M. Awang, A. Hassan, Research progress in friction stir processing of magnesium alloys and their metal matrix surface composites: evolution in the 21st century, J. Magnes. Alloy. 12 (6) (2024) 2091–2146, https://doi.org/10.1016/j.jma.2024.06.007.
[66] W. Wang, P. Han, P. Peng, T. Zhang, Q. Liu, S.N. Yuan, L.Y. Huang, H.L. Yu, K. Qiao, K.S. Wang, Friction stir processing of magnesium alloys: a review, Acta Metall. Sin. (Engl. Lett.) 33 (1) (2020) 43–57, https://doi.org/10.1007/s40195-019-00971-7.
[67] M. Srivastava, S. Rathee, S. Maheshwari, A. Noor Siddiquee, T.K. Kundra, A review on recent progress in solid state friction based metal additive manufacturing: friction stir additive techniques, Crit. Rev. Solid State Mater. Sci. 44 (5) (2019) 345–377, https://doi.org/10.1080/10408436.2018.1490250.
[68] A. Heidarzadeh, S. Mironov, R. Kaibyshev, G. Çam, A. Simar, A. Gerlich, F. Khodabakhshi, A. Mostafaei, D.P. Field, J.D. Robson, A. Deschamps, P. J. Withers, Friction stir welding/processing of metals and alloys: A comprehensive review on microstructural evolution, Prog. Mater. Sci. 117 (2021), https://doi.org/10.1016/j.pmatsci.2020.100752.
[69] R.S. Mishra, R.S. Haridas, P. Agrawal, Friction stir-based additive manufacturing, Sci. Technol. Weld. Join. 27 (3) (2022) 141–165, https://doi.org/10.1080/13621718.2022.2027663.
[70] Q. Cao, B. Qi, C. Zeng, Q. Yang, Z. Jiang, R. Zhang, Y. Xie, F. Wang, B. Cong, Wire-arc directed energy deposition of magnesium alloys: defects, macro-/microstructure, and mechanical performance, Addit. Manuf. Front. 3 (4) (2024), https://doi.org/10.1016/j.amf.2024.200166.
[71] H. Yi, Q. Wang, H. Cao, Wire-arc directed energy deposition of magnesium alloys: microstructure, properties and quality optimization strategies, J. Mater. Res. Technol. 20 (2022) 627–649, https://doi.org/10.1016/j.jmrt.2022.07.083.
[72] C. Tan, R. Li, J. Su, D. Du, Y. Du, B. Attard, Y. Chew, H. Zhang, E.J. Lavernia, Y. Fautrelle, J. Teng, A. Dong, Review on field assisted metal additive manufacturing, Int. J. Mach. Tools Manuf. 189 (2023), https://doi.org/10.1016/j.ijmachtools.2023.104032.
[73] H. Yi, T. Lang, J. Si, Y. Chi, H. Cao, Y. Huang, High-performance manufacturing of metal components via multi-field assisted wire-arc directed energy deposition, J. Manuf. Process. 143 (2025) 234–276, https://doi.org/10.1016/j.jmapro.2025.04.016.
[74] Y. Cao, Y. Zhang, W. Ming, W. He, J. Ma, Review: the metal additive-manufacturing technology of the ultrasonic-assisted wire-and-arc additive-manufacturing process, Metals 13 (2) (2023), https://doi.org/10.3390/met13020398.
[75] C. Zeng, J. Xue, Y. Jia, S. Luo, F. Huang, X. Liu, Y. Du, A review of additive manufacturing of metallic materials assisted by electromagnetic field technology, J. Manuf. Process. 131 (2024) 920–946, https://doi.org/10.1016/j.jmapro.2024.09.078.
[76] D. Jafari, T.H.J. Vaneker, I. Gibson, Wire and arc additive manufacturing: opportunities and challenges to control the quality and accuracy of manufactured parts, Mater. Des. 202 (2021), https://doi.org/10.1016/j.matdes.2021.109471.
[77] M.R. Zahidin, F. Yusof, S.H. Abdul Rashid, S. Mansor, S. Raja, M.F. Jamaludin, Y. H. Manurung, M.S. Adenan, N.I. Syahriah Hussein, Research challenges, quality control and monitoring strategy for Wire Arc Additive Manufacturing, J. Mater. Res. Technol. 24 (2023) 2769–2794, https://doi.org/10.1016/j.jmrt.2023.03.200.
[78] B. Wu, Z. Pan, D. Ding, D. Cuiuri, H. Li, J. Xu, J. Norrish, A review of the wire arc additive manufacturing of metals: properties, defects and quality improvement, J. Manuf. Process. 35 (2018) 127–139, https://doi.org/10.1016/j.jmapro.2018.08.001.
[79] C.R. Cunningham, J.M. Flynn, A. Shokrani, V. Dhokia, S.T. Newman, Invited review article: Strategies and processes for high quality wire arc additive manufacturing, Addit. Manuf. 22 (2018) 672–686, https://doi.org/10.1016/j.addma.2018.06.020.
[80] S.W. Williams, F. Martina, A.C. Addison, J. Ding, G. Pardal, P. Colegrove, Wire + Arc additive manufacturing, Materials Science Technology (United Kingdom) 32 (7) (2016) 641–647, https://doi.org/10.1179/1743284715Y.0000000073.
[81] B. Tomar, S. Shiva, Cold metal transfer-based wire arc additive manufacturing, J. Braz. Soc. Mech. Sci. Eng. 45 (3) (2023), https://doi.org/10.1007/s40430-023-04084-2.
[82] T. Mukherjee, T. DebRoy, A digital twin for rapid qualification of 3D printed metallic components, Appl. Mater. Today 14 (2019) 59–65, https://doi.org/10.1016/j.apmt.2018.11.003.

[83] S. Hu, H. Zhang, Z. Wang, Y. Liang, Y. Liu, The arc characteristics of cold metal transfer welding with AZ31 magnesium alloy wire, J. Manuf. Process. 24 (2016) 298–306, https://doi.org/10.1016/j.jmapro.2016.10.001.
[84] B. Mvola, P. Kah, P. Layus, Review of current waveform control effects on weld geometry in gas metal arc welding process, Int. J. Adv. Manuf. Technol. 96 (9–12) (2018) 4243–4265, https://doi.org/10.1007/s00170-018-1879-z.
[85] B. Cong, J. Ding, S. Williams, Effect of arc mode in cold metal transfer process on porosity of additively manufactured Al-6.3%Cu alloy, Int. J. Adv. Manuf. Technol. 76 (9–12) (2015) 1593–1606, https://doi.org/10.1007/s00170-014-6346-x.
[86] S. Kesarwani, N. Yuvaraj, M.S. Niranjan, CMT-based WAAM: a comprehensive review of process parameters, their effects, challenges, and future scope, J. Braz. Soc. Mech. Sci. Eng. 46 (12) (2024), https://doi.org/10.1007/s40430-024-05276-0.
[87] T. Nitschke-Pagel, H. Wohlfahrt, Residual stresses in welded joints–sources and consequences, Mater. Sci. Forum 404 (2002, August) 215–226.
[88] H. Yi, L. Jia, J. Ding, H. Li, Achieving material diversity in wire arc additive manufacturing: Leaping from alloys to composites via wire innovation, Int. J. Mach. Tools Manuf. 194 (2024), https://doi.org/10.1016/j.ijmachtools.2023.104103.
[89] K. Yang, W. Yang, H. Yang, H. Chen, Y. Ai, F. He, X. Lin, Mechanistic insights into ultrasonic cavitation in magnesium alloy melt pools: effects on pore formation and microstructural evolution, J. Mater. Process. Technol. (2026) 119299.
[90] Z. Tong, K. Liu, L. Chen, J. Tan, K. Peng, X. Chen, Achieving synergistic strength-ductility in CMT-WAAM fabricated AZ31 through in-situ oxidation and ultrasonic-assisted, J. Manuf. Process. 157 (2026) 784–797.
[91] T. Yuan, Z. Luo, S. Kou, Grain refining of magnesium welds by arc oscillation, Acta Mater. 116 (2016) 166–176, https://doi.org/10.1016/j.actamat.2016.06.036.
[92] Y.B. Liu, J.Z. Li, Q.J. Sun, P. Jin, Q. Sun, B.P. Li, J.C. Feng, Optimization of magnetic oscillation system and microstructural characteristics in arc welding of Al/Mg alloys, J. Manuf. Process. 39 (2019) 69–78.
[93] H. Yi, F. Jiao, H. Cao, J. Zhang, Y. Zou, Numerical simulations of molten pool dynamics in wire-arc directed energy deposition processes: a review, J. Manuf. Process. 134 (2025) 970–997, https://doi.org/10.1016/j.jmapro.2025.01.022.
[94] S. Cadiou, M. Courtois, M. Carin, W. Berckmans, P. Le masson, 3D heat transfer, fluid flow and electromagnetic model for cold metal transfer wire arc additive manufacturing (Cmt-Waam), Addit. Manuf. 36 (2020), https://doi.org/10.1016/j.addma.2020.101541.
[95] T. Zhang, C. Xu, J. Cheng, Y. Huang, Y. Peng, L. Wang, K. Wang, Study on droplet transfer behavior and spattering mechanism in Mg-Gd-Y-Zr alloy regulated short circuit (Fronius CMT) welding, J. Manuf. Process. 126 (2024) 35–47, https://doi.org/10.1016/j.jmapro.2024.07.075.
[96] W. Ou, T. Mukherjee, G.L. Knapp, Y. Wei, T. DebRoy, Fusion zone geometries, cooling rates and solidification parameters during wire arc additive manufacturing, Int. J. Heat. Mass Transf. 127 (2018) 1084–1094, https://doi.org/10.1016/j.ijheatmasstransfer.2018.08.111.
[97] Y. Wang, S. Shuai, C. Huang, T. Jing, C. Chen, T. Hu, J. Wang, Z. Ren, Revealing the diversity of dendritic morphology evolution during solidification of magnesium alloys using synchrotron X-ray imaging: a review, Acta Metall. Sin. Engl. Lett. 35 (2) (2022) 177–200, https://doi.org/10.1007/s40195-021-01319-w.
[98] K. Bhagat, S. Rudraraju, Modeling of dendritic solidification and numerical analysis of the phase-field approach to model complex morphologies in alloys, Eng. Comput. 39 (4) (2023) 2345–2363, https://doi.org/10.1007/s00366-022-01767-7.
[99] F. Wang, W. Chen, D. Wang, H. Hou, Y. Zhao, Phase-field modeling and experimental investigation for rapid solidification in wire and arc additive manufacturing, J. Mater. Res. Technol. 28 (2024) 4585–4599, https://doi.org/10.1016/j.jmrt.2024.01.021.
[100] J. Wang, Z. Zhao, W. Du, P. Bai, L. Wang, Z. Zhang, Z. Huang, Macro-micro numerical simulation and experimental study of Mg-Gd-Y-Zn-Zr alloy fabricated by cold metal transfer wire arc additive manufacturing, J. Mater. Res. Technol. 23 (2023) 403–418, https://doi.org/10.1016/j.jmrt.2022.12.193.
[101] Y. Wang, Y. Zhang, X. Liu, J. Wang, X. Xie, J. Jiang, J. Liu, H. Liu, Y. Wu, S. Dong, L. Peng, Simulation of microstructure evolution in Mg alloys by phase-field methods: a review, Crystals 12 (9) (2022), https://doi.org/10.3390/cryst12091305.
[102] M.J. Aziz, Model for solute redistribution during rapid solidification, J. Appl. Phys. 53 (2) (1982) 1158–1168, https://doi.org/10.1063/1.329867.
[103] K. Wu, X. Wang, L. Xiao, Z. Li, Z. Han, Experimental study on the effect of cooling rate on the secondary phase in As-Cast Mg–Gd–Y–Zr alloy, Adv. Eng. Mater. 20 (3) (2018), https://doi.org/10.1002/adem.201700717.
[104] H. Cai, N. Zhang, L. Liu, J. Su, Y. Li, Y. Kang, F. Guo, Effects of cooling rate on the microstructure and properties of magnesium alloy-a review, J. Magnes. Alloy. (2024), https://doi.org/10.1016/j.jma.2024.06.021.
[105] M. Pouranvari, Critical review on fusion welding of magnesium alloys: metallurgical challenges and opportunities, Sci. Technol. Weld. Join. 26 (8) (2021) 559–580, https://doi.org/10.1080/13621718.2021.1982339.
[106] Y.H. Yang, Z.P. Guan, P.K. Ma, M.W. Ren, H.L. Jia, P. Zhao, M. Zha, H.Y. Wang, Wire arc additive manufacturing of a novel ATZM31 Mg alloy: Microstructure evolution and mechanical properties, J. Magnes. Alloy. 12 (12) (2024) 5024–5037, https://doi.org/10.1016/j.jma.2023.08.014.
[107] J. Wang, Z. Zhao, P. Bai, R. Zhang, Z. Zhang, L. Wang, W. Du, F. Wang, Z. Huang, Microstructure and mechanical properties of AZ31 magnesium alloy prepared using wire arc additive manufacturing, J. Alloy. Compd. 939 (2023), https://doi.org/10.1016/j.jallcom.2022.168665.
[108] X. Yang, J. Liu, Z. Wang, X. Lin, F. Liu, W. Huang, E. Liang, Microstructure and mechanical properties of wire and arc additive manufactured AZ31 magnesium alloy using cold metal transfer process, Materials Science Engineering A 774 (2020), https://doi.org/10.1016/j.msea.2020.138942.
[109] W. Yang, H. Yang, K. Yang, X. Wang, C. Hu, X. Lin, Microstructure evolution and mechanical properties of large-size AZ31 magnesium alloy block fabricated by wire arc additive manufacturing, J. Magnes. Alloy. 13 (2025) 1187–1202, https://doi.org/10.1016/j.jma.2024.04.024.
[110] B. Ren, C. Chen, B. Yang, Y. Gao, X. Sui, Y. Fu, Z. Li, X. Zhao, Exploring the impact of multiple parameter combinations with constant heat input on weld integrity of Mg alloy welded joints prepared by cold metal transfer technology, J. Magnes. Alloy. (2025), https://doi.org/10.1016/j.jma.2025.03.011.
[111] Z. Zhang, J. Shen, J. Bi, S. Hu, Y. Zhen, X. Bu, Microstructure and mechanical properties of weaving wire and arc additive manufactured AZ91 magnesium alloy based on cold metal transfer technique, Materials 16 (11) (2023), https://doi.org/10.3390/ma16114047.
[112] S. Cheng, F. Liu, Y. Xu, C. Li, F. Liu, C. Huang, X. Lin, H. Zheng, Effects of arc oscillation on microstructure and mechanical properties of AZ31 magnesium alloy prepared by CMT wire-arc directed energy deposition, Materials Science Engineering A 864 (2023), https://doi.org/10.1016/j.msea.2022.144539.
[113] J.D. Kim, H.U. Jun, J. Cheon, J. Kim, J.H. Kim, C. Ji, Y. do Kim, Effect of additional side shielding on the wire arc additive manufacturing of AZ31 magnesium alloy, J. Mater. Res. Technol. 25 (2023) 6567–6577, https://doi.org/10.1016/j.jmrt.2023.07.147.
[114] J.D. Kim, J. Cheon, Y. Park, Y. do do, Kim, C. Ji, On the fabrication of finer grain structure through using finer wire diameter for wire arc additive manufacturing of AZ31B magnesium alloy, J. Mater. Res. Technol. (30 (2024) 3916–3928, https://doi.org/10.1016/j.jmrt.2024.04.113.
[115] S.K. Manjhi, P. Sekar, S. Bontha, A.S.S. Balan, Effect of equiaxed grains and secondary phase particles on mechanical properties and corrosion behaviour of CMT- based wire arc additive manufactured AZ31 Mg alloy, CIRP J. Manuf. Sci. Technol. 46 (2023) 48–64, https://doi.org/10.1016/j.cirpj.2023.07.008.
[116] S.K. Manjhi, P. Sekar, S. Bontha, A.S.S. Balan, Effect of CMT-WAAM process parameters on bead geometry, microstructure and mechanical properties of AZ31 Mg alloy, J. Mater. Eng. Perform. 33 (16) (2024) 8567–8581, https://doi.org/10.1007/s11665-023-08498-w.
[117] J. Bi, J. Shen, S. Hu, Y. Zhen, F. Yin, X. Bu, Microstructure and mechanical properties of AZ91 Mg alloy fabricated by cold metal transfer additive manufacturing, Mater. Lett. 276 (2020), https://doi.org/10.1016/j.matlet.2020.128185.
[118] T. Klein, A. Arnoldt, M. Schnall, S. Gneiger, Microstructure formation and mechanical properties of a wire-arc additive manufactured magnesium alloy, JOM 73 (4) (2021) 1126–1134, https://doi.org/10.1007/s11837-021-04567-4.
[119] Z. Zhang, J. Shen, S. Hu, Y. Chen, C. Yin, X. Bu, Optimization of CMT characteristic parameters for swing arc additive manufacturing of AZ91 magnesium alloy based on process stability analysis, Materials 16 (8) (2023), https://doi.org/10.3390/ma16083236.
[120] D. Ma, C. Xu, Jie, J. Tian, S. Sui, C. Guo, X. Wu, Quan, Z. ming Zhang, Study on anisotropy of microstructure and mechanical properties of AZ31 magnesium alloy fabricated by wire arc additive manufacturing, China Foundry 20 (4) (2023) 280–288, https://doi.org/10.1007/s41230-023-2187-2.
[121] P. Wang, H. Zhang, H. Zhu, Q. Li, M. Feng, Wire-arc additive manufacturing of AZ31 magnesium alloy fabricated by cold metal transfer heat source: processing, microstructure, and mechanical behavior, J. Mater. Process. Technol. 288 (2021), https://doi.org/10.1016/j.jmatprotec.2020.116895.
[122] M. Zhao, Z. Zhao, W. Du, P. Bai, Z. Huang, Simulation study on temperature and stress fields in Mg-Gd-Y-Zn-Zr alloy during CMT additive manufacturing process, Materials 17 (5) (2024), https://doi.org/10.3390/ma17051199.
[123] M. Zhao, Z. Zhao, W. Du, P. Bai, Z. Huang, Temperature field simulation and microstructure study of WAAM fabricated Mg-Gd-Y-Zn-Zr alloy, Mater. Today Commun. 38 (2024), https://doi.org/10.1016/j.mtcomm.2024.108512.
[124] P. Bai, J. Wang, Z. Zhao, W. Du, D. Tie, C. Cai, R. Zhang, F. Wang, Microstructure and mechanical properties of Mg-Gd-Y-Zn-Zr alloy fabricated by cold metal transfer wire arc additive manufacturing, J. Mater. Res. Technol. 27 (2023) 5805–5821, https://doi.org/10.1016/j.jmrt.2023.10.265.
[125] W. Yang, H. Yang, K. Yang, Z. Wang, X. Wang, C. Hu, X. Lin, Wire-arc additive manufacturing of Mg-Gd-Y-Zn-Zr alloy fabricated by cold metal transfer heat source: Processing, microstructure, and mechanical properties, J. Mater. Res. Technol. 29 (2024) 5551–5561, https://doi.org/10.1016/j.jmrt.2024.03.026.
[126] D. Ma, C. Xu, Y. Qi, S. Sui, J. Tian, T. Tu, C. Guo, X. Wu, Z. Zhang, S. Remennik, D. Shechtman, Microstructural evolution and mechanical properties of Mg-8.1Gd-2.6Y-0.7Zn-0.5Zr alloy by multi-layer wire arc additive manufacturing, J. Mater. Res. Technol. 27 (2023) 6974–6983, https://doi.org/10.1016/j.jmrt.2023.11.142.
[127] C. Zhang, R. Ju, Y. Li, Z. Zhao, L. Wang, K. Ma, D. Zhang, Z. Zhang, P. Bai, Wire-arc additive manufacturing of Mg-Gd-Y-Zn-Zr alloy: Microstructure and mechanical properties, J. Mater. Res. Technol. 32 (2024) 3083–3092, https://doi.org/10.1016/j.jmrt.2024.08.150.
[128] G. Li, Y. Li, Z. Zhao, S. Wei, L. Wang, K. Ma, D. Zhang, Z. Zhang, X. Lin, P. Bai, Investigation of microstructure and mechanical properties of GWZ1031K alloy additively manufactured by cold metal transfer-based wire-arc directed energy deposition, J. Alloy. Compd. 1021 (2025), https://doi.org/10.1016/j.jallcom.2025.179652.

[129] R. Ju, Y. Li, Z. Zhao, L. Wang, K. Ma, D. Zhang, S. Wei, Z. Zhang, W. Fan, X. Lin, P. Bai, Effect of wire feed rate on microstructure and mechanical properties of Mg-Gd-Y-Zn-Zr alloy fabricated via cold metal transfer wire-arc additive manufacturing(CMT-WAAM), J. Alloy. Compd. 1029 (2025), https://doi.org/10.1016/j.jallcom.2025.180812.
[130] Z. Deng, Q. Su, M. Chen, F. Wang, L. Ke, F. Wang, J. Dong, Isotropic high strength Mg-Gd-Y-Zn-Zr alloy fabricated by wire arc additive manufacturing based on cold metal transfer, J. Magnes. Alloy. (2024), https://doi.org/10.1016/j.jma.2024.05.014.
[131] D. Ma, C. Xu, Y. Qi, S. Sui, J. Tian, T. Tu, C. Guo, X. Wu, Z. Zhang, S. Remennik, D. Shechtman, Achieving fully equiaxed grain microstructure and isotropic mechanical properties in wire arc additive-manufactured Mg-Y-Nd-Zr alloys, J. Alloy. Compd. 962 (2023), https://doi.org/10.1016/j.jallcom.2023.171041.
[132] F. Chen, X. Cai, B. Dong, S. Lin, Microstructure and mechanical properties of WE43 magnesium alloy fabricated by wire-arc additive manufacturing, ThinWalled Struct. 206 (2025) 112699, https://doi.org/10.1016/j.tws.2024.112699.
[133] F. Chen, X. Cai, B. Dong, S. Lin, Effect of process modes on microstructure and mechanical properties of CMT wire arc additive manufactured WE43 magnesium alloy, J. Mater. Res. Technol. 27 (2023) 2089–2101, https://doi.org/10.1016/j.jmrt.2023.10.063.
[134] H. Shi, R. Liu, H. Chen, W. Wang, J. Zhou, X. Chen, K. Liu, Microstructural evolution and mechanical properties of ZM6(Mg-Nd-Zr-Zn) alloy fabricated by wire arc additive manufacturing, J. Alloy. Compd. 1022 (2025), https://doi.org/10.1016/j.jallcom.2025.180096.
[135] X. Tao, J. Sun, Y. Huang, J. Yu, Y. Guo, Y. Xu, L. Yi, G. Wu, W. Liu, Ultra-light Mg-Li alloy with high modulus prepared by cold metal transfer-based directed energy deposition, Addit. Manuf. 97 (2025), https://doi.org/10.1016/j.addma.2024.104617.
[136] D. Liu, X. Zong, P. Xue, Y. Zhang, H. Zhou, Z. Gao, R. Wang, B. Lu, Comprehensive study on the differences in microstructure and mechanical properties of Mg–Li alloy fabricated by additive manufacturing, casting, and rolling, J. Mater. Res. Technol. 31 (2024) 4128–4138, https://doi.org/10.1016/j.jmrt.2024.07.147.
[137] Z. Xu, J. Xiao, S. Chen, C. Ding, S. Gai, Z. Yan, In-situ high-dynamic micro hammering enhanced wire-arc direct energy deposition of magnesium alloy, J. Magnes. Alloy. (2025), https://doi.org/10.1016/j.jma.2025.03.022.
[138] X. Fang, J. Yang, X. Jiang, X. Li, R. Chen, K. Huang, Wire-arc directed energy deposited high-performance AZ31 magnesium alloy via a novel interlayer hammering treatment, Materials Science Engineering A (2024) *889*, https://doi.org/10.1016/j.msea.2023.145864.
[139] J. Wei, C. He, M. Qie, Y. Liu, H. Zhou, C. Kang, G. Qin, Achieving high strength-ductility of AZ91 magnesium alloy via wire-arc directed energy deposition assisted by interlayer friction stir processing, Addit. Manuf. 94 (2024), https://doi.org/10.1016/j.addma.2024.104453.
[140] H. Yi, Q. Wang, W. Zhang, H. Cao, Wire-arc directed energy deposited Mg-Al alloy assisted by ultrasonic vibration: Improving properties via controlling grain structures, J. Mater. Process. Technol. 321 (2023), https://doi.org/10.1016/j.jmatprotec.2023.118134.
[141] X. Liu, S. Yin, G. Zhang, Y. Li, R. Guan, Effect of interlayer ultrasonic impact on the microstructure, mechanical and corrosion properties of wire arc additive manufacturing AZ31 Mg alloy thin wall, J. Mater. Res. Technol. 33 (2024) 180–192, https://doi.org/10.1016/j.jmrt.2024.09.040.
[142] X. Zhao, B. Ren, Y. Zhang, H. Wang, Y. Liu, X. Zhang, C. Chen, Microstructural evolution and strengthening mechanisms of CMT directed energy deposition-arc with interlayer ultrasonic impact treatment manufactured AZ31 magnesium alloy, Materials Science Engineering A 879 (2023), https://doi.org/10.1016/j.msea.2023.145267.
[143] S. Chen, H. Yi, Q. Wang, H. Cao, Effect of ultrasonic vibration on corrosion properties of wire-arc directed energy deposited magnesium alloy, J. Alloy. Compd. 1019 (2025), https://doi.org/10.1016/j.jallcom.2025.179313.
[144] X. Li, X. Fang, M. Zhang, B. Wang, K. Huang, Enhanced strength-ductility synergy of magnesium alloy fabricated by ultrasound assisted directed energy deposition, J. Mater. Sci. Technol. 178 (2024) 247–261, https://doi.org/10.1016/j.jmst.2023.09.021.
[145] X. Li, X. Fang, M. Zhang, B. Wang, K. Huang, Enhanced strength-ductility synergy of magnesium alloy fabricated by ultrasound assisted directed energy deposition, J. Mater. Sci. Technol. 178 (2024), https://doi.org/10.1016/j.jmst.2023.09.021.
[146] K. Yang, W. Yang, F. He, H. Yang, H. Chen, X. Lin, CMT-WAAM processing of AZ31 magnesium alloy assisted with ultrasound: Evolution of arc, melt pool and microstructure, J. Manuf. Process. 148 (2025) 442–458.
[147] X. Li, X. Fang, M. Zhang, H. Zhang, Y. Duan, K. Huang, Gradient microstructure and prominent performance of wire-arc directed energy deposited magnesium alloy via laser shock peening, Int. J. Mach. Tools Manuf. 188 (2023), https://doi.org/10.1016/j.ijmachtools.2023.104029.
[148] S.K. Manjhi, O. R, S. Bontha, A.S.S. Balan, Effect of burnishing strategies on surface integrity, microstructure and corrosion performance of wire arc additively manufactured AZ31 Mg alloy, Int. J. Lightweight Mater. Manuf. 8 (3) (2025) 355–373, https://doi.org/10.1016/j.ijlmm.2024.12.001.
[149] Y.H. Yang, H.L. Jia, C. Wang, W. Liu, M. Zha, P.K. Ma, Z.P. Guan, H.Y. Wang, An innovative strategy to prepare fine-grained Mg-Al alloys with a superior strength-ductility synergy via wire-arc directed energy deposition, Addit. Manuf. 86 (2024), https://doi.org/10.1016/j.addma.2024.104207.
[150] C. Zhang, Z. Li, Y. Tu, J. Wang, J. Zhang, H. Tang, In-situ strengthening of AZ31 magnesium alloy by introducing TC4 particles during wire-arc directed energy deposition with simultaneous feeding of powder and wire, Virtual Phys. Prototyp. 19 (1) (2024), https://doi.org/10.1080/17452759.2024.2387294.
[151] C. Zhang, Z. Li, Y. Tu, J. Wang, F. Weng, J. Zhang, H. Tang, Regulation on microstructure and mechanical properties of SiC particles reinforced AZ31 magnesium matrix composites fabricated by synchronous feeding of powder and wire in wire-arc directed energy deposition, J. Mater. Res. Technol. 30 (2024) 7789–7802, https://doi.org/10.1016/j.jmrt.2024.05.070.
[152] H. Dieringa, M. Nienaber, D. Giannopoulou, J. Isakovic, J. Bohlen, M.S. Kujur, N. ben Khalifa, T. Klein, S. Gneiger, Novel magnesium nanocomposite for wire-arc directed energy deposition, Materials 17 (2) (2024), https://doi.org/10.3390/ma17020500.
[153] Q. Cao, B. Qi, C. Zeng, R. Zhang, B. He, Z. Qi, F. Wang, H. Wang, B. Cong, Achieving equiaxed microstructure and isotropic mechanical properties of additively manufactured AZ31 magnesium alloy via ultrasonic frequency pulsed arc, J. Alloy. Compd. 909 (2022), https://doi.org/10.1016/j.jallcom.2022.164742.
[154] X. Li, M. Zhang, X. Fang, Z. Li, G. Jiao, K. Huang, Improved strength-ductility synergy of directed energy deposited AZ31 magnesium alloy with cryogenic cooling mode, Virtual Phys. Prototyp. 18 (1) (2023), https://doi.org/10.1080/17452759.2023.2170252.
[155] P. Ma, C. Wang, H. Jia, Y. Yang, M. Zha, Simultaneous enhancement in deposition efficiency and nano-scale precipitation of high-strength AZ31 Mg alloy via water cooling assisted wire-arc directed energy deposition, Thin Walled Struct. 206 (2025), https://doi.org/10.1016/j.tws.2024.112689.
[156] H. Zhang, D. Xin, X. Zhang, K. Wang, E. Tang, X. Pan, C. Wu, Comparative study on microstructure and mechanical properties of CMT wire-arc directed energy deposited magnesium alloy assisted by water bath cooling and ultrasonic vibration, Mater. Lett. 380 (2025), https://doi.org/10.1016/j.matlet.2024.137741.
[157] J. Li, Y. Qiu, J. Yang, Y. Sheng, Y. Yi, X. Zeng, L. Chen, F. Yin, J. Su, T. Zhang, X. Tong, B. Guo, Effect of grain refinement induced by wire and arc additive manufacture (WAAM) on the corrosion behaviours of AZ31 magnesium alloy in NaCl solution, J. Magnes. Alloy. 11 (1) (2023) 217–229, https://doi.org/10.1016/j.jma.2021.04.007.
[158] K. Li, B. Li, L. Zhu, X. Hou, Z. Li, L.E. Murr, B. Jiang, F. Pan, Optimizing microstructure and strength of CMT-wire arc additive manufactured WE43 Mg alloy through a novel active cooling technique, Thin Walled Struct. 205 (2024), https://doi.org/10.1016/j.tws.2024.112453.
[159] G. Graf, P. Spoerk-Erdely, E. Maawad, M. Burtscher, D. Kiener, H. Clemens, T. Klein, Effect of wire-arc directed energy deposition on the microstructural formation and age-hardening response of the Mg-9Al-1Zn (AZ91) alloy, J. Magnes. Alloy. 11 (6) (2023) 1944–1958, https://doi.org/10.1016/j.jma.2023.05.012.
[160] D. Ma, C. Xu, S. Sui, Y. Qi, C. Guo, Z. Zhang, J. Tian, F. Zeng, S. Remennik, D. Shechtman, Customized heat treatment process enabled excellent mechanical properties in wire arc additively manufactured Mg-RE-Zn-Zr alloys, Int. J. Extrem. Manuf. 6 (4) (2024), https://doi.org/10.1088/2631-7990/ad48ea.
[161] X. Li, M. Zhang, X. Fang, X. Liu, Y. Zhou, T. Chang, K. Huang, The origin of ultrahigh-strength in GWZ1021K alloy fabricated by wire-arc directed energy deposition, J. Magnes. Alloy. (2024), https://doi.org/10.1016/j.jma.2024.11.011.
[162] X. Li, X. Fang, Z. Zhang, S. Ghafoor, R. Chen, Y. Liu, K. Tang, K. Li, M. Ma, J. Shang, K. Huang, Revealing precipitation behavior and mechanical response of wire-arc directed energy deposited Mg-Gd-Y-Zr alloy by tailoring aging procedures, Int. J. Extrem. Manuf. 6 (4) (2024), https://doi.org/10.1088/2631-7990/ad35fd.
[163] D. Ma, C. Xu, S. Sui, J. Tian, C. Guo, X. Wu, Z. Zhang, S. Remennik, D. Shechtman, Microstructure evolution and mechanical properties of wire arc additively manufactured Mg-Gd-Y-Zr alloy by post heat treatments, Virtual Phys. Prototyp. 18 (1) (2023), https://doi.org/10.1080/17452759.2023.2225492.
[164] C. Shen, Y. Tu, X. Cheng, Z. Li, Y. Jiang, F. Cheng, D. Zheng, Z. Xu, Effect of heat treatment on microstructure and mechanical properties of Mg-6Gd-3Y-0.5Zr alloy fabricated by wire arc additive manufacturing, J. Alloy. Compd. 986 (2024), https://doi.org/10.1016/j.jallcom.2024.174063.
[165] Z. Liu, L. Wang, S. Luo, Y. Feng, S. Zhao, Y. Fu, Effect of heat treatment on microstructure and mechanical properties of WE43 alloy fabricated by wire arc additive manufacturing, Mater. Today Commun. 41 (2024) 110950, https://doi.org/10.1016/j.mtcomm.2024.110950.
[166] D. Ma, C. Xu, S. Sui, J. Tian, F. Zeng, S. Remennik, D. Shechtman, Z. Zhang, C. Guo, Y. Qi, Enhanced age-hardening and formation of plate precipitates in Mg-Gd-Ag-Al alloy fabricated by wire-arc additive manufacturing, Materials Science Technology (United Kingdom) (2025), https://doi.org/10.1177/02670836251318551.
[167] D. Ma, C. Xu, S. Sui, J. Tian, C. Guo, X. Wu, Z. Zhang, D. Shechtman, S. Remennik, Enhanced strength-ductility synergy in a wire and arc additively manufactured Mg alloy via tuning interlayer dwell time, J. Magnes. Alloy. 11 (12) (2023) 4696–4709, https://doi.org/10.1016/j.jma.2023.01.015.
[168] X.R. Zhang, A. Li, X.Z. Li, D.D. Zhang, G.L. Bi, D.Q. Fang, X.D. Ding, J. Sun, Fully equiaxed grain structure and isotropic mechanical properties in wire arc additive manufactured Mg–Al-RE alloy, J. Mater. Res. Technol. 31 (2024) 3998–4011, https://doi.org/10.1016/j.jmrt.2024.07.073.
[169] J. Li, Y. Hao, K. Zhao, H. Liang, B. Zhang, Z. Deng, F. Wang, Hot compression behavior and 3D processing maps of Mg-Gd-Y-Zn alloy formed by cold metal

transfer wire arc additive manufacturing, Materials Science Technology (United Kingdom) (2024), https://doi.org/10.1177/02670836241305971.
[170] J. Wang, Z. Zhao, W. Du, P. Bai, L. Wang, Z. Zhang, Z. Huang, High-temperature compression deformation strengthening mechanism of Mg–Gd–Y–Zn–Zr alloy formed by cold metal transfer (CMT) arc additive forming, Materials Science Engineering A 893 (2024), https://doi.org/10.1016/j.msea.2024.146084.
[171] Z. Zhao, J. Wang, W. Du, P. Bai, L. Wang, Z. Zhang, Z. Huang, The high-temperature deformation and microstructural evolution mechanism of Mg-Gd-Y-Zn-Zr alloy formed by CMT arc additive forming, Virtual Phys. Prototyp. 18 (1) (2023), https://doi.org/10.1080/17452759.2023.2279152.